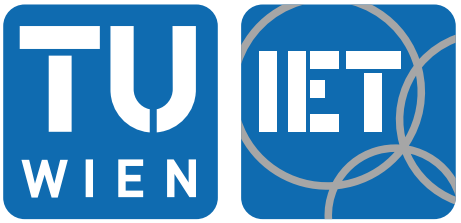

INSTITUT FÜR
ENERGIETECHNIK
UND THERMODYNAMIK
Institute of Energy Systems and Thermodynamics

Master's Thesis

Influence of Spatial and Temporal Parameters in a Part Load operating Francis Runner CFD Simulation

under the supervision of

Ass.Prof. Dipl.-Ing. Dr.techn. Eduard Doujak
E302 - Institute of Energy Systems and Thermodynamics

assisted by

Projektass. Dipl.-Ing. Franz Josef Haller BSc
E302 - Institute of Energy Systems and Thermodynamics

submitted to the Faculty of Mechanical and Industrial Engineering
of Technische Universität Wien
for the degree of Diplom-Ingenieur (Dipl.-Ing.)

by

Manuel Oos, BSc
[redacted]

Die approbierte gedruckte Originalversion dieser Diplomarbeit ist an der TU Wien Bibliothek verfügbar
The approved original version of this thesis is available in print at TU Wien Bibliothek.

Statutory Declaration

This thesis is the result of my own work and includes nothing that is the outcome of work done in collaboration except as specified in the text.

It is not substantially the same as any that I have submitted, or, is being concurrently submitted for a degree or diploma or other qualification at Technische Universität Wien or any other University or similar institution except as specified in the text. I further state that no substantial part of my thesis has already been submitted, or, is being concurrently submitted for any such degree, diploma or other qualification at Technische Universität Wien or any other University or similar institution except as specified in the text.

Vienna, August 2023 .....

(Manuel Oos, BSc)

Die approbierte gedruckte Originalversion dieser Diplomarbeit ist an der TU Wien Bibliothek verfügbar
The approved original version of this thesis is available in print at TU Wien Bibliothek.

Acknowledgements

I would like to take this opportunity and express my deepest gratitude to my wife, Lena. Your unconditional love and support, in every instance since our togetherness, is invalueable. It is you, and not the battle you have to endure, that takes my mind back to the important things in life, certainly when I get lost in the endeavour of my education and work. I wish for nothing but a long future ahead of us.

My sincere appreciation, not only for his understanding of our situation, but also his guidance and the trust in my contribution, goes to my supervisor Ass.Prof. Dipl.-Ing. Dr.techn. Eduard Doujak. His character, experience and the exemplified leadership, is something I truly admire.

Gratitude is also owed to my colleagues Alex, Christian, Constantin, Daniel and Franz, for their support and collaboration during my research.

Eternal thanks go to my parents Karin and Markus, not only for enabling my pursuite of a higher education, but also for the sacrifices they made, to make the current life, my sister Sarah and I are living, possible. The same gratitude is also expressed towards my parents in law Christiane and Christoph. Since our first acquaintance, they have supported and treated me, as if I was one of their own children.

Finally, I feel the need to thank the rest of my family, my family in law and my friends. You are all the reason, that make the journey of life, worthwhile.

Die approbierte gedruckte Originalversion dieser Diplomarbeit ist an der TU Wien Bibliothek verfügbar
The approved original version of this thesis is available in print at TU Wien Bibliothek.

Abstract

The thesis investigates the influence of spatial and temporal parameters on a conducted simulation of a Francis runner, that operates in off design condition. The timestep size in seconds, which correlates to one degree of a single runner revolution (dt), is refined in two stages. The first stage corresponds to 0.5° (0.5dt), and the second, finest timestep size equals the time in seconds, the runner requires to rotate 0.1° (0.1dt) of a full revolution.

In the same manner, additional simulations with three different mesh sizes are performed. Due to the considerable computational effort, each spatially refined setup invokes the most coarse timestep size dt. With the results, obtained for each different mesh size, the procedure of a grid independency study is performed and documented.

The influence of the total simulation time, is another topic considered in the scope of this thesis. Simulation time is conveniently expressed in terms of runner rotations. The simulation duration has been prolonged until approximately 70 full runner revolutions, in case of all simulations that invoke the coarse timestep size (dt). Almost 21 full rotations are simulated in case of the two temporally refined simulations (0.1dt and 0.5dt). The medium mesh size is considered in every setup, for each different timestep size.

The signal of each monitored global parameter (hydraulic efficiency η_h, head H, and mechanical power P_{mech}) along the simulation, is plotted against the simulation duration T_{sim}. On the basis of these global parameters, the different refinements (spatial and temporal) are compared against each other. The global parameters are also used in the evaluation of the grid independency study. Additional signals, that are tracked by monitor points, which are located at the draft tube wall, are

Die approbierte gedruckte Originalversion dieser Diplomarbeit ist an der TU Wien Bibliothek verfügbar
The approved original version of this thesis is available in print at TU Wien Bibliothek.
TU Bibliothek Your knowledge hub WIEN

presented as well.

Lastly, the occuring, large scale turbulence flow phenomenon, namely the rotating draft tube vortex rope, is visualised by the Q-criterion and compared between each spatially and temporally refined simulation.

Die approbierte gedruckte Originalversion dieser Diplomarbeit ist an der TU Wien Bibliothek verfügbar
The approved original version of this thesis is available in print at TU Wien Bibliothek.
TU Bibliothek Your knowledge hub WIEN

Kurzfassung

Die Arbeit befasst sich mit dem Einfluss unterschiedlicher Zeitschrittweiten, sowie der unterschiedlichen Anzahl an Elementen, auf die Simulationsergebnisse einer Francis Turbine, die im Teillastgebiet arbeitet. Simulationen, mit drei verschiedenen Zeitschrittweiten (in Sekunden), welche geschickterweise in Grad einer vollen Laufradumdrehung ausgedrückt werden, sind simuliert worden. Der gröbste Zeitschritt entspricht einer Laufradrotation von 1° (dt) einer ganzen Umdrehung. Dieser wurde im ersten Schritt halbiert (0.5dt) und die Zeitschrittweite von 0.1° (0.1dt) stellt die feinste zeitliche Auflösung dar.

Sinngemäß der Verfeinerung des Zeitschritts, wurden auch verschiedene Netzgrößen, simuliert. Angesichts der steigenden Elementanzahl sind diese mit grob, mittel und fein (coarse - medium - fine) betitelt. Da die Ergebnisse der Simulationen mit verschiedenen Netzgrößen den Ausgangspunkt einer Netzunabhängigkeitsstudie darstellen, wurde diese im Zuge der Arbeit ebenfalls durchgeführt.

Ein weiterer Aspekt, mit welchem sich die Arbeit beschäftigt, ist der Einfluss der Simulationsdauer. Um die Simulationsdauer greifbarer darzustellen, wird sie in Laufradrotationen dargestellt. Somit wurden nahezu 70 ganze Laufradrotationen, aller Simulationen, welche den groben Zeitschritt aufweisen, simuliert. Aufgrund der erheblichen Berechnungsdauer sind die Simulationen mit den verfeinerten Zeitschrittweiten (0.1dt und 0.5dt) nur ganze 21 Laufradrotationen simuliert worden. Die räumliche Grundlage, jede zeitlichen Verfeinerung, ist das Netz, welches die mittlere Zellenanzahl aufweist.

Während jeder Simulation sind diverse Größen, an definierten Punkten im Setup, aufgezeichnet worden. Alle Simulationsergebnisse und damit der Einfluss der zeitlichen und räumlichen Verfeinerung, werden anhand der definierten globa-

Die approbierte gedruckte Originalversion dieser Diplomarbeit ist an der TU Wien Bibliothek verfügbar
The approved original version of this thesis is available in print at TU Wien Bibliothek.

len Größen (Hydraulischer Wirkungsgrad η_h, Höhe H und mechanische Leistung P_{mech}) verglichen. Die selben globalen Größen werden im Zuge der Auswertung der Netzunabhängigkeitsstudie herangezogen. Das Signal weiterer, sogenannter Monitorpunkte an diversen Stellen der Saugrohrwand und der Einfluss der Verfeinerung (zetiliche, räumliche) auf dieses, wird ebenfalls dokumentiert.

Zu guter Letzt wird die großskalige Turbulenzerscheinung, der rotierende Wirbelzopf, für die verschiedenen zeitlich und räumlich verfeinerten Simulationen verglichen.

Die approbierte gedruckte Originalversion dieser Diplomarbeit ist an der TU Wien Bibliothek verfügbar
The approved original version of this thesis is available in print at TU Wien Bibliothek.

Contents

Die approbierte gedruckte Originalversion dieser Diplomarbeit ist an der TU Wien Bibliothek verfügbar
The approved original version of this thesis is available in print at TU Wien Bibliothek.
TU Wien Bibliothek Your knowledge hub

Die approbierte gedruckte Originalversion dieser Diplomarbeit ist an der TU Wien Bibliothek verfügbar
The approved original version of this thesis is available in print at TU Wien Bibliothek.

Nomenclature

Abbrevations

ARS	Algebraic Reynolds-stress
ASM	Algebraic stress model
BC	Boundary condition
BCD	Bounded central differencing scheme
BEP	Best efficiency point
BSL	Menter Baseline
CAES	Compressed-air energy storage
CFD	Computational fluid dynamics
DES	Detached-eddy simulation
DNS	Direct numerical simulation
DT	Draft tube
DTVR	Draft tube vortex rope
EVM	Eddy-viscosity model
FEM	Finite element method
FFT	Fast Fourier transformation
FL	Full-load
FVM	Finite volume method
GGI	General grid interface
GIS	Grid independecy study
GUI	Graphical user interface
GV	Guide vane
HPC	High performance cluster
HWL	Head water level
KVS	Kármán vortex shedding
LES	Large-eddy simulation
LHS	Left-hand side

Die approbierte gedruckte Originalversion dieser Diplomarbeit ist an der TU Wien Bibliothek verfügbar
The approved original version of this thesis is available in print at TU Wien Bibliothek.
TU Bibliothek Your knowledge hub WIEN

NS	Navier-Stokes
PDE	Partial differential equation
PHES	Pumped-hydro energy storage
PL	Part-load
PtG	Power-to-gas
R	Runner
RANS	Reynolds-averaged Navier-Stokes
RHS	Right-hand side
RMS	Root-mean square
RP	Rated point
RSI	Rotor-stator interaction
RSM	Reynolds-stress model
RST	Reynolds-stress transport
SAS	Scale-adaptive simulation
SC	Spiral case
SRS	Scale-resolving simulation
SST	Shear-stress transport
SV	Stay vane
TVR	Turbulent viscosity ratio
TWL	Tail water level
URANS	Unsteady RANS

Physical Constants

$\mathbf{g}$	Gravitational acceleration	$[\mathrm{m/s^2}]$
ρ	Density	$[\mathrm{kg/m^3}]$

Dimensionless Numbers

C_Q	Constant for Q-criterion	$[-]$
CFL	Courant-Friedrichs-Lewy number	$[-]$
Re	Reynolds number	$[-]$
U^+	Dimensionless velocity	$[-]$
y^+	Dimensionless wall distance	$[-]$

Variables

Δp_t	Total pressure difference	[Pa]
dt	Timestep size	[°]

Die approbierte gedruckte Originalversion dieser Diplomarbeit ist an der TU Wien Bibliothek verfügbar
The approved original version of this thesis is available in print at TU Wien Bibliothek.
TU Bibliothek Your knowledge hub WIEN

c_i	Absolute velocity component	[m/s]
$c_{1,2}$	Absolute velocity at runner inlet,outlet - optimum	[m/s]
$c'_{1,2}$	Absolute velocity at runner inlet,outlet - part-load	[m/s]
$c''_{1,2}$	Absolute velocity at runner inlet,outlet - full-load	[m/s]
D	Diameter	[m]
F_i	Blending functions	[−]
f_n	Runner rotational frequency	[Hz]
f_{BP}	Blade passing frequency	[Hz]
H	Head	[m]
k	Kinetic energy of turbulent fluctuations per unit mass	[m^2/s^2]
L	Integral length scale	[m]
l_{K41}	Kolmogorov length scale	[m]
L_{vK}	von Kármán length scale	[m]
n	Rotational speed	[min^{-1}]
n_q	Specific speed	[min^{-1}]
n_{11}	Unit speed	[min^{-1}]
P	Mean kinematic pressure	[m^2/s^2]
p	Kinematic pressure	[m^2/s^2]
P_h	Hydraulic power	[W]
p_i	Static pressure	[Pa]
P_m	Mechanical power	[W]
P_{RP}	Rated power	[−]
Q	Discharge	[m^3/s]
Q	Value of Q-criterion	[s^{-2}]
Q_{11}	Unit Discharge	[m^3/s]
Q_{SAS}	Source term in the SST-SAS turbulence model	[−]
t	Time	[s]
T_m	Turbine torque	[Nm]
t_{K41}	Kolmogorov time scale	[s]
$u_{1,2}$	Circumferential velocity at runner inlet,outlet - optimum	[m/s]
$u'_{1,2}$	Circumferential velocity at runner inlet,outlet - part-load	[m/s]
$u''_{1,2}$	Circumferential velocity at runner inlet,outlet - full-load	[m/s]
u_{K41}	Kolmogorov velocity scale	[m/s]
$w_{1,2}$	Relative velocity at runner inlet,outlet - optimum	[m/s]
$w'_{1,2}$	Relative velocity at runner inlet,outlet - part-load	[m/s]
$w''_{1,2}$	Relative velocity at runner inlet,outlet - full-load	[m/s]

Die approbierte gedruckte Originalversion dieser Diplomarbeit ist an der TU Wien Bibliothek verfügbar
The approved original version of this thesis is available in print at TU Wien Bibliothek.
TU Bibliothek Your knowledge hub WIEN

Y	Specific turbine energy	$[m^2/s^2]$
Y^*	Loss-free specific turbine energy	$[m^2/s^2]$
Y_h	Specific hydraulic energy loss	$[m^2/s^2]$
z_i	Geodetic height	[m]
z_{GV}	Number of guide vanes	[–]
z_{HWL}	Head water level	[m]
z_{TWL}	Tail water level	[m]
k	Wavenumber	[1/m]

Greek Symbols

α_i	Incidence angle of absolute velocity component, optimum	[°]
α_i'	Incidence angle of absolute velocity component, part-load	[°]
α_i''	Incidence angle of absolute velocity component, full-load	[°]
β_i	Incidence angle of relative velocity component, optimum	[°]
β_i'	Incidence angle of relative velocity component, part-load	[°]
β_i''	Incidence angle of relative velocity component, full-load	[°]
δ	Turbulent shear layer thickness	[m]
ϵ	Turbulent dissipation per unit mass	$[m^2/s^3]$
η_h	Hydraulic efficiency	[%]
κ	von Kármán constant	[–]
μ	Dynamic viscosity	[Pas]
ν	Kinematic viscosity	$[m^2/s]$
ν_t	Eddy viscosity	$[m^2/s]$
ω	Angular velocity/Rate of turbulent dissipation	$[s^{-1}]$
ϕ	Guide vane opening angle	[°]
σ_k	Closure coefficient	[–]

Vectors, Tensors, Matrices

$\boldsymbol{\Omega}$	Skew- tensor
$\boldsymbol{\sigma^R}$	Reynolds-stress tensor
$\boldsymbol{\sigma}$	Cauchy-stress tensor
$\boldsymbol{\tau^R}$	Specific Reynolds-stress tensor
$\boldsymbol{\tau}$	Shear-rate tensor
$\mathbf{C_f}$	Cell face centre vector
$\mathbf{C}$	Cell centre vector
$\mathbf{I}$	Identity matrix

Die approbierte gedruckte Originalversion dieser Diplomarbeit ist an der TU Wien Bibliothek verfügbar
The approved original version of this thesis is available in print at TU Wien Bibliothek.
TU Bibliothek Your knowledge hub WIEN

$\mathbf{S}$	Mean strain-rate tensor
$\mathbf{s}$	Strain-rate tensor
$\mathbf{U}$	Mean velocity component vector
$\mathbf{u}$	Velocity component vector
$\mathbf{u}'$	Fluctuating velocity component vector
$\mathbf{x}$	Spatial coordinate vector

Superscripts

*	Loss-free

Subscripts

1	Fine
1	Inlet
2	Medium
2	Outlet
3	Coarse
i	Index
m	Meridional velocity amount
u	Circumferential velocity amount

Die approbierte gedruckte Originalversion dieser Diplomarbeit ist an der TU Wien Bibliothek verfügbar
The approved original version of this thesis is available in print at TU Wien Bibliothek.

Die approbierte gedruckte Originalversion dieser Diplomarbeit ist an der TU Wien Bibliothek verfügbar
The approved original version of this thesis is available in print at TU Wien Bibliothek.

Chapter 1

Introduction

When it comes to electricity storage on a large scale there are several options available e.g. CAES (Compressed-air energy storage), PtG (Power-to-gas) approaches, chemical storage as well as battery solutions. While the above mentioned technologies are expected to become more advanced in the near future, PHES (Pumped-hydro energy storage) systems represent the most competitive and only mature solution in terms of large-scale electricity storage (10-600GWh) at present. In addition, PHES's offer a wide range of grid managemement services which play an important role in maintaining the electrical grid resilience. Grid fluctuations due to feeding our power grid with volatile energy sources such as wind-, or solar power are conveniently counteracted by means of PHES. [1]
Summing up advantages such as large storage efficiency, low operation and maintenance costs, fast response-time i.e. operation-mode switch from pumping to generating within minutes to seconds, high global roundtrip efficiencies (75-82%), long lifetime (50-100 years) and gaining more concern as of late: 'black-start' capability (restarting the electric grid after a blackout) substantiates PHES's important position considering electricity supply. [1, 2]

The main side effect of compensating the unstable output of such volatile energy sources to the electrical grid on one hand, while also providing for peak power production to ancillary services on the other, is the requirement of these hydraulic turbines to operate at off-design conditions more frequently. Part-load, low-load, and full-load as well as numerous start-stop cycles are accompanied by certain flow phenomena causing strong vibrations induced by high pressure pulsations

on Francis runners. Resulting high dynamic stresses decrease the design lifetime. Therefore a hydro power plant owner feels the need to increase operating costs. The importance of quantifing such costs by the virtue of damaging factors over a whole operating range, especially in off-design conditions including start-stop procedures, needs no further explaination. [3]

CFD (Computational fluid dynamics) in combination with site measurements to verify numerical solutions proves as valuable tool along the way, prior to fatigue analysis and further lifetime assessment. Extracted pressure fields from a numerical (CFD) solutions serve as input for the FEM (Finite element method) analysis of a Francis runner that is investigated. Visualisation of other field quantities can support insights on operating behaviour and the occuring flow phenomena to a greater extent. Needless to say the necessity for accurate CFD results is crucial.

1.1 Thesis Outline

On the basis of contributions made by predecessors, the thesis aims to investigate the influence of spatial as well as temporal parameters in a numerical simulation of a Francis runner. Efforts made by J. Unterluggauer [4] during the course of GSG (Green storage grid) and it's follow-up project MDREST (Development of method for the life time prediction of hydraulic turbines by means of machine diagnostics) as well as the supplementing work by A. Schmelz [5] among others, with sole focus on their underlying CFD approach are revisited. In comparison to their conducted simulations, the numerical setup was remained the same with the only difference of changing spatial (number of elements) and temporal (refined timestep size) parameters. Additionally, the dependency of the solution on the total simulation time and results of a GIS (Grid independecy study) in part-load operating conditions are adressed in the scope of this thesis. The author is thankful for the given possibility and hopes to contribute to the project DIGI-Hydro (Digitalisation and visualisation forming a basis for predictive maintenance in hydropower) under guidance of his mentor and project leader Ass.Prof. Dipl.-Ing. Dr.techn. Eduard Doujak.

Die approbierte gedruckte Originalversion dieser Diplomarbeit ist an der TU Wien Bibliothek verfügbar
The approved original version of this thesis is available in print at TU Wien Bibliothek.
TU Bibliothek Your knowledge hub WIEN

Chapter 2

Fundamentals

After briefly discussing a Francis runner's main characteristics, the dynamic fluid flow phenomena experienced at different operating conditions will be summarized. Furthermore, a short history of CFD applied to Francis runner set-ups will be the main emphasis of this chapter.

2.1 Francis Turbine

Classification of hydraulic turbomachines is most common by means of specific speed n_q defined as:

$$n_q = n\frac{\sqrt{Q}}{H^{0.75}} \tag{2.1}$$

Dependent on discharge Q, heads H in the range between 50m up to 700m and rotational speed n, Francis runners are located at specific speeds ranging from 20rpm $\leq n_q \leq$ 120rpm. Along with highest hydraulic efficiencies ($> 96\%$ [7]) and power output of more than 800MW among water turbines, Francis runner's ability

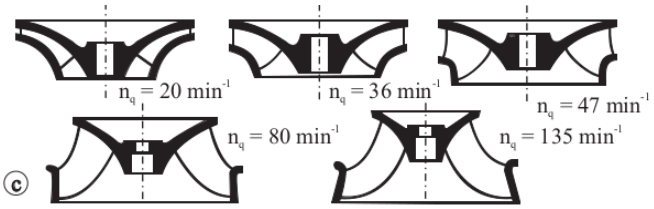

Figure 2.1: Types of Francis runners depending on specific speed n_q [6]

Die approbierte gedruckte Originalversion dieser Diplomarbeit ist an der TU Wien Bibliothek verfügbar
The approved original version of this thesis is available in print at TU Wien Bibliothek.

to work in pumping mode substantiates it's numerous deployment when considering PHES. Several concepts and their functionality are provided in [8].

Figure 2.1 displays different runner geometries based on n_q. Smaller specific speeds (high head runners) yield more radially shaped, narrow blade channels where as on the other end, a more axial shape with larger blade channels is implemented for medium and low head runners (large specific speeds). Several blades are connected to the hub on the top side and to the shroud on the bottom of a runner. Waterways through a turbine are conveniently decomposed into five domains as depicted in figure 2.2. Headwater is distributed by means of a spiral case (1) via stay vanes (2) and adjustable guide vanes (3). While those three components are required to convert headwater pressure into angular momentum, stay vanes are additionally responsible for mechanically strengthening the spiral case as well for providing an equal distribution of water flow. Guide vanes are in control of the flow rate. After radially entering the runner (4) at it's inlet, water flow exits in axial direction at the so-called suction side of the runner followed by a draft tube (5). It's purpose is to decelerate the flow in order to increase turbine efficiency. The generated torque is converted into electricity by means of a generator connected to the runner hub via a shaft ((6)).

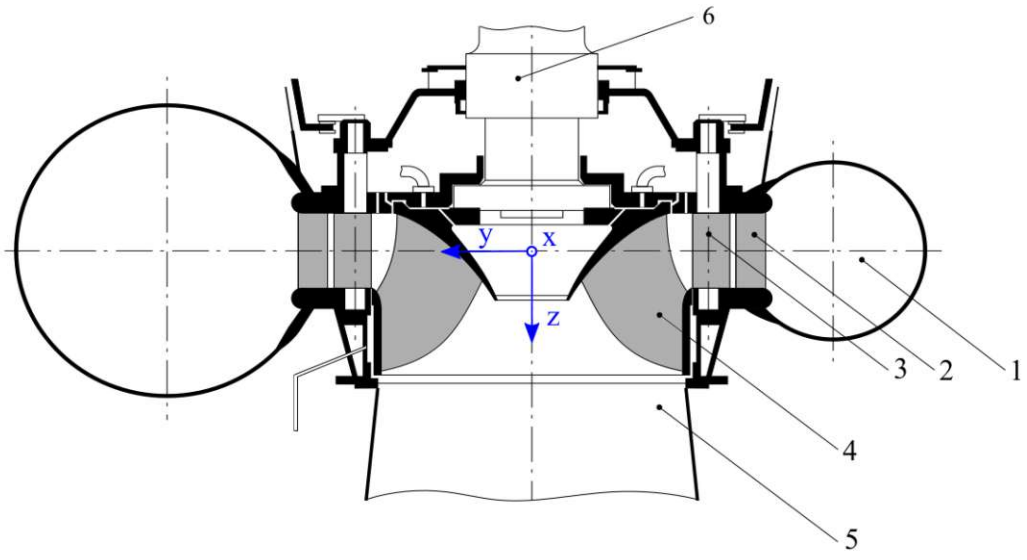

Figure 2.2: Meridional plane of Francis runner [4]

Die approbierte gedruckte Originalversion dieser Diplomarbeit ist an der TU Wien Bibliothek verfügbar
The approved original version of this thesis is available in print at TU Wien Bibliothek.

2.1.1 Energy Conversion

Bernoulli's theorem for an incompressible ($D_t\rho = 0$), homogeneous ($\rho = const.$) fluid flow states constant specific energy along a streamline. Loss-free specific energy Y^* of a fluid particle flowing along a streamline from the inlet (1) to the outlet (2) (fig. 2.3) through a runner blade channel can be expressed in terms of total pressure difference Δp_t [9]:

$$\begin{aligned} \rho Y^* &= p_1 - p_2 + \rho\frac{c_1^2 - c_2^2}{2} + \rho g(z_1 - z_2) \\ \Delta p_t &= \Delta p + \rho\frac{\Delta c^2}{2} + \rho g \Delta z \end{aligned} \tag{2.2}$$

The total pressure difference Δp_t is calculated with static pressures p_1/p_2, mass averaged quadratic flow velocities c_1/c_2, geodetic heights z_1/z_2 and constants namely water density ρ and local gravitational acceleration g.

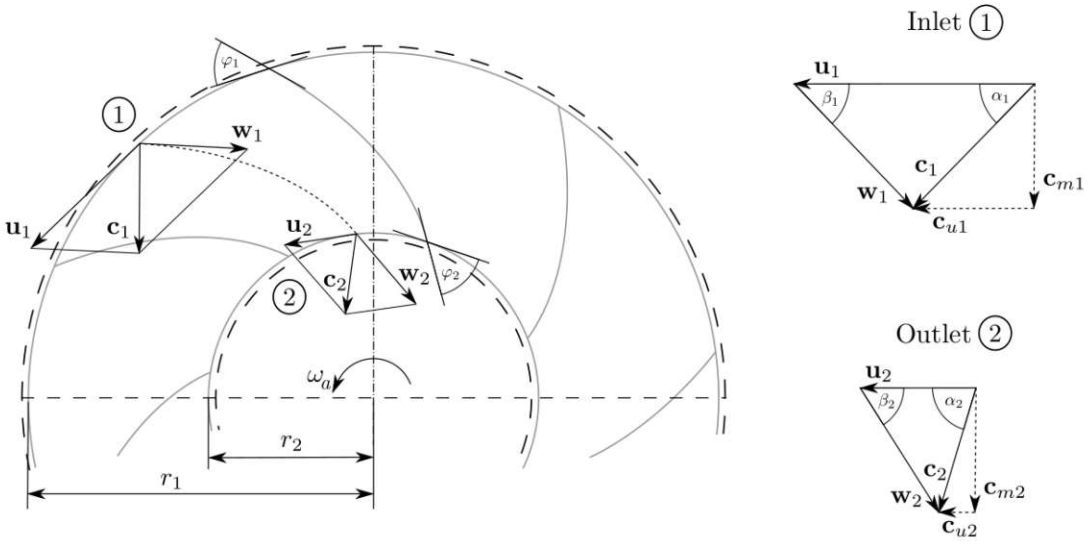

Figure 2.3: Flow along streamline through radial runner and velocity triangles [10]

With net water head H and the correlation $Y^* = gH$, the total pressure difference between sections 1-1 and 2-2 (fig. 2.4) can be expressed as [9]:

$$H = \frac{\Delta p_t}{\rho g} \tag{2.3}$$

Die approbierte gedruckte Originalversion dieser Diplomarbeit ist an der TU Wien Bibliothek verfügbar
The approved original version of this thesis is available in print at TU Wien Bibliothek.

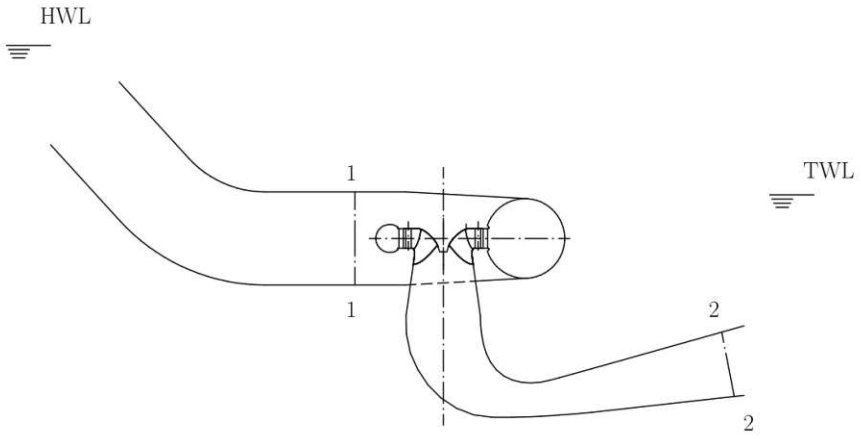

Figure 2.4: Conceptual water levels and measuring planes [9]

The net water head can be obtained by taking the difference $z_{HWL} - z_{TWL}$, between head and tail water level and accounting for losses at the inlet (HWL→1-1) and outlet (2-2→TWL) circuits. Sections 1-1 and 2-2 schematically represent turbine measuring planes which are invoked at the same location in the numerical setup. Averaged field values are monitored at these planes during a simulation.

While the available hydraulic power can be derived from the infamous Euler turbine equation given in [7], it can also be defined using the loss-free specific energy Y^* and discharge Q [2]:

$$P_h = \rho Q Y^* = \rho Q g H \tag{2.4}$$

Available specific energy Y results in Y^* subtracted by losses (hydraulic loss Y_h) due to friction an turbulence. The hydraulic efficiency is then expressed as:

$$\eta_h = \frac{Y}{Y^*} = \frac{Y^* - Y_h}{Y^*} \tag{2.5}$$

and can be equivalently given in terms of available mechanical turbine power at the shaft P_m or turbine torque T_m (and angular velocity ω), divided by available hydraulic power P_h:

$$\eta_h = \frac{P_m}{P_h} = \frac{T_m \omega}{\rho Q g H} \tag{2.6}$$

Die approbierte gedruckte Originalversion dieser Diplomarbeit ist an der TU Wien Bibliothek verfügbar
The approved original version of this thesis is available in print at TU Wien Bibliothek.

2.1.2 Velocity Triangles

Taking equation (2.4) into consideration and assuming a constant net head H, power output regulation can only be realized by varying discharge Q. In a Francis runner application this is implemented by means of adjustable guide vane openings. As a result of guide vane movement (i.e. variation of guide vane angle ϕ), discharge is set to achieve desired power output and different operating points are obtained. Figure 2.6 shows resulting runner velocity triangles influenced by certain guide vane positions. Three main operating points can be distinguished namely BEP (Best efficiency point), PL (Part-load), and FL (Full-load). It is important to notice the changing circumferential amount c_{u2} at the outlet. For example this reaches from vanishing (BEP), to $c'_{u2} \neq 0$ (PL), to c''_{u2} pointing in the opposite direction of rotating velocity u_2.

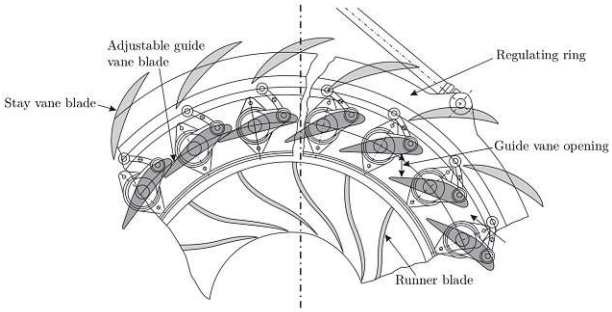

Figure 2.5: Guide vane movement [6]

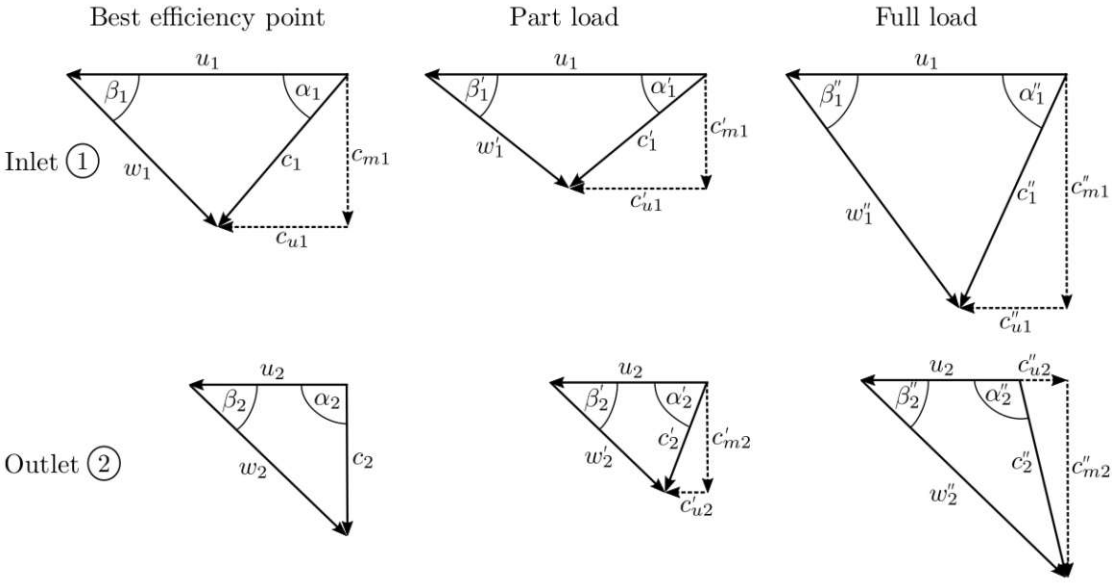

Figure 2.6: Francis runner velocity triangles obtained at different operating points [2]

Die approbierte gedruckte Originalversion dieser Diplomarbeit ist an der TU Wien Bibliothek verfügbar
The approved original version of this thesis is available in print at TU Wien Bibliothek.

2.2 Operating Region & Unsteady Flow Effects

Prior the installment of a prototype runner, it is common to test it's operating behaviour by means of a geometrically similar model runner. Characteristics gathered from model testing are described using a hill chart. The model hill chart can be transposed to a prototype runner hill chart utilizing equations for unit speed n_{11} and unit discharge Q_{11}:

$$Q_{11} = \frac{Q}{D^2\sqrt{H}} \qquad n_{11} = \frac{nD}{\sqrt{H}} \tag{2.7}$$

Unit entities correspond to a geometrically similar turbine with runner diameter of $D = 1\text{m}$ and net water head $H = 1\text{m}$. Typical hill charts include iso-curves of efficiency levels as well as constant guide vane opening (angle) iso-lines (see fig. 2.7 left). While operating points on the basis of velocity triangles have already been discussed, figure 2.7 (right) schematically splits the hill chart into regions named after their most prominent unsteady flow effects that occure within those regions. These dynamic flow phenomena lead to pressure oscillations, that not only

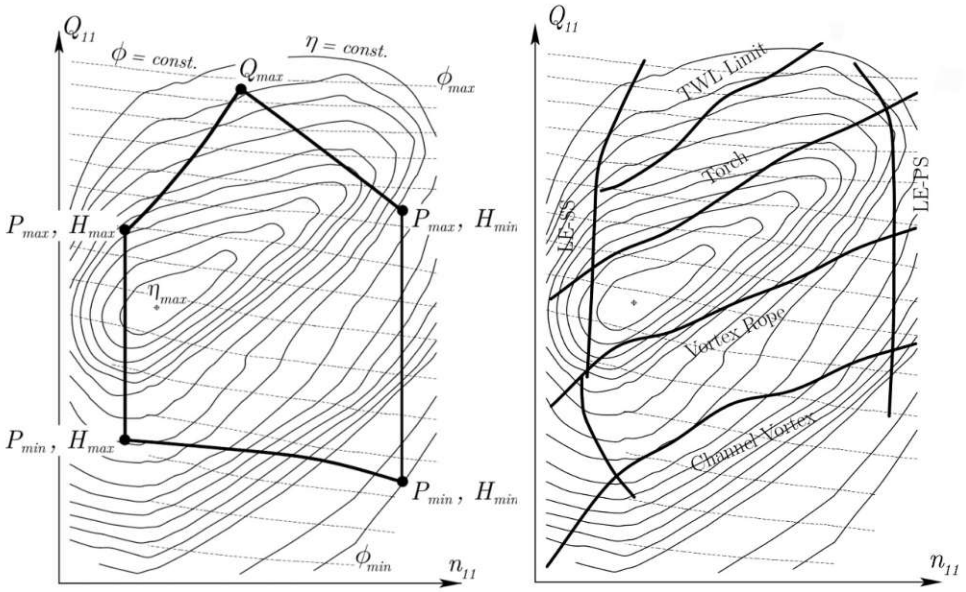

Figure 2.7: Hill chart, operation region and regions of unsteady flow effects [2, 9]

influence the operating mode, but also may cause damage to structual components. A typical hydraulic energy producers requirement is that the pressure pulsation amplitude remains below predefined limits. The pressure pulsation amplitude is

Die approbierte gedruckte Originalversion dieser Diplomarbeit ist an der TU Wien Bibliothek verfügbar
The approved original version of this thesis is available in print at TU Wien Bibliothek.

commonly associated with the hydraulic stability of Francis turbines. [11]

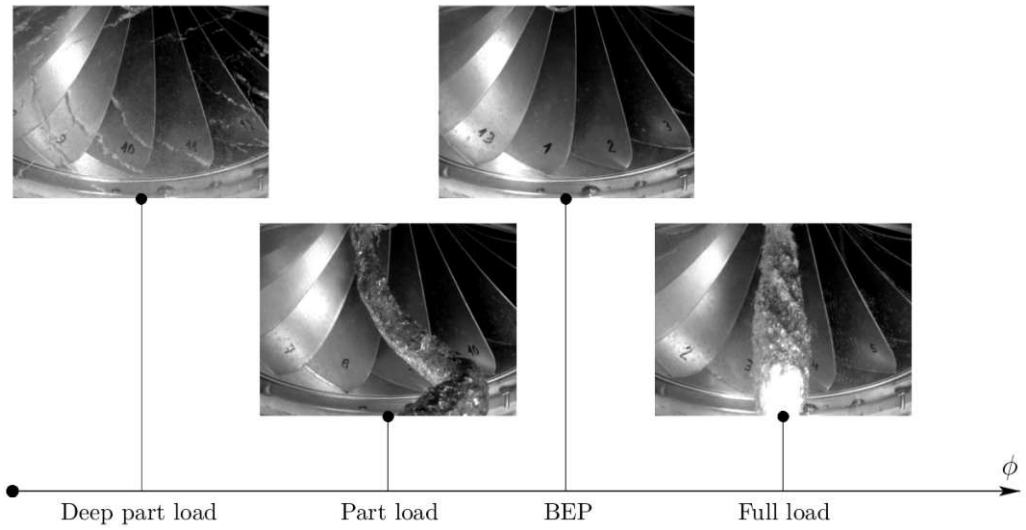

Figure 2.8: Visualized unsteady flow phenomena [2]

Following explaination of unsteady flow effects tries to summarize their describtion found in Phd Thesis' of Eichhorn [2], Unterluggauer [4] and Magnoli [9].

Best efficiency point

The region closely located around the optimum, BEP, is considered as "rope free zone". Hardly any swirling appearance as well as a homogeneous velocity profile are the reason for relatively low dynamic pressure oscillations. Furthermore, draft tube cone pressure is high enough to prevent the flow from cavitating. Most present dynamic phenomenon (omnipresent over the whole operating range) occuring in the rope free region is the RSI (Rotor-Stator Interaction) as a result of the rotating runner passing stationary guide vanes. The source of this effect is the inhomogeneous pressure distribution along the spiral case as well as guide vane wakes entering the rotating runner. Excitation of the runner through spiral case pressure distribution happens at runner's rotating frequency f_n while guide vane wakes excite the runner at the blade passing frequency z_{BP} (z_{GV} equals number of guide vanes):

$$f_{BP} = z_{GV} f_n = z_{GV} \frac{n}{60} \tag{2.8}$$

In conclusion, this phenomenon mostly effects the runner inlet section.

Die approbierte gedruckte Originalversion dieser Diplomarbeit ist an der TU Wien Bibliothek verfügbar
The approved original version of this thesis is available in print at TU Wien Bibliothek.
TU Bibliothek Your knowledge hub WIEN

Part-load

Observation of a rotating vortex rope appearing in the draft tube cone directly corresponds to an operating point in part-load region (see fig. 2.7 and 2.8). Already subject to many research projects, it's pressure oscillation frequency is below runner frequency in the range of $0.2f_n \div 0.4f_n$. The vortex rope's shape and it's rotating character is influenced by volume flow rate and runner outlet swirl. Due to lower flow rates in the region below BEP (rope free region), a high residual swirl exits the runner outlet and enters the draft tube. Surplus kinetic energy is transformed into static pressure. The decelerated swirl, unsteady itself, causes a highly unsteady pressure field and as a result a helix shaped vortex rope forms and rotates in runner direction. [12]

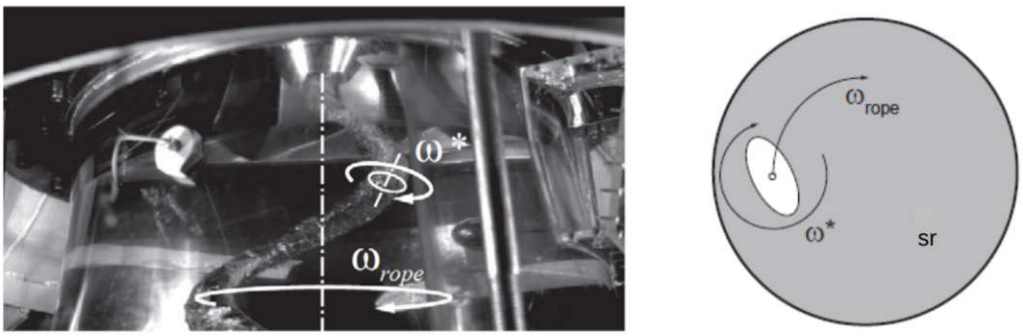

Figure 2.9: Vortex rope, graphics adapted from [13]

While pressure oscillations due to this phenomenon are often experienced at the whole machine set, the part-load vortex rope may be accompanied by cavitation. The self rotation angular velocity of the vortex rope (ω^* in fig. 2.9) can lead to a significant pressure drop in the core region of the vortex and vaporization at low temperatures becomes possible.

Deep part-load

Just narrated behaviour becomes even more pronounced when further decreasing discharge Q. Runner outlet swirl becomes more intense, again resulting in a draft tube vortex. The set-in of channel vorticies (fig. 2.8) marks the beginning of this often called low-load zone. Inter-blade vorticies are originated by flow seperations in the runner, mostly taking place at the leading edge.
While the shape of this inter-blade flow phenomenon closely reflects a hairpin vortex, (see [14]) both, the helix shaped vortex rope and hairpin vorticies along

Die approbierte gedruckte Originalversion dieser Diplomarbeit ist an der TU Wien Bibliothek verfügbar
The approved original version of this thesis is available in print at TU Wien Bibliothek.
TU Bibliothek Your knowledge hub WIEN

runner blades, form a core with high rotating velocities around it leading to low pressure zones in the vortex core. A pressure drop below vapor pressure results in liquid's evaporation, origin to all cavitating circumstances. [15]

Full-load
Changing direction of circumferential amount (c''_{u2} in fig. 2.6) due to increased discharge results in a counter-rotating swirl. In cases of high local flow acceleration - going hand in hand with a static pressure drop - pressure might drop below fluids vapor pressure resulting in a cavitating torch light shaped vortex (see fig. 2.8). Resulting pressure fluctuation of this phenomenon is usually small by reason of a relative stable flow condition, making the RSI the highest remaining effect exciting the runner in full-load operation.

Additional experienced flow phenomena such as KVS (Kármán vortex shedding) and subdivision of part-load region into higher part-load and part-load zone, as well as the small region of full-load instability occurance is thoroughly given in [4] and [11]. Numerical investigation of **No-load** operating conditions and important findings regarding it's CFD approach are given in [16].

2.3 Historical View and Influencing Parameters in a Francis Runner CFD Simulation

Although rising computational power and the progress made in numerical methods in the early 1970s were promising, the bigger challenge at that time seemed to be the introduction of this new method. With CFD already being found in literature and key modifications to the most famous two-equation turbulence model (k-ϵ) accomplished by 1978, acceptance, or even familiarity by engineers in the field of hydraulic turbine design was lacking. It was the capability of the FEM to model complex geometries with good accuracy that brought first true success to CFD modeling turbine flow. The evolution from the "quasi-3D" approach (splitting flow region into meridional and blade-to-blade flow) initially invoking "Laplace Equation" (potential flow solver) to a fully 3D-Euler analysis, and it's ability leading to the first numerically modeled vorticity driven secondary flow often observed in test rigs at off-design conditions (fig. 2.10), is well documented in [17].

Die approbierte gedruckte Originalversion dieser Diplomarbeit ist an der TU Wien Bibliothek verfügbar
The approved original version of this thesis is available in print at TU Wien Bibliothek.

Figure 2.10: 3D Euler code modeled leading edge vortex in 1989 [17]

After successfully modeling flow through stationary and rotating sections in one simulation, the first numerical hill chart of a Francis runner was published in 1996. The deviation to measured absolute efficiency and the well reflected shape of prototyp hill chart showed both the enormous potential but also limitations of this new method. Neglecting not only viscous effects, but also turbulence (Euler approach), the CFD tool was continuously solidified by the introduction of RANS (Reynolds-averaged Navier-Stokes) equations and became state-of-the-art by 2000. This new approach, taking both into account (viscosity and turbulence), allowed for a far more realistic flow simulation as well as loss analysis and prediction of flow seperation. Being inherently conservative with respect to mass and momentum, most development with commercial software developer (ASC, CFX and now ANSYS) was made using the FVM (Finite volume method) approach to model fluid flow. [17]

Trying to numerically predict the draft tube vortex's complex and unsteady flow behaviour by means of CFD started in 2001. Accurate simulation of such a flow phenomenon determined by both large and small scale vorticity dynamics are particularly dependent on the applied turbulence model. An important finding at that time resorted to the finding, that the standard k-ϵ model overpredicts turbulence intensity, since the effect of streamline curvature on turbulence production is wrongly taken into account. To remedy this poor approximation RSM (Reynolds-stress model) and other two-equation models with streamline curvature correction were

Die approbierte gedruckte Originalversion dieser Diplomarbeit ist an der TU Wien Bibliothek verfügbar
The approved original version of this thesis is available in print at TU Wien Bibliothek.
TU Bibliothek Your knowledge hub WIEN

able to deliver more reliable results. In addition, grid resolution was found to be another important numerical parameter crucial for an accurate prediction of the helical vortex tube. This circumstance came even more pronounced not only for two-phase flow analysis of a cavitating draft tube vortex but also for simulations of the increasing non-symmetrical flow patterns, dominant in part-load condition. Quite remarkable on the other hand at that time (2006) was the fact that not only major excitation frequencies of omnipresent RSI, but even amplitudes of resulting pressure pulsations, could already be predicted quite accuratly by means of CFD. [18]

Being a notoriously difficult application when put into practice explains certain dicta for CFD such as "Cheats, Frauds and Deceivers" or "Colors For Directors". Trying to counteract this notion, several workshops on validation of method and results have been organized by the European Research Community on Flow, Turbulence and Combustion (ERCOFTAC). A review of the well-known "Francis-99" test case is given in [19]. The main author also published a paper documenting the state of the art in numerical simulation of Francis turbines in 2016 [20]. Outcomes of contributions cited up to this point shall narrow down further upcoming investigation of Francis runner CFD simulation's influencing parameters.

As already stated and turbulence being one of the classical, yet in many basic questions to an unsatisfactory level understood scientific subject, applied turbulence model has a major influence on outcoming results. Independet of the chosen model, the fact that turbulence is naturally irregular and showes anything but periodic behaviour, allows for simple argumentation which substantiates the requirement for complete model simulations. Component (e.g. only runner and draft tube domain) as well as passage (sector model of spiral case, guide vanes and one runner channel) modeling for the sake of computational effort imposes assumed and/or periodic BC (Boundary condition) at interfaces which improperly mimics the actual circumstance and forces periodicity on simulated turbulence carried by the fluid flow.

A properly chosen turbulence model needs to go hand in hand with specific mesh criteria. While mesh quality on it's own influences solution convergence, numerical stability and outcoming results, mesh size (the number of cells), is the overall key parameter regarding the computational domain. Cell counts for a complete turbine simulation are range from 4.3 million to 20 million (48 mio. with modeled labyrinth

Die approbierte gedruckte Originalversion dieser Diplomarbeit ist an der TU Wien Bibliothek verfügbar
The approved original version of this thesis is available in print at TU Wien Bibliothek.
TU Bibliothek Your knowledge hub WIEN

seals [21]) in the course of Francis-99. According to the authors knowledge, simulations reaching up to 250 and even 300 million cells ([22], [23] and [24]) represent the highest cell counts achieved in this field so far.

GIS or "mesh scaling tests" are often carried out by performing simulations with identical numerical setup but using different cell counts (e.g. coarse - medium - fine). While a steady state simulation on it's own is only reasonable to acquire an initial solution for upcoming unsteady calculations, GIS are, on top of their steady state character, commonly carried out at BEP operating condition. Under guidance of the author's mentor, the decision towards performing a GIS for unsteady calculations in part-load operating condition was made and is hoped to yield insights on how the mesh size influences this highly dynamic part-load flow beaviour.

Lastly, the influence of different timestep sizes corresponding to the degree (fractions of the degree) of a runner revolution, as well as the number of fully simulated runner rotations will be investigated.

Die approbierte gedruckte Originalversion dieser Diplomarbeit ist an der TU Wien Bibliothek verfügbar
The approved original version of this thesis is available in print at TU Wien Bibliothek.

Chapter 3

Francis Runner CFD

Understanding (computational) fluid dynamics underlying mathematics on it's own is not simple. Putting this knowledge into practice using any current CFD software available can become a daunting task. While commercial providers (Ansys Fluent, Ansys CFX, Simcenter STAR-CCM+) are already trying to ease up its toolbox' usage by introducing a neat GUI (graphical user interface), the open-source software in the field of CFD - OpenFOAM - requires additional skill such as code based input. Regardless of the software put into practice, profound knowledge of underlying equations and their discretisation, different schemes approximating derivatives, numerical algorithms and solvers, turbulence modeling and applied BC is indispensable. Coming to terms with this enables application of basically every CFD software available and softens their overwhelming character significantly.

3.1 Governing Equations

Although governing equations have been known for centuries, an analytical solution to fluid flows underlying system of PDEs (partial differential equations) can only be achieved, by invoking substantial simplifying assumptions. In general, analytical solutions to PDEs only exist for rather trivial ones. Their ubiquitous nature in scientific fields that obey mathematical laws have led to numerous numerical approximating methods. The purpose of such methods is to transform PDEs into a corresponding system of much simpler algebraic equations. This process will be

Die approbierte gedruckte Originalversion dieser Diplomarbeit ist an der TU Wien Bibliothek verfügbar
The approved original version of this thesis is available in print at TU Wien Bibliothek.
TU Bibliothek Your knowledge hub WIEN

concerned in more detail in the upcoming chapter.

As Leonardo da Vinici's famous sketches of his "Studies of Water passing Obstacles and falling" ([25]) depict, the approach to define fluid flows motion strictly resorts to the framework of continuums mechanic. This is also true for turbulent flow behaviour - even the smallest scales occuring in a turbulent flow are ordinarily far larger than any molecular length scale. This allowes for the describtion of (macroscopic) physical properties as continuous functions in macroscopic coordinates (time and space). The motion of (incompressible) fluid flow can fully be described by flow velocity components $\mathbf{u}$ and pressure value p at every spatial coordinate $\mathbf{x}$ of a control volume, at every instant of time t. [26, 27]

Prior the formulation of fluid flows conservation laws (i.e. mass, momentum and energy conservation) the total derivative operator[1]

$$\boxed{\mathrm{D}_t = \frac{\partial}{\partial t} + \mathbf{u} \cdot \nabla} \tag{3.1}$$

is invoked. Aside it's purpose to reformulate, and in doing so make equations look more appealing, the very important case of an *incompressible* fluid is defined as $\mathrm{D}_t\rho = 0$.

Conservation of mass, commonly named continuity equation reads as:

$$\boxed{\frac{\partial \rho}{\partial t} + \nabla \cdot (\rho \mathbf{u}) = 0} \tag{3.2}$$

Single-phase water flow is approximated to be incompressible hence suffering a *solenoidal's* field restriction leading to continuity equation in it's reduced from:

$$\frac{\partial \rho}{\partial t} + \nabla \cdot (\rho \mathbf{u}) \rightarrow \underbrace{\frac{\partial \rho}{\partial t} + \mathbf{u} \cdot \nabla \rho}_{\mathrm{D}_t\rho=0} + \rho \nabla \cdot \mathbf{u} \Rightarrow \boxed{\nabla \cdot \mathbf{u} = 0} \tag{3.3}$$

Several approaches that treat two-phase fluid flow are well documented in [29].

Conservation of linear and angular momentum i.e. Cauchy's first and second law of motion (1827), state symmetry of Cauchy's stress tensor ($\boldsymbol{\sigma} = \boldsymbol{\sigma}^t$). Strict

[1] Basic tensor algebra and as well as explaination of used notation is thoroughly given in [28]

Die approbierte gedruckte Originalversion dieser Diplomarbeit ist an der TU Wien Bibliothek verfügbar
The approved original version of this thesis is available in print at TU Wien Bibliothek.

LTE (local thermodynamic equilibrium) simplifies the decomposition of $\boldsymbol{\sigma}$ in it's deviatoric (Shear-rate tensor $\boldsymbol{\tau}$) and spherical component (negativ pressure $-p$) and leads to momentum equation (conservation of momentum) that, for the sake of brevity, neglects any external field forces (e.g. gravitational force):

$$\boxed{\rho \mathrm{D}_t \mathbf{u} = -\nabla p + \nabla \cdot \boldsymbol{\tau}} \tag{3.4}$$

In addition to water's incompressibility, flow through a Francis runner is approximated to be isothermal ($\Delta T = 0$) qhich allowes to omit further derivation of energy conservation equation in the scope of this thesis. The energy conservation equation when dealing with compressible, and/or non-isothermal flow as well as required equations of state and second constitutive relationship in order to close this undetermined system of equations, are provided in basically all referenced textbooks.

The first constitutive relationship required to proceed further termed *Newtonian fluid* has it's orgin in 1687 (*Philosophiae Naturalis Principia Mathematica* [30]). Isaac Newton (1642-1727) was the first to relate momentum transport on a molecular base, namely shear stress or drag, to the velocity gradient or rate of shear strain by a scalar constant of proportionality (viscosity μ). While several restrictions on viscous stresses are made when deriving the *Newtonian fluid* approximation, the most essential two properties are: [30, 31]

- **static dependency** of $\boldsymbol{\tau}$ on $\nabla \mathbf{u}$: neglecting viscoelastic effects hence neither time derivatives nor time integration takes place in expression
- **isotropic fluid**: fluid has no preferred direction (typical fluid property)

These are very well alligned with Bird et al.'s [32] more profound description of all restrictions made when deriving the *Newtonian fluid* constitutive relation. Even though the outcoming equation approximating $\boldsymbol{\tau}$ reads rather trivial, it took mathematicians more than a century to generalize Newton's one dimensional procedure and extend it to three dimensions. Since an incompressible, *Newtonian fluid* flow is considered, the often encountered familiar *Stokes hypothesis* is superflous and shall remain mentioned. Incompressible fluid flow's solenoidal $\mathbf{u}$-field reduces the symmetric, linear combination of velocity gradients (see Bird et al. [32]) right away to:

$$\boxed{\boldsymbol{\tau} = 2\mu\mathbf{s}}, \qquad \mathbf{s} = \mathrm{sym}(\nabla \mathbf{u}) = \frac{1}{2}\left(\nabla \mathbf{u} + \nabla \mathbf{u}^t\right) \tag{3.5}$$

Small lettering of $\mathbf{s}$ (Strain-rate or Deformation-rate tensor) will become obvious

Die approbierte gedruckte Originalversion dieser Diplomarbeit ist an der TU Wien Bibliothek verfügbar
The approved original version of this thesis is available in print at TU Wien Bibliothek.
TU Bibliothek Your knowledge hub WIEN

when deriving RANS equations.
On the verge of jumping into turbulence, a common starting point (Scheichl [31], Wilcox [33], Davidson [14],.. all use the exact same starting point) for it's investigation, in fact the underlying set of equations for a:

- *homogeneous* ($\rho = \text{const.}$ throughout domain),
- *incompressible* ($\mathrm{D}_t\rho = 0$),
- *Newtonian fluid* ($\boldsymbol{\tau} = 2\mu\mathbf{s}$)

fluid, often considered as the Navier-Stokes Equations, reads as:

$$\boxed{\begin{aligned} \nabla \cdot \mathbf{u} &= 0 \\ \rho\frac{\partial \mathbf{u}}{\partial t} + \rho\nabla\cdot(\mathbf{uu}) &= -\nabla p + \nabla \cdot 2\mu\boldsymbol{s} \end{aligned}} \tag{3.6}$$

Going from left to right (bottom eq. 3.6), the terms are titled temporal-, convective-, pressure gradient- and diffusion-term.

3.2 Turbulence and it's Modeling

Osborne Reynolds' (1832-1912) famous pipe and channel flow experiments led to the familiar demarcation of turbulent from laminar flow. The appearance of "slugs" and "puffs" depicted in figure 3.1 at a critical threshold of Reynolds number Re, represents one of the first visualisations of a turbulent flow. Already observed in one

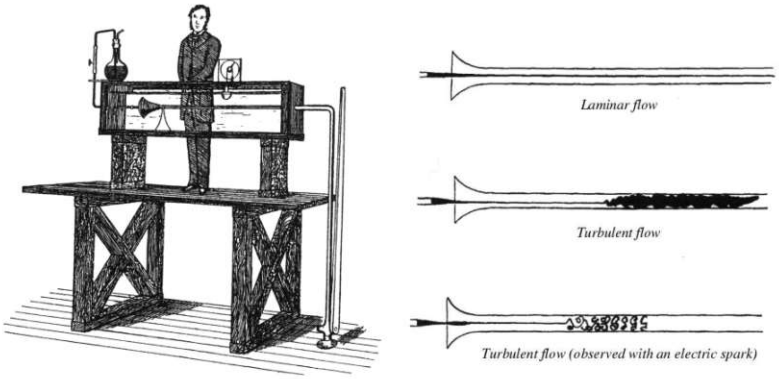

Figure 3.1: Reynolds' experimental set-up and visualisations (originally by dye injected into water) [31]

Die approbierte gedruckte Originalversion dieser Diplomarbeit ist an der TU Wien Bibliothek verfügbar
The approved original version of this thesis is available in print at TU Wien Bibliothek.

of THE classical literature on turbulence ([26]), most flows occuring in nature and engineering applications are turbulent. Laminar flow is the exception (e.g. journal bearing). Resorting to the classical "definition" rendering a flow turbulent, necessary ingredients are (I) unsteadiness, (II) three-dimensionality, (III) the presence of vortices, i.e. non-vanishing vorticity (traced back to non-vanishing viscosity). A fourth requirement, (IV) randomness, states temporal non-reproducibility of a viscous flow. The most often encountered property, necessary for the occurance of turbulence is a sufficiently large Reynolds number (V) $Re \gg 1$. The presence of a rigid surface (VI), and consequently it's no-slip condition leading to high shear rates, is the last prerequisite. [31]

Adimensionalisation of momentum equation (see e.g. [34]) yields dimensionless conservation of momentum[2] and Reynolds number Re ($\nu = \mu/\rho$):

$$\frac{\partial \mathbf{u}}{\partial t} + \mathbf{u} \cdot \nabla \mathbf{u} = -\nabla p + \frac{1}{Re} \nabla^2 \mathbf{u} \,, \qquad Re = \frac{UL}{\nu} \tag{3.7}$$

Rigorous description of turbulent flow is difficult since it is accompanied by an abundance of different time and length scales. More precisely, it is due to the non-linear (quadratic in $\mathbf{u}$) term on the LHS (Left-hand side) of momentum equation and the associated dynamics of smaller scales, resulting from subtle interplay with non-vanishing (contrasting Euler-limit: $Re \to \infty$) viscous term at the RHS (Right-hand side). Numerical simulation resolving scales all the way down to the smallest scales of turbulence (Kolmogorov scales) is known as DNS (Direct numerical simulation). Extremely fine temporal and spatial discretisation is required, hence fluid flow through most simple geometries could have been accomplished as of yet. [31]

In order to remedy just narrated difficulty, scientists have resorted to statistical methods. Instead of discussing several averaging methods pertinent in turbulence model research, the basic idea behind each method is explained by means the following experiment. Formulation of time-, spatial- and ensemble- averaging proposed by Reynolds, as well as the idea behind Favre averaging (density-weighted) for compressible flow considerations, is given for example in [29].

Figure 3.2 sketches the turbulent wake behind an initially stationary cylinder

[2] $\nabla \cdot (\mathbf{uu}) = \mathbf{u} \cdot \nabla \mathbf{u} + \mathbf{u} \cancel{\nabla \cdot \mathbf{u}} = \mathbf{u} \cdot \nabla \mathbf{u}$

Die approbierte gedruckte Originalversion dieser Diplomarbeit ist an der TU Wien Bibliothek verfügbar
The approved original version of this thesis is available in print at TU Wien Bibliothek.
TU Bibliothek Your knowledge hub WIEN

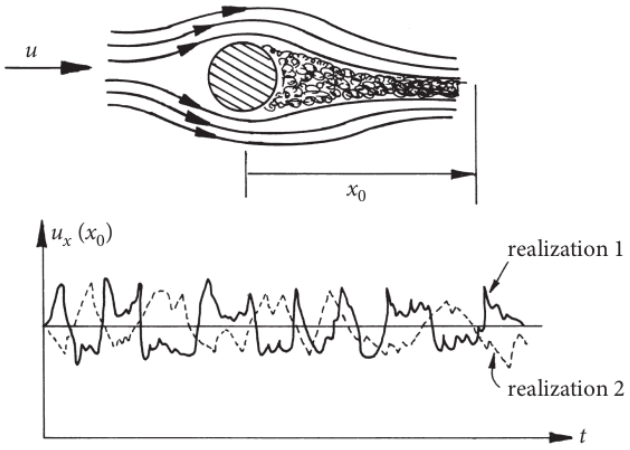

Figure 3.2: Realizations of an experiment [14]

towed through a quiescent fluid at constant speed. Despite identical inital conditions, the repetition of this experiment while measuring velocity u_x as a function of time at the fixed position x_0 each occasion, shows different realizations. In case of the depicted experiment, time-averaging each realization yields the exact same mean value (horizontal line along realizations). Each aformentioned statistical approach is concerned with expressing flow field quantities as the sum of it's mean and fluctuating part. E.g. the instantaneous velocity $\mathbf{u}(\mathbf{x}, t)$ is decomposed into the sum of mean velocity $\mathbf{U}(\mathbf{x})$ and it's fluctuating part $\mathbf{u}'(\mathbf{x}, t)$. Same procdure for the decomposition of p and $\mathbf{s}$, followed by averaging eq. (3.6) with some knowledge of correlations finally yields famous RANS equations:

$$\boxed{\begin{gathered}\nabla \cdot \mathbf{U} = 0 \\ \rho\frac{\partial \mathbf{U}}{\partial t} + \rho\nabla \cdot \left(\mathbf{U}\mathbf{U} + \overline{\mathbf{u}'\mathbf{u}'}\right) = -\nabla P + \nabla \cdot 2\mu\mathbf{S}\end{gathered}} \tag{3.8}$$

The fundamental problem of turbulence, also known as *Closure Problem*, lies within the prescription of the Reynolds-stress tensor $\boldsymbol{\sigma}^R = \rho\overline{\mathbf{u}'\mathbf{u}'}$ (reordering the above momentum equation yields more common notation of specific Reynolds-stress tensor $\boldsymbol{\tau}^R = -\overline{\mathbf{u}'\mathbf{u}'}$). Being symmetric, $\boldsymbol{\tau}^R$'s six independent unknown components on top of four unknown mean-flow properties $(P, \mathbf{U})$, yield a total of ten unknowns. With a grand total of four equations (one scalar, one vector equation), the system (3.8) remains undetermined. Tackling the circumstance of this undetermined system, i.e. finding approximations for unknown correlations in terms of known flow properties, can be understood as turbulence modeling. [33]

Die approbierte gedruckte Originalversion dieser Diplomarbeit ist an der TU Wien Bibliothek verfügbar
The approved original version of this thesis is available in print at TU Wien Bibliothek.

In quest of sufficient equations, the concept of the Reynolds-stress equation is inevitable. Not only does it represent it's own class of tubulence models (2nd-Order) their derivation (taking moments of NS equation ($\overline{u_i'\mathcal{N}(u_j) + u_j'\mathcal{N}(u_i)} = 0$[3]), showcases important turbulence quantities. As seen in [33], this derivation illustrates the closure problem of turbluence (by gaining six new equations, 22 new unknown correlations are generated). Trace operation of the Reynolds-stress equation (i.e. $tr\left(\overline{u_i'\mathcal{N}(u_j) + u_j'\mathcal{N}(u_i)} = 0\right)$) yields the important k-equation, here expressed in terms of physical processes:

$$\rho\frac{\partial k}{\partial t} + \rho\mathbf{U}\cdot\nabla k = P - \epsilon + D^{\mu} + D^{P} + \text{"}t.t.\text{"} \tag{3.9}$$

LHS reads as a momentum equation i.e. temporal/unsteady term followed by convective transport of property k. Further description of the terms on the LHS (P.. production, ϵ.. dissipation, D^{μ}.. viscous diffusion, D^{P}.. pressure diffusion and $t.t.$... turbulent transport) as well as the exact term-by-term eq. (3.9) is given in [33].

Explaination of the two most important turbulence quantities (k and ϵ) is most apparent in Lewis Fry Richardson's (1881-1953) energy cascade and his notorious little poem (fig. 3.3). As already stated, turbulence contains an abundance of different time and length scales. With the convention to talk of mechanical energy transferring, different-sized and -shaped structures as *eddies*, Richardson's energy cascade - present in all turbulent flows - describes a multi-stage

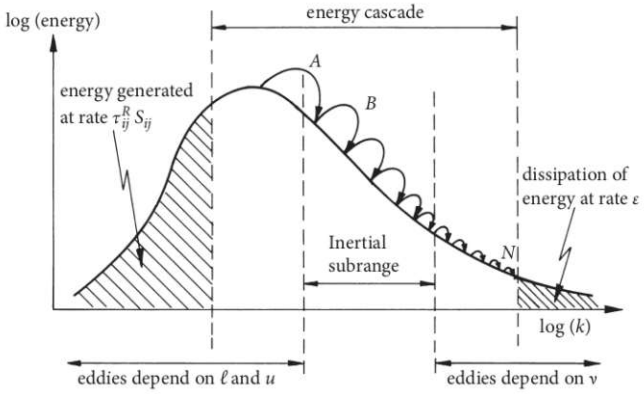

"Big whorls have little whorls,
Which feed on their velocity,
And little whorls have lesser whorls,
And so on to viscosity."

Figure 3.3: Schematic representation of the energy cascade [14]

[3]Navier-Stokes operator, invoking Einstein summation convention (Einstein notation) instead of tensor notation, defined as: $\mathcal{N}(u_i) = \rho\frac{\partial u_i}{\partial t} + \rho u_k\frac{\partial u_i}{\partial x_k} + \frac{\partial p}{\partial x_i} - \mu\frac{\partial^2 u_i}{\partial x_k \partial x_k} = 0$

Die approbierte gedruckte Originalversion dieser Diplomarbeit ist an der TU Wien Bibliothek verfügbar
The approved original version of this thesis is available in print at TU Wien Bibliothek.

process of large-scale eddies which transfer **turbulence kinetic energy** k (not to be confused with wavenumber k in figure 3.3) all the way down to the smallest-scale vorticies. Turbulence kinetic energy carried by the smallest-scale eddies has to be dissipated to heat through the action of viscosity. It is quantified in terms of the normal specific Reynolds-stress components and represents a measure for the intensity of turbulent fluctuations:

$$k \equiv \frac{1}{2}(\overline{u_x'^2} + \overline{u_y'^2} + \overline{u_z'^2}) = \frac{1}{2}\overline{\mathbf{u}'\mathbf{u}'} \tag{3.10}$$

Andrei Nikolaevich Kolmogorov's (1903-1987) *"K41"* universal equilibrium theory (1941) introduced the **dissipation rate** as $\epsilon = -\frac{dk}{dt}$. The rate of smaller eddies receiving energy from larger ones is somewhat equal to the rate at which the smallest eddies dissipate energy into heat. As previously stated, dissipation into heat happens through action of viscosity making ϵ and kinematic viscosity ν the sole influencing dimensional quantities of motion at the smallest scale. Simple dimensional analysis yields the Kolmogorov scales of length l_{K41}, time t_{K41} and velocity u_{K41} representing the smallest scales of turbulence: [14, 33]

$$l_{K41} \equiv \left(\frac{\nu^3}{\epsilon}\right)^{\frac{1}{4}}, \qquad t_{K41} \equiv \left(\frac{\nu}{\epsilon}\right)^{\frac{1}{2}}, \qquad u_{K41} \equiv (\nu\epsilon)^{\frac{1}{4}} \tag{3.11}$$

Still in need of closure, the first attempt in a mathematical describtion of said turbulent stresses was introduced by Joseph Valentin Boussinesq (1842-1929) in 1877 (prior to RANS's origin in 1895). His famous concept approximates the Reynolds-stress tensor by embracing a so-called *eddy-viscosity*. This titles the whole class of 1st-Order turbulence models as EVM (Eddy-viscosity models).

$$\boldsymbol{\tau}^R = 2\nu_t\mathbf{S} - \frac{2k}{3}\mathbf{I} \tag{3.12}$$

This newly introduced unknown eddy-viscosity ($\nu_t = \mu_t/\rho$) enabled modeling of k-equation which is used in virtually all turbulence energy equation models:

$$\frac{\partial k}{\partial t} + \mathbf{U}\cdot\nabla k = \boldsymbol{\tau}^R : \boldsymbol{S} - \epsilon + \nabla\cdot\left[(\nu + \frac{\nu_t}{\sigma_k})\nabla k\right] \tag{3.13}$$

However, an additional equation expressing ν_t (or other turbulence quantities commonly referred to as the turbulent length- or time- scale) is necessary to finally close the system of equations which culminates in 1st-Order two-equation models.

Die approbierte gedruckte Originalversion dieser Diplomarbeit ist an der TU Wien Bibliothek verfügbar
The approved original version of this thesis is available in print at TU Wien Bibliothek.
TU Bibliothek Your knowledge hub WIEN

3.2.1 Classification of Turbulence Model

Among the many turbulence models that already exist, five principle classes can be distinguished (fig. 3.4). Not only the level of complexity, but also computational effort decrease from top to bottom. The idea behind LES (Large-eddy simulation) models, found in between aformentioned DNS and RANS approach, resorts to the observation of small scale turbulent structure's universal character. Large energy carrying eddies are computed and instead of numerically resolving, the effects of small scale sturctures (homogeneous, isotropic turbulence i.e. statistically uniform in all directions) are modeled. Although they are computationally considerably cheaper compared to DNS, LES still require such a high grid resolution for engineering problems of large Re number, a solution consequencing massive computational costs cannot be adopted. Notwithstanding the fact that modeling all scales of turbulence is a brutal simplification and loses much of the information contained in the NS equation, Francis runner CFD falls back to the RANS turbulence model approach. [33, 35]

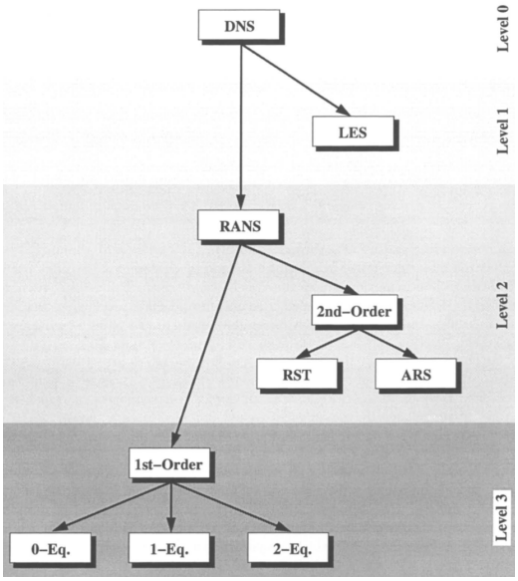

Figure 3.4: Hierachy of turbulence models [35]

Befor proceeding, the difference between 1st- and 2nd-Order RANS turbulence models needs to be summarized briefly. The description of the Reynolds-stress tensor invoking Boussinesq approximation (3.12) was found to have certain drawbacks. In assuming an analogy to Newton's law of viscosity (3.5), it must be emphasized that viscosity ν is a fluid property whereas eddy-viscosity ν_t depends upon many details of the flow under consideration. Flow-history effects and their persistence over long distances in a turbulent flow impose the most significant influence on $\boldsymbol{\tau}^R$, giving reason to doubt this simple linear relationship between $\boldsymbol{\tau}^R$ and $\mathbf{S}$. In addition, turbulence model's inability to take the effects of streamline curvature, secondary motions and sudden changes in strain rate into account, can be traced back to the eddy-viscosity approximation. To omit the introduction of additional differential equations, the idea of a nonlinear constitutive relation, to approximate

Die approbierte gedruckte Originalversion dieser Diplomarbeit ist an der TU Wien Bibliothek verfügbar
The approved original version of this thesis is available in print at TU Wien Bibliothek.

$\boldsymbol{\tau}^R$ more appropriately, was introduced. Turbulence models deducing this nonlinear relation for $\boldsymbol{\tau}^R$ form the full Reynolds-stress equation (hence 2nd-Order), followed by suitable closure approximations are termed ASM (Algebraic stress model, in fig 3.4: ARS.. Algebraic Reynolds-stress). The other type of 2nd-Order models neglect a constitutive relation and solve the equations (governed by the momentum of the NS equation) for each single Reynolds-stress tensor entry. Therefore they naturally take care of the aforementioned effects and Boussinesq approximation's shortcomings. They are termed RST (Reynolds-stress transport) models. [32, 33]

Despite RST (or RSM) model's convenient properties that automatically account for flow history, streamline curvature and independent treatment of $\boldsymbol{\tau}^R$'s normal stresses, the majority of simulated flows through Francis runners is performed using 1-st Order turbulence models. In the course of Francis-99 a total of two participants performed calculations on the basis of RSM. Mössinger et al.'s [36] results showed no significant advantage over RANS models for simulations at BEP operating condition. In fact, RSM simulations did not converge for part load operating condition, leading to Mössinger's favored overall turbulence model in terms of numerical robustness, stability and accuracy, namely the SST k-ω model. This two-equation model undeniably enjoys the most popularity in the field of Francis runnner CFD applications with it's origin in 1992. [37]

3.2.2 SST k-ω Model

Depending on the flow region, the SST k-ω model switches between the more appropriate turbulence model (k-ω and (transformed) k-ϵ model). Although proven success for a large variety of flow simulations, the k-ϵ model is notorious for it's lack of sensitivity to adverse pressure gradients which results in unnaturally high shear-stress levels and therefore delayed or even prevented flow seperation. The most prominent development to overcome k-ϵ's shortcomings with respect to accuracy and robustness on top of it's simple formulation hence advantageous numerical stability is the k-ω model. Somewhat ironic, it's origin dates back to the first two-equation turbulence model proposed by Kolmogorov in 1942. In the spirit of him being deemed as the great believer in dimensional analysis, he formed a transport equation for a second parameter, namely dissipation per unit turbulence kinetic energy ω. Reasoning behind his formulation resorts to simple

Die approbierte gedruckte Originalversion dieser Diplomarbeit ist an der TU Wien Bibliothek verfügbar
The approved original version of this thesis is available in print at TU Wien Bibliothek.
TU Bibliothek Your knowledge hub WIEN

dimensional analysis between ν_t [(length)^2/(time)], k [(length)^2/(time)^2] and ϵ [(length)^2/(time)^3]. Additional physical reasoning led to modeling of transport equation for ω [1/(time)]. The k-ω's drawback, however, is it's strong dependence on freestream values of ω, leading to unphysically large changes in magnitude of eddy-viscosity (see upcoming equation). [33, 37]

Full derivation of the SST model and it's fundamental BSL (Menter baseline) model is given in [37]. The essential supplementing definition for eddy-viscosity reads as:

$$\nu_t = \frac{k}{\omega} \tag{3.14}$$

In order to profit from the best of both, the BSL model switches between the k-ω model in near wall region (boundary-layer) and retains k-ϵ's advantage of the freestream independency in the wake region. Weighting the transport equations of each model seperatly (multiplication by blending function F_1 and $(1 - F_1)$), before correspondingly adding them together, reduces the four scalar equations to the BSL model's transport equations for k and ω. The same blending function accounts for the transformation of any constant ϕ from the k-ω (index 1) and the transformed k-ϵ (index 2) to the BSL model:

$$\phi = F_1\phi_1 + (1 - F_1)\phi_2 \tag{3.15}$$

With the introduction of a second blending function F_2, which is solely responsible for modification of the eddy-viscosity ν_t, the BSL model was advanced to the SST (Shear-stress transport) k-ω model. Rational behind the "2nd switch" is based on the assumption that the turbulent shear-stress in a boundary-layer is proportional to turbulence kinetic energy k. For conventional two-equation models, this proportionality can be rewritten in terms of production and dissipation ratio of turbulence kinetic energy. Overprediction of shear-stress for adverse pressure gradients (production/dissipation $\gg 1$) is avoided by means of second blending function, hence considered as a shear stress limiter.

Summing up, blending function F_1 takes the value one in the viscous sublayer and the logarithmic region of the boundary-layer (k-ω model) and gradually switch to zero in the wake region (transformed k-ϵ model). The aformentioned proportionality of shear-stress is implemented through modification of eddy-viscosity by means of blending function F_2. A value of one is realized for boundary-layer flow region

Die approbierte gedruckte Originalversion dieser Diplomarbeit ist an der TU Wien Bibliothek verfügbar
The approved original version of this thesis is available in print at TU Wien Bibliothek.
TU Bibliothek Your knowledge hub WIEN

prohibiting the overprediction of shear-stress (by decreasing ν_t) whereas a value of zero yields the original formulation (eq. 3.14) for the rest of the flow field. The price to pay for this advanced model is the necessary computation of blending functions, including their involved distance from the surface. [37, 38]

Despite the applied URANS (Unsteady RANS) approach (refrain from neglecting temporal terms) invoking the SST k-ω model (SST-URANS), discrepancies compared to measurements in Francis runner CFD simulations have been put in evidence, especially for the simulation of part load operating points. To avoid meshes, modeling the complete hydraulic machinery meeting LES requirements, hybrid RANS-LES models titeled SRS (Scale-resolving simulation) show improvements of results in part load operating condition. [39]

3.2.3 SST-SAS

Reason for the application of SRS models is not only related to superior accuracy, but first and foremost for their ability to resolve unsteady turbulent structures which RANS models are unable to obtain. The groundlaying idea of any SRS model is to harness RANS models strength in wall boundary-layer region and switch to a more appropriate formulation for free shear flows. As an example, DES (Detached-eddy simulation) models run in RANS mode for attached flow regions and switch to LES mode in detached regions away from the wall. This necessitates an LES grid (and time step) resolution in the majority of the computational domains (especially when considering Francis runner fluid flow), hence does not offer notable computational savings over standard LES. In addition, the LES' turbulent length scale, initiating the model switch, is strongly mesh dependent. As argued in [40], LES' future to become the main element in industrial CFD simulation of entire turbomachinery is considered unrealistic. The more recent approach, namely SAS (Scale-adaptive simulation), does not switch turbulence formulation but still enables the formation of a broadband turbulence spectrum. It is the applied turbulence modeling approach in the scope of this thesis that will be investigated further.

RANS models suffer from lack of an exact transport equation. On the basis of k-equation (eq. 3.13), representing the large scale of turbulence energy, this

Die approbierte gedruckte Originalversion dieser Diplomarbeit ist an der TU Wien Bibliothek verfügbar
The approved original version of this thesis is available in print at TU Wien Bibliothek.
TU Bibliothek Your knowledge hub WIEN

circumstance spreads on top of purely heuristic argumentation, to the second modeled transport equation. Deemed to account for closure, one reason for RANS' deficiencies lies in the observation that the transported turbulence quantities of the second transport equation (for example ϵ or ω), relate to the dissipative (smallest) scale of turbulence. Each transport equation defines an independent scale, one for large (k-eq.), the other for small scale turbulence (ω- or ϵ-eq.). In recent years, Rotta's approach from the early 1970s ([41]), which formulates a more consistent scaling equation that represents a large scale of turbulence for the second (closing) transport equation as well, has been modernized. These adaptions form a more solid base for the continuing term-by-term modeling approach. While derivation of Rotta's original k-kL model invoking the integral length scale L and it's transformation to the SST k-ω model is summarized in [42, 43], key is that the turbulent length scale L, estimated for standard two-equation models, will always approach turbulent shear layer thickness ($L \sim \delta$). Turbulence models based on Rotta's theory behave differently due to the inherent turbulent length scale of the second transport equation, not only allowing a more subtle reaction to resolved flow features but also determining both turbulent scales from model's source terms[4]. The turbulent length scale of Rotta's modeling approach estimates $L \sim L_{vK}$. [42]

While classical URANS methods show some improvement relative to steady state (RANS) simulations, they are bounded to unphysical single mode unsteady behaviour. This circumstance cannot be counteracted by either time step or mesh refinement. Adding the term Q_{SAS} to the SST's ω-equation, enables the model to operate in SAS mode. Q_{SAS} is zero for steady flow situation and the SST k-ω model is realized. Dependent on the ratio of integral length scale ($L \sim \sqrt{k}/\omega$) to the aformentioned von Kármán length scale ($L_{vK} \sim \kappa|\mathbf{U}'/\mathbf{U}''|$), source term Q_{SAS} dominates the other terms in the ω-equation and SAS mode is fully activated. An unsteady velocity profile yields a smaller von Kármán length scale, which is detected by Q_{SAS} and consequentially increases the production of ω. To summarize, L_{vK} adjusts to the smallest scales and in doing so increases ω which produces an eddy-viscosity (eq. 3.14) small enough to allow the formation of even smaller eddies until the grid limit is reached. [42]

[4]All other two-equation models determine one turbulence scale on the basis of source terms (strain-rate $\mathbf{S}$) while the second scale is not defined solely from source terms

Die approbierte gedruckte Originalversion dieser Diplomarbeit ist an der TU Wien Bibliothek verfügbar
The approved original version of this thesis is available in print at TU Wien Bibliothek.
TU Bibliothek Your knowledge hub WIEN

3.2.4 Law of the Wall

Participating in the course of Francis-99, Nicolle et al. [44], have already investigated the effect of near wall mesh refinement. In other terms speaking, they tried to evaluate the dependency of numerical solutions on the y^+-value. The results were that a completely different behaviour became evident for their two applied turbulence models (k-ϵ & SST k-ω). While simulations invoking the k-ϵ model were more or less insensitive when lowering the first cell height, the computed power output, for simulations with an SST k-ω model approach, decreased rapidly along with the wall distance and stabilzed for y^+-values < 5. This gives reason for a brief discussion on the pertinency of wall functions.

Boundary-layers are most demanding in terms of appropriate mesh resolution. High gradients, not only for primary solution variables (velocity, pressure) but even more so for turbulence quantities, are experienced in boundary-layers to meet the wall's no-slip condition. As stated in [45], the main quality criterion for boundary-layer meshes most CFD users are fixated on is not an achieved y^+-value sub predefined threshold, but rather the number of cells inside the boundary-layer. In addition, it is crucial that the Re-number dependent boundary-layer thickness δ (historically δ_{99}) is fully covered by so-called inflation or prism layers. To support following explaination, figure 3.5 depicts the classical case of a flow over a flat plate in two dimensions.

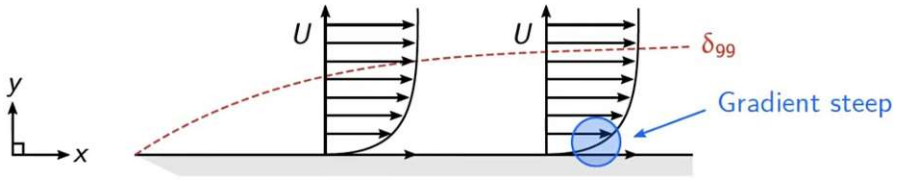

Figure 3.5: Flow over a flat plate, graphics adopted from [46]

Appropriate resolution of steep gradients in the direction normal to the wall ($\partial U/\partial y$) requires a certain cell height of the closest cell to the wall, inflation layer growth rate, typically in the range of $1.05 \div 1.3$ and enough inflation layers to include δ_{99} (see dashed red line in fig. 3.5). The smoothness of the last prism layer (farthest away from the wall) merging into the non boundary-layer mesh is another grid quality measurement. Small volume transitions are favorable.

The premise behind wall functions is to circumvent the aforementioned mesh

Die approbierte gedruckte Originalversion dieser Diplomarbeit ist an der TU Wien Bibliothek verfügbar
The approved original version of this thesis is available in print at TU Wien Bibliothek.

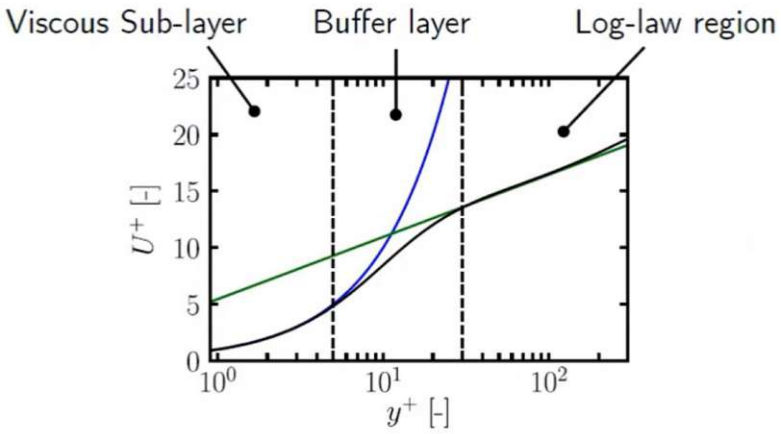

Figure 3.6: Law of the wall, graphics adopted from [48]

refinement when approaching the wall by means of empirically gathered functions which approximate the boundary-layer profiles. It's concept or rather the existence of boundary-layers is traced back to the findings of Ludwig Prandtl in 1904 [47]. Based on his theory it was shown that the near-wall region can be subdivided into two layers, i.e. the innermost so-called viscous sublayer followed by the logarithmic or log-law layer. The region inbetween is often considered as buffer layer (see fig. 3.6). As indicated by it's name, molecular viscosity plays the dominant role in the innermost sublayer (laminar-like flow) while turbulence dominates the mixing process further away from the wall. Viscous and turbulent effects are of compareable magnitude in the buffer layer. Wall functions employ empirical formulation on the basis of dimensionless near-wall mesh node distance y^+. Underlying mathematics accounting for the appropriate profiles of mean-flow as well as turbulence quantities in the near-wall region, can be looked up in most CFD toolboxes userguides (e.g. [49], [50]).

Modern CFD codes provide automatic near-wall treatment, i.e. the switch between wall-function and the so-called low-Re-number method. If boundary-layer resolution meets a y^+-value sub certain threshold, low-Re-number method (in this case the Reynolds number refers to turbulent Re-number which is of the order of $O(1)$ for the viscous sublayer) is applied. A more economic mesh in terms of numerical effort resorts to the wall-function method. From figure 3.6 it is clear that y^+-values in the buffer layer region ($5 < y^+ < 30$) inaccuratly predict the flow property (in this case tangential velocity along wall), and should be avoided. The implementation of inflation layers with a first cell height that yields $y^+ < 5$

Die approbierte gedruckte Originalversion dieser Diplomarbeit ist an der TU Wien Bibliothek verfügbar
The approved original version of this thesis is available in print at TU Wien Bibliothek.
TU Bibliothek Your knowledge hub WIEN

(which is recommended to be even lower $y^+ < 2$ by [50]), and therefore refrains from modeling the flow in it's laminar region, is however cumbersome and takes great effort in the meshing process.

3.3 Finite Volume Method

The already introduced governing equations in the previous chapter as well as transport equations of each turbulence model (current version in usage is provided in every CFD toolbox userguide), are PDE's. A solution to such typs of equations is acquired by using approximation methods. Most development of numerical approximating methods in the field of CFD is achieved for the finite volume method. As of today, every relevant software provider's toolbox (certainly mentioned ones) is based on the FVM. This is also the case for the used toolbox in the scope of this thesis namely Ansys CFX. Crudely speaking, FVM can be thought of as modeling the volume of interest, flow passes through, by means of a finite number of elements (tiny volumes) "in" which PDE's are solved. Flow field values governed by PDE's are calculated at predefined locations determined by certain nodes of each element. Following, a brief overview of groundlaying discretisation procedure and the naturally inhabitant discretisation error must be summarized.

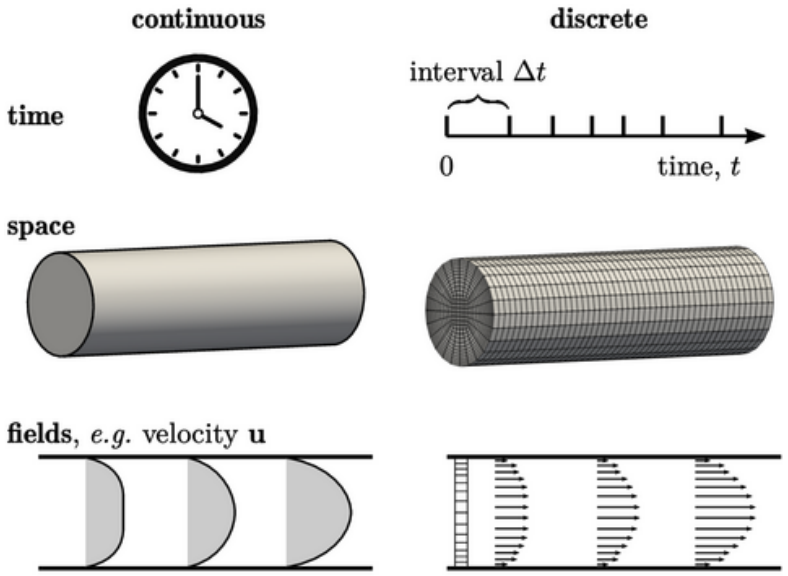

Figure 3.7: Solution domain discretisation for a pipe flow [30]

Die approbierte gedruckte Originalversion dieser Diplomarbeit ist an der TU Wien Bibliothek verfügbar
The approved original version of this thesis is available in print at TU Wien Bibliothek.

For better organisation of one's mind, there are two executed discretisation processes namely solution domain and equation discretisation. While the first is considered to numerically describe the computational domain dividing space into a finite number of discrete regions as well as splitting time into a finite number of time steps (transient simulation), the later copes with appropriate transformation of each term present in governing equations. In the sense of tangibility, solution domain discretisation is nicely illustrated in figure 3.7. [27]

A more profound description of solution **domain discretisation** i.e. the meshing process is provided in [51].

3.3.1 Equation Discretisation

It is the preceived wisdom of FVM's first introduction in the early 1970's. Indeed, the concept of a finite number of control volumes modeling the physical system of interest has its origin in 1967. Crediting the idea to his PhD supervisor, Brian Spalding, the original figure illustrating Spaldings's "tanks and tubes" was initially described in Runchal's PhD thesis (1969). Discrete grid points are surrounded by a single "tank" or control volume. "Tubes" or in modern terminology, fluxes, are referred to as each link between control volumes. In comparison to this ancient 2D-example (fig. 3.8), discrete points in a three dimensional domain (i.e. pipe flow in figure 3.7) are placed at each centre of every control volume or cell. Cells can have an irregular polyhedral shape consisting of an unlimited number of faces (≥ 4) and each face can have an

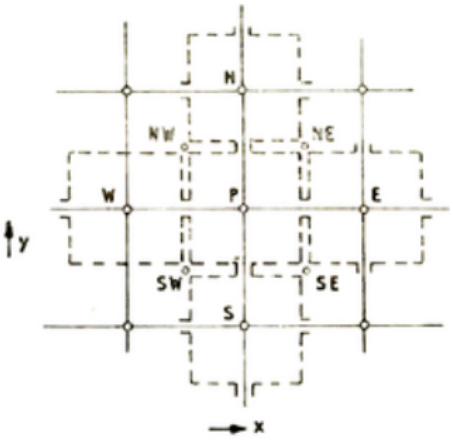

Figure 3.8: "tanks and tubes" [30]

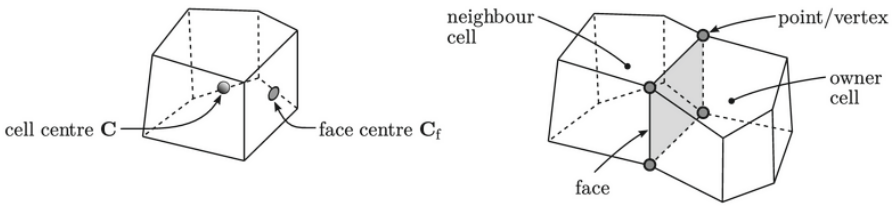

Figure 3.9: Cells in a FVM mesh [30]

Die approbierte gedruckte Originalversion dieser Diplomarbeit ist an der TU Wien Bibliothek verfügbar
The approved original version of this thesis is available in print at TU Wien Bibliothek.

unlimited number of edges (≥ 3). With the exception of the domains boundary, cells are contiguous in respect to their faces making each face common to two cells, one known as *owner* (P), the other one as *neighbour* (N) cell. In a *colocated* variable arrangement, all field quantities to solve for are stored at the cell centroid (P,N) of each control volume. [30]

Achieving good accuracy when dealing with 2nd-Order equations, the order of discretisation is required to be equal or higher than the order of the equation to be discretised. Proof of the FVM's discretisation being 2nd-Order accurate in time and space, requires field values to vary linearly across each control volume and is shown in Jasak's thesis [27].

To arrive at the corresponding system of simpler algebraic equations, the integral form of governing equations over each cell is discretised. Governing equation's integral form as well as several identities of the Gauss- or divergence theorem, relating volume integrals (e.g. $\int_V(\nabla \cdot \mathbf{a})\mathrm{d}V$) to it's flux through the volume's closed surfaces, are adressed in [27] as well. Assumption of linear variation across each single cell's bounding surfaces finally yields the expression for the summation of face integrals[5]:

$$\int_{V_P}(\nabla \cdot \mathbf{a})\mathrm{d}V \overset{Gauss}{=} \oint_{\partial V_P} \mathrm{d}\mathbf{S}.\mathbf{a} \longrightarrow \sum_f \left(\int_f \mathrm{d}\mathbf{S}.\mathbf{a}\right) = \sum_f \mathbf{S}.\mathbf{a_f} \tag{3.16}$$

Due to the necessity for face values as seen in eq. 3.16 at each face centre (fig. 3.9), discretisation schemes are often considered as face interpolation schemes. Face values are expressed (interpolated) in terms of cell centroid values of the owner (P) and neighbour (N) cell. Regardless of the applied face interpolation scheme, numerical errors naturally inhabit the discretisation procedure and cannot be avoided. While this first group of errors (equation discretisation error) is commonly considered as numerical diffusion, the other error (solution domain discretisation) comes down to insufficient mesh resolution, mesh skewness, and non-orthogonality. Put simply, they lack mesh quality. Numerical diffusion is a direct consequence of discretisation practice that is lower than 2nd-Order accurate. This drop in the order of discretisation is required to preserve boundedness of the solution.

[5] $\mathbf{a}$.. represents an arbitrary variable, $\mathbf{S}$.. outward-pointing face area vector and $\mathbf{a_f}$.. face centre value of $\mathbf{a}$

Die approbierte gedruckte Originalversion dieser Diplomarbeit ist an der TU Wien Bibliothek verfügbar
The approved original version of this thesis is available in print at TU Wien Bibliothek.
TU Bibliothek Your knowledge hub WIEN

Jasak [27] shows in great detail the numerical diffusion that can be related to the discretisation of the temporal and convective terms for several different schemes.

Only the basic concept of the FVM discretisation process up to this point shall be explained. Profound describtion of term-by-term discretisation using different schemes and the optional explicit versus implicit treatment of temporal terms is well documented in referenced literature. [27, 30, 29].

Discretisation process ultimately leads to matrix and source term construction. The system of algebraic equations in the end required to solve for, is conveniently described as a matrix equation. Figure 3.10 schematically displays the contribution of each term's discretised form to the matrix equation, shown for a transport equation of a random field value Ψ with a source term S_Ψ.

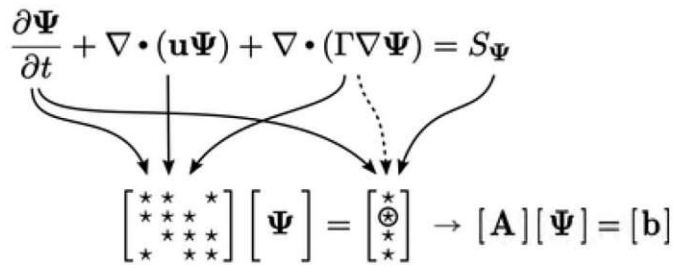

Figure 3.10: Examplary matrix construction [30]

At this point, the implementation of BC corresponds to adjustment of certain entries in the coefficient matrix [**A**] and source term [**b**].

3.3.2 Pressure-Velocity Coupling

Incompressible fluid flow's solution algorithm requires certain care. Since momentum equation (3.4,3.6) strongly couples both fields (p, $\mathbf{u}$) and the incompressible continuity equation ($\nabla \cdot \mathbf{u} = 0$) only imposes a restriction on the velocity field, the system of three equations solving for four unknows is undetermined. Difficulties associated with this pressure-velocity coupling accompanied by the discretisation of the pressure gradient led to a variety of segregated and coupled algorithms. The mother of segregated algorithms, SIMPLE (Semi-implicit method for pressure-linked equations), and it's improved spin-offs, initally solve the momentum equation in a sequential manner. Continuity equation's restriction is then "projected" onto

Die approbierte gedruckte Originalversion dieser Diplomarbeit ist an der TU Wien Bibliothek verfügbar
The approved original version of this thesis is available in print at TU Wien Bibliothek.
TU Bibliothek Your knowledge hub WIEN

the solution field in a seperate step. This "guess-and-correct" nature requires a large number of iterations. Coupled solvers, as the name states, solve both, the continuity and the momentum equation as a single, hence much larger system. A detail analysis between the two different approaches is given in [52].

Although a *staggered* variable arrangement (velocity evaluated at cell-face centres, other variables stored at the cell centre) not only proved efficient and accurate but also avoided prominent *chequerboard* oscillations, this method was bounded to structured meshes. Eagerness to solve fluid flow for complex geometries (unstructured meshes) has led to development for colocated arrangements. The most notable contribution enabling robust computation of meshes, storing all variables at the the same node, is credited to Rhie and Chow (early 1980s). It's numerical framework is very well documented by Bartholomew et al. [53].

The CFX toolbox uses a coupled solver algorithm based on the Rhie and Chow derivations. This allows for a fully implicit discretisation of each equation at any given time step. Solving implicitly discretised equations is generally more demanding in terms of computational effort yet proves superior in regards to numerical stability and the final number of iterations required until convergence. Due to the stronger coupling compared to the explicit approach, the system remains stable even if famous Courant-Friedrichs-Lewy (1967) limit is violated. Explicit system's stability is bounded to CFL number [34]:

$$CFL = \frac{U\Delta t}{\Delta x} < 1 \tag{3.17}$$

sub unity. Physical velocity U cannot propagate a distance exceeding Δx in time equal to Δt. For conducted SRS, CFX' solver theory guide, however, recommends meeting the condition $CFL = 1$ in the main SRS region for the accurate simulation of the physical process. [50]

3.3.3 Residual

Because of the governing equation's non-linearity, the system of algebraic equations is required to be linearized and solved iterativly. Only the general concept of this procedure is briefly explained. A profound overview of iterative solvers is given in [54].

Die approbierte gedruckte Originalversion dieser Diplomarbeit ist an der TU Wien Bibliothek verfügbar
The approved original version of this thesis is available in print at TU Wien Bibliothek.

For the remainder of this chapter the matrix notation $[\mathbf{A}][\mathbf{\Psi}] = [\mathbf{b}]$ (fig. 3.10) is replaced by $\mathbf{A} \cdot \mathbf{\Psi} = \mathbf{b}$, equivalent to vector notation. Coefficient matrix $\mathbf{A}$ is an $N \times N$ tensor. Solution vector $\mathbf{\Psi}$ is a single column vector with N rows. Linear iteration schemes resort to matrix decomposition ($\mathbf{A} = \mathbf{M} - \mathbf{N}$). The applied decomposition technique mainly influences the convergence speed and is not further considered. Showcasing the concept of a *residual* is of more importance, hence carried out. The absolute solution error is defined as the difference between the exact and approximate solution ($\boldsymbol{\epsilon}^{(n)} = \mathbf{\Psi_{ex}} - \mathbf{\Psi}^{(n)}$). Since the exact solution is unknown, $\boldsymbol{\epsilon}^{(n)}$ cannot be determined. The residual provides a measure for the error of the solution rather than the absolute error. After n-iterations the residual is expressed as:

$$\boldsymbol{\rho}^{(n)} = \underbrace{\mathbf{A} \cdot \mathbf{\Psi_{ex}}}_{\mathbf{b}} - \mathbf{A} \cdot \mathbf{\Psi}^{(n)} = \mathbf{b} - \mathbf{A} \cdot \mathbf{\Psi}^{(n)} \tag{3.18}$$

Prevailing linear relation between absolut solution error and residual is displayed by subtracting eq. (3.18) from the exact system of algebraic equations:

$$\begin{aligned} &\mathbf{A} \cdot \mathbf{\Psi^{ex}} - \mathbf{b} - \left(\boldsymbol{\rho}^{(n)} + \mathbf{A} \cdot \mathbf{\Psi}^{(n)} - \mathbf{b}\right) = 0 \\ &\longrightarrow \mathbf{A} \cdot \left(\mathbf{\Psi^{ex}} - \mathbf{\Psi}^{(n)}\right) = \underline{\mathbf{A} \cdot \boldsymbol{\epsilon}^{(n)} = \boldsymbol{\rho}^{(n)}} \end{aligned} \tag{3.19}$$

Qualitative convergence is indicated by a decrease of the residual by three orders of magnitude during the iteration process. Primary field variables are considered to be sufficiently established. In case of turbulence field variables, a decrease to a convergence tolerance of at least 10^{-6} is recommended. [55]

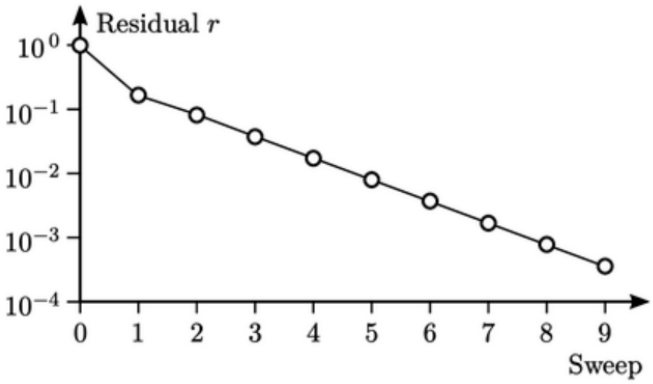

Figure 3.11: Typical residual control graph [30]

Figure 3.11 schematically displays the convergence history for an arbitrary field value.

Die approbierte gedruckte Originalversion dieser Diplomarbeit ist an der TU Wien Bibliothek verfügbar
The approved original version of this thesis is available in print at TU Wien Bibliothek.

Die approbierte gedruckte Originalversion dieser Diplomarbeit ist an der TU Wien Bibliothek verfügbar
The approved original version of this thesis is available in print at TU Wien Bibliothek.

Chapter 4

Prototype and Numerical Setup

Main characteristics of the prototype Francis turbine under investigation, already subject to several studies by predecessors (Unterluggauer [4, 56, 57, 58, 59], Schmelz [5] and Stadler [60]) shall be briefly recapitulated. Summarized numerical setups of performed simulations in the scope of this thesis are presented in the second section.

4.1 Prototype Francis Turbine

The hydropower plant under investigation is schematically depicted in figure 4.1. Intensive site measurements have been performed by Unterluggauer et al. [56], not only to gain insight on the experienced stress levels the runner is suffering under different operating conditions, but also to provide a solid basis for the validation of

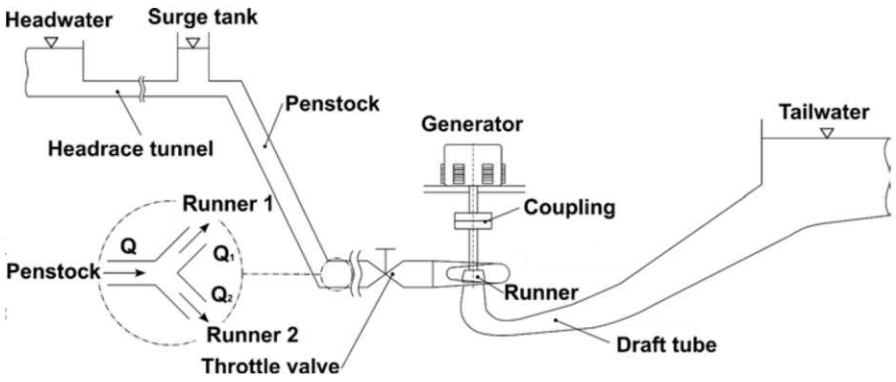

Figure 4.1: Hydropower plant [56]

numerical simulations. Only one of the two identical Francis runners was prepared for the conducted measuring programm while the other runner was maintained at stationary condition near the rated point (RP). Profound description of the measuring programm as well as sensor positioning is provided in Mühlbachler's thesis [61].

With a net water head of 160m, the turbine is considered a medium-head Francis runner defined by specific speeds of $n_q \approx 56$rpm at the RP. The runners main geometrical property is given in table 4.1. Dependent on the operating point, discharge varies from $\approx 5\text{m}^3/\text{s}$ to $37\text{m}^3/\text{s}$.

Runner diameter $D_{1,a}$ [m]	2
Number of stay vanes z_{SV} [-]	23
Number of guide vanes z_{GV} [-]	24
Number of runner blades z_{RB} [-]	13

Table 4.1: Runner facts

4.2 Numerical Setup

4.2.1 Spacial Discretisation

While numerous simulations have been performed by predecessors, gathering of available meshes and their comparsion was the initial task. The full scale computa-

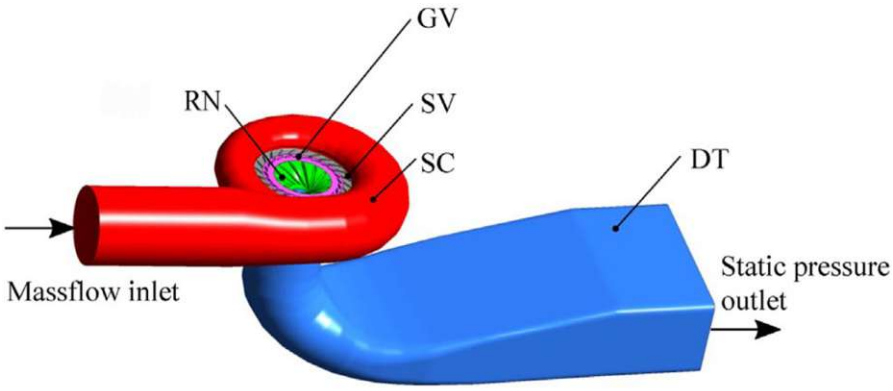

Figure 4.2: Computational domain [59]

Die approbierte gedruckte Originalversion dieser Diplomarbeit ist an der TU Wien Bibliothek verfügbar
The approved original version of this thesis is available in print at TU Wien Bibliothek.
TU Bibliothek Your knowledge hub WIEN

tional domain (fig. 4.2) is decomposed into 5 subdomains, the SC (Spiral case), SV (Stay vane), GV (Guide vane), RN (Runner) and DT (Draft tube) domain, respectively. Each domain is meshed seperatly after they are glued together by means of CFX's interface connection option GGI (General grid interface). Monitoring planes (see fig. 2.4) as well as monitoring points, according to sensor positioning in the conducted measuring programm, have been included in the numerical setup.

Since an investigation of a single operating point in part-load region was conducted, only one GV-mesh, corresponding to the guide vane opening (see fig. 2.5) of certain operating point is available. The turbines power output at this part-load operating point is estimated at around $37\% \cdot P_{RP}$.

Each particular domain was (with the expception of the runner: NUMECA AUTOGRID5 [57]) meshed using the current version of ANSYS ICEM. Multiblock, sole hexahedral elemental grids were realized. At this point, after simulations were finished, the editor focused on the meshing procedure for another prototype Francis turbine.

Domain	Cells [mio.]	Min. angle [°]	Min. determinant [-]	Min. aspect ratio [-]	Min. skew [-]
SC_coarse	1.620	6.181	0.175	0.261e-3	0.0653
SC_medium	1.698	7.137	0.199	0.214e-3	0.0472
SC_fine	3.693	6.254	0.081[1]	0.399e-3	0.0595
SV_coarse	0.400	24.822	0.212	0.414e-3	0.299
SV_medium	1.231	24.808	0.237	0.672e-3	0.290
SV_fine	4.080	24.821	0.282	1.008e-2	0.277
GV	2.597	30.144	0.626	0.663e-3	0.336
RN_coarse	3.143	15.855	0.169	0.252e-3	0.226
RN_medium	4.641	15.383	0.168	0.486e-3	0.229
RN_fine	7.284	18.228	0.251	0.682e-3	0.232
DT_coarse	0.986	31.356	0.429	0.375e-3	0.432
DT_medium	1.401	31.264	0.612	0.462e-3	0.395
DT_fine	3.069	30.379	0.607	0.606e-3	0.392

[1] 94 elements <0.2

Table 4.2: Single domain cell count and quality metrics

In order to perform a conclusive GIS, Celik et al. [62] suggest a grid refinement factor of $r > 1.3$. The procedure will be elaborated in more detail, but for now it is only required to state, that the refinement factor necessitates specific different cell counts of performed simulations. With an increasing cell count, meshes are notoriously titled "coarse - medium - fine". Due to a total of three available meshes

Die approbierte gedruckte Originalversion dieser Diplomarbeit ist an der TU Wien Bibliothek verfügbar
The approved original version of this thesis is available in print at TU Wien Bibliothek.
TU Bibliothek Your knowledge hub WIEN

for the SC- and SV-domain (already generated to conduct a GIS) and the necessary single GV-domain mesh corresponding to the appropriate opening, adaption of different meshes for the GIS in part-load operating condition was limited to the exchange of meshes only for the RN- and DT-domain. A total of seven different runner and eleven draft tube meshes were optional. Narrowed down and with computational effort as well as suggested refinement factor in mind, table 4.2 grants an overview of utilised mesh sizes and their quality metrics.

Following the study of Unterluggauer [57], same three global parameters, namely head H, mechanical power P_m and hydraulic efficiency η_h, are chosen to be evaluated in the course of conducted grid convergence study. Although grid refinement is recommended to be done systematically, it is appropriate to use an averaged "global" cell size when observing global variables. Achieving the desired refinement factor for a three dimensional domai0,n which tracks global variables, corresponds to a cell count factor c_r of:

$$c_r = \frac{\text{Ncells\_fine}}{\text{Ncells\_medium}} \left(= \frac{\text{Ncells\_medium}}{\text{Ncells\_coarse}} \right) = 1.3^3 \sim 2.2 \tag{4.1}$$

When comparing each domains cell counts seperatly (coarse - medium - fine) in table 4.2 to the outcome of equation (4.1), not only unsystematic mesh refinements but also seldom achieved cell count factors will become evident. This corresponds to a refinement factor sub suggested threshold of 1.3 as seen in table 4.3.

Refinement factor r [-]	Total mesh	Cells [mio.]
$r_{32} = 1.1341$	Coarse - 3	8.746
	Medium - 2	11.568
$r_{21} = 1.2641$		
	Fine - 1	20.723

Table 4.3: Refinement factor and total domain cell count

The procedure of a GIS according to Celik et al. [62], is the specific guideline for the calculation and the reporting of discretisation error estimates in a CFD simulation. To the authors knowledge, conducted GIS' in the field of Francis runner CFD. have been evaluated for stationary simulations, around BEP operating condition, only. Given this fact alone, as well as the pronounced inhomogeneous velocity profiles, and the awarness of complex flow phenomena occuring at off design conditions,

Die approbierte gedruckte Originalversion dieser Diplomarbeit ist an der TU Wien Bibliothek verfügbar
The approved original version of this thesis is available in print at TU Wien Bibliothek.
TU Bibliothek Your knowledge hub WIEN

supported the decision towards a conducted mesh scaling test in part-load operating region.

4.2.2 Temporal Discretisation

Influence of temporal parameters is another topic considered in the scope of this thesis. The timestep size dt in a Francis runner CFD simulations, is most commonly expressed in terms time, the runner is required to rotate a certain amount of degrees. To allow for a comparison, predecessors contributions shall be briefly summarized in regards to total simulation duration as well as timestep size.

A total of 15 runner rotations with a timestep value corresponding to 1° of a single runner revolution have been performed by Unterlugauer et al. [57]. The same timestep size but less total runner rotations (8.5), due to larger total cell counts (25 mio. for RN domain, 37 mio. for RN VS domain, see [58]) were simulated in a follow up effort, investigating the impact of air admission in low-load operating conditions. The thesis of Schmelz [5] reports an approximate total of 30 runner rotations with a timestep size corresponding to 5° of a runner revolution. Finally, Stadler [60] simulated a total of seven runner rotations and a time step size of 1° without injection of air in the GV region.

Setup	Cells [mio.]	dt [°]	T_{sim} [rev.]	dt [s]
Steady [57]	5.991[1]	58.628	1000 iterations	2.228-2
Unsteady [57]	≈ 13	1	15	3.8889e-4
Unsteady [58][2]	25/37	1	8.5	3.8889e-4
Unsteady [5][2]	13.584	5	≈ 30	1.9445e-3
Unsteady [60]	≈ 6	1	7	3.9e-4

[1] no spiral case, one runner sector

[2] air admission

Table 4.4: Timestep size and simulation time summary

While aformentioned parameters relate to unsteady calculations, a steady state simulation with a physical timestep size of $1/\omega = 30/n\pi \longrightarrow 0.022282$s was conducted in order to acquire an initial solution, unsteady simulations utilize as input. The initial simulation is reported to omit the SC domain in it's spatial discretisation

Die approbierte gedruckte Originalversion dieser Diplomarbeit ist an der TU Wien Bibliothek verfügbar
The approved original version of this thesis is available in print at TU Wien Bibliothek.
TU Bibliothek Your knowledge hub WIEN

and uses a correspondig mass-flow distribution with an incident angle defined at SV inlet. Its influencial aspect on follow up simulations due to this truncated initial simulation for the sake of computational savings, might be questionable and a source of uncertainty. Table 4.4 summarizes predecessors conducted simulations.

The performed simulations in the scope of this thesis with respect to the applied temporal parameters are given in table 4.5. Three different time step sizes have been chosen to compare and evaluate it's influence on the numerical solution. Spacial discretisation in each case corresponds to the medium mesh (11.568 mio. cells) size.

Setup	Cells [mio.]	dt [°]	T_{sim} [rev.]	dt [s]
Unsteady	11.568	1	$\approx$ 70	3.8889e-4
Unsteady	11.568	0.5	$\approx$ 21	1.9444e-4
Unsteady	11.568	0.1	$\approx$ 21	3.8889e-5

Table 4.5: Current timestep size and simulation time

All simulations were performed on the fastest supercomputer in Austria, namely VSC-4 (Vienna Scientific Cluster). In case of the dt-timestep size, an approximate wall clock time of ∼2.5-3 days was required to simulate 7 full runner rotations. For 0.5dt, half the runner revolutions could be simulated in the same amount of days. This relation trivially extends to a tenth of the timestep size. In the end a total of 70 runner revolutions with a timestep size of dt, and 21 full rotations with 0.5dt as well as 0.1dt were simulated. Resulting total wall clock time can be estimated to ∼30 days for dt-calculations, ∼18 days for 0.5dt- and ∼90 days of 0.1dt-calculations.

4.2.3 Solver Settings

The analysis type for each simulation is set to transient and the applied turbulence model is the scale resolving SST-SAS model with automatic wall function treatment. CFX's "High Resolution" scheme is chosen for the discretisation of the advection terms. "Second Order Backward Euler" is selected for temporal terms. While treamtent of temporal terms is in agreement with the suggestion of "Best Practice: Scale-Resolving Simulations in Ansys CFD" ([40]), the advection term is

Die approbierte gedruckte Originalversion dieser Diplomarbeit ist an der TU Wien Bibliothek verfügbar
The approved original version of this thesis is available in print at TU Wien Bibliothek.

recommended to be treated by the BCD (bounded central differencing scheme). A qualitative comparsion between these two schemes might be interesting, although occuring differences are expected more in terms of required convergence time, rather than, if at all, in distinctive deviation between numerical solution values. The main difference between the two schemes is the evaluation of the specific blending factor which first and foremost influences the convergence rate.

Turbulence numerics is treated, as suggested in [40] by CFX's "First Order" scheme. Convergence criteria is set to a RMS (root mean square) value of $1e^{-8}$ and the maximum number of coefficient loops is set to eight. The applied boundary condition configuration is very well in agreement with the most robust configuration according to CFX 'solver modeling guide ([49]) i.e. velocity/massflow as inlet and static pressure as outlet condition. Turbulence intensity is estimated medium at the inlet and outlet boundaries. Each wall is considered to be smooth and the "No Slip Wall" condition is applied. As already stated, GGI connection is selected for each linkage of the interfaces between computational domains. Due to is rotating motion, the "Transient Rotor Stator" setting is selected at the runners inlet and outlet interface.

Die approbierte gedruckte Originalversion dieser Diplomarbeit ist an der TU Wien Bibliothek verfügbar
The approved original version of this thesis is available in print at TU Wien Bibliothek.

Chapter 5

Results

5.1 Turbulent Structures

Following the guideline of the "Best Practice: Scale-Resolving Simulations in Ansys CFD" ([40]), first topic on the agenda when post processing a finalized simulation, is the visual inspection of the turbulence structures. This makes sense from the standpoint, that the main reason for the application of an SRS model is, as aformentioned (see chapter 3.2.3), to obtain turbulent flow behaviour in greater detail. Common approaches, often encountered when visualizing turbulence are the λ_2- and the Q-criterion. The original definition of a vortex in an incompressible flow was proposed in terms of the eigenvalues of the tensor $\mathbf{S}^2 + \mathbf{\Omega}^2$ (see [63]). $\mathbf{\Omega}$[1] represents the skew- or anti-symmetric counterpart of already introduced strain-rate tensor $\mathbf{S}$ (averaged eq. 3.5). With the more general definition of Q according to [40]:

$$Q = C_Q(\mathbf{\Omega}^2 - \mathbf{S}^2) \tag{5.1}$$

an iso-surface, that corresponds to the selected value of the Q-criterion, can be visualized. Small values of Q are related to weak turbulent structures. The essential, large scale turbulence is obtained by large values of Q (for high Re-numer flows up to $Q \approx 10^8$). A value of zero calculates the iso-surface for a perfect balance between the deformation- and spin- tensor, whereas higher values shift the iso-surface to regions, where the rate of rotation (vorticity), is dominating the rate of deformation (shear).

[1] $\mathbf{\Omega} = \mathrm{skw}(\nabla\mathbf{U}) = \frac{1}{2}(\nabla\mathbf{U} - \nabla\mathbf{U}^t)$

Die approbierte gedruckte Originalversion dieser Diplomarbeit ist an der TU Wien Bibliothek verfügbar
The approved original version of this thesis is available in print at TU Wien Bibliothek.
TU Bibliothek Your knowledge hub WIEN

Most prominent occuring unsteady flow phenomenon in part-load operating region is the draft tube vortex rope (DTVR). Post-processing the Q-criterion of conducted simulations yields the iso-surface, which displays the DTVR's size and shape. In figure 5.1, the top view of the obtained DTVR for the simulation with a timestep size dt (left), is compared to the one which invokes the finest timestep size (0.1dt, right). The iso-surface is colored with the turbulent or eddy-viscosity ratio (TVR $= \mu_t/\mu$).

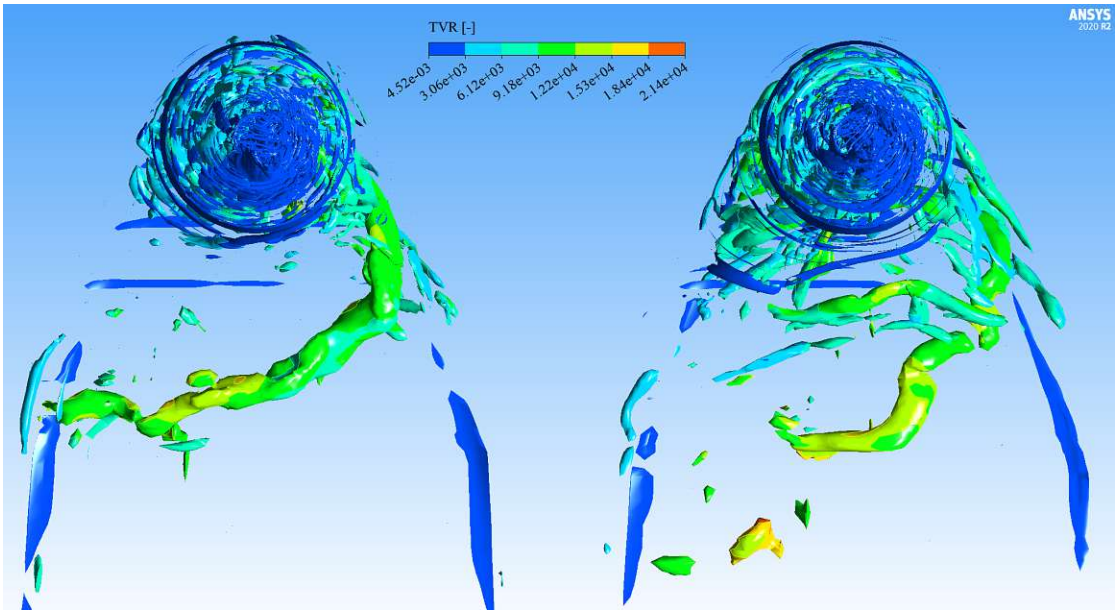

Figure 5.1: DTVR for different timestep sizes: left - dt, right - 0.1dt

It is recognized, that, in case of the 0.1dt simulation (right), the vortex rope extends much further downstream into the draft tube. The length between each final blob of vorticity (end of the DTVR) is approximately 1.5 meter.

The same change in behaviour of the DTVR, along refined simulations, is obtained for increasing cell counts (spatial refinement). Figure 5.2 compares the DTVR for different mesh sizes. Going from left to right, the mesh size increases from the most coarse mesh (left), to the one with the highest cell count (right). While the Q-criterion in case of the coarse and medium mesh, obtains more or less random blobs of vorticity close to the region of the suspected DTVR, the fine mesh not only shows an extended DTVR, but also a more compact shape of the large scale vorticity. That indicates the persistence of turbulent structures over a longer distance when refining spatial parameters. If the medium mesh (fig. 5.2 mid), is

Die approbierte gedruckte Originalversion dieser Diplomarbeit ist an der TU Wien Bibliothek verfügbar
The approved original version of this thesis is available in print at TU Wien Bibliothek.
TU Bibliothek Your knowledge hub WIEN

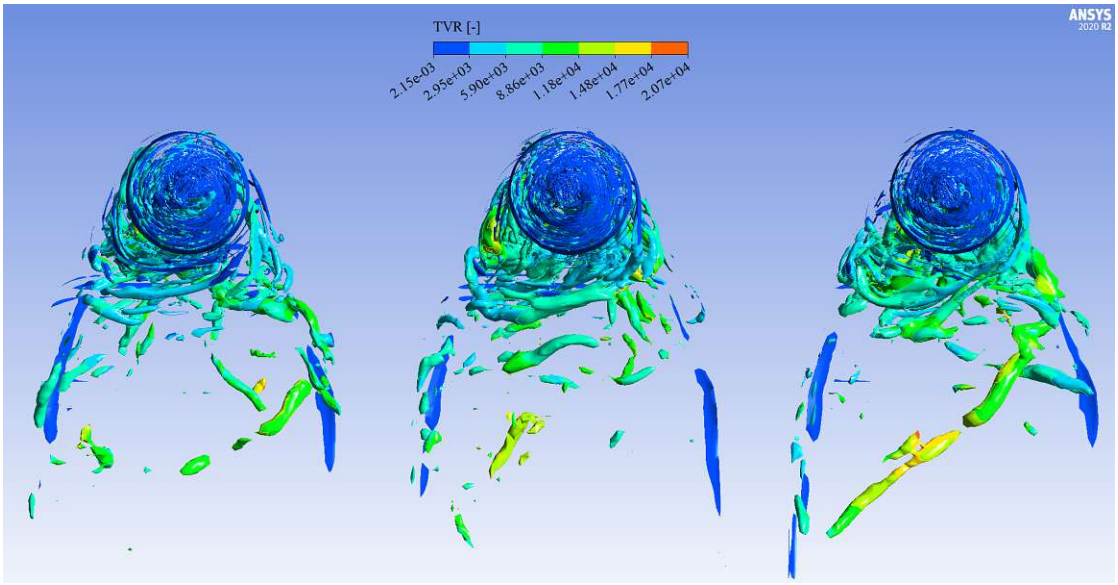

Figure 5.2: DTVR for different mesh sizes: left - coarse, mid - medium, right - fine

compared to the fine mesh DTVR (fig. 5.2 right), it is seen that the location of the impact point at the RHS of the draft tube wall[2], varies. The Q-criterion obtains an early impact of the medium mesh DTVR, with respect to the fine one. As a result of the impact at the right wall, the vortex rope changes it's direction and heads towards the left side (final blob fig. 5.2 mid). A delayed reflection of the DTVR is evident in case of the fine mesh.

One reason of this varying DTVR's size and shape, dependent on temporal and/or spatial parameters, can be related to the different prediction of the swirling magnitude at the interface section from runner to draft tube. More precisely, it is due to the circumferentially located swirling strength of the velocity vector around the draft tube nose. Comparison of the swirling vector between conducted simulations is displayed in figures 5.3 and 5.4. Again, computational effort increases from left to right in both figures.

The value of the swirling vector changes quite drastically and almost doubles it's magnitude between the dt and 0.1dt simulation (fig. 5.3). Same increase in magnitude is evident between the coarse and medium mesh, whereas it remains of

[2]The flow direction vector towards the draft tube outlet is the reference to determine right and left

Die approbierte gedruckte Originalversion dieser Diplomarbeit ist an der TU Wien Bibliothek verfügbar
The approved original version of this thesis is available in print at TU Wien Bibliothek.
TU Bibliothek Your knowledge hub WIEN

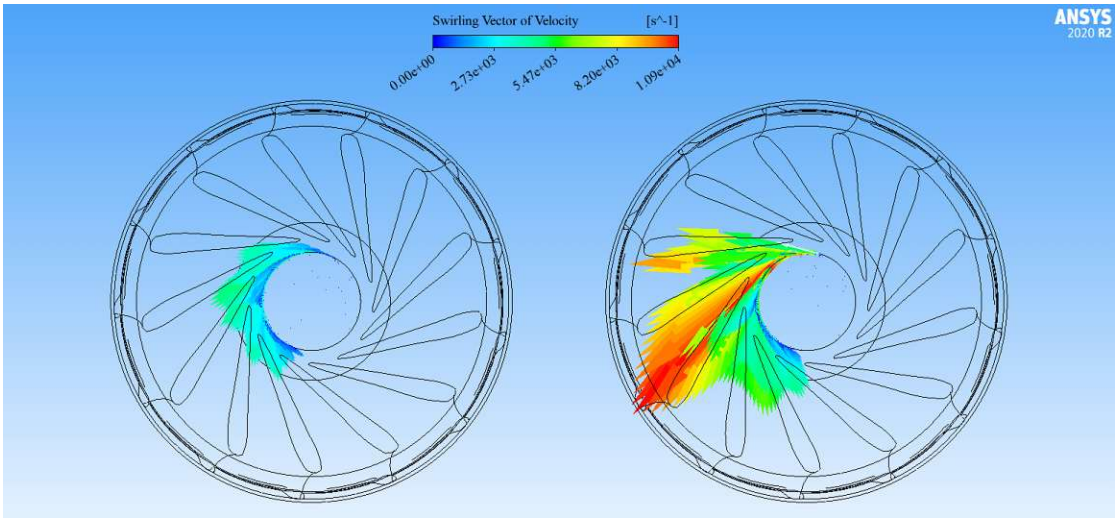

Figure 5.3: Swirling magnitude for different timestep sizes: left - dt, right - 0.1dt

the same order of magnitude for further refinement (fig. 5.4). The circumferential locations of displayed swirling vectors indicate the detachment of turbulent structures. While only the magnitude of swirl changes between refined timestep sizes (fig. 5.3), the detachment region, not only tends to increase from the coarse to the medium mesh, but even splits into two regions in case of the fine mesh (fig. 5.4).

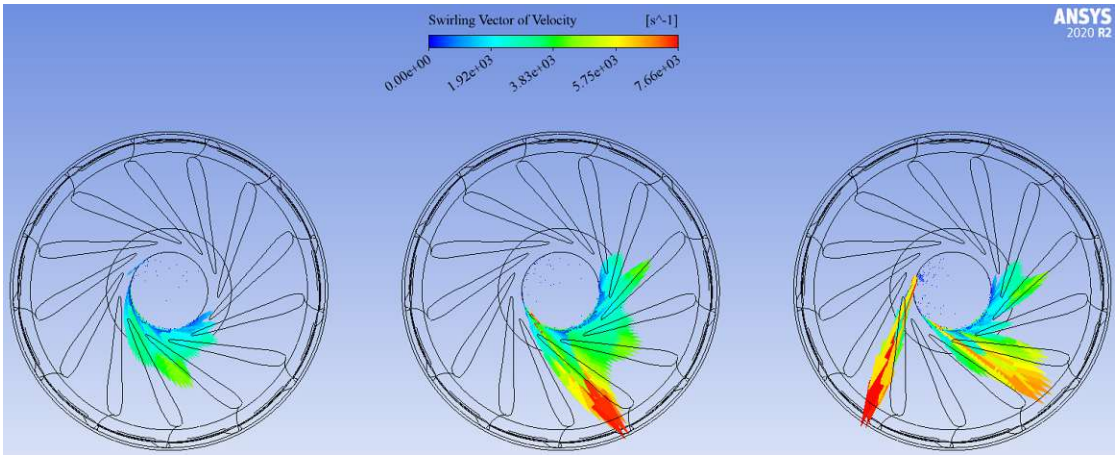

Figure 5.4: Swirling magnitude for different mesh sizes: left - coarse, mid - medium, right - fine

The reason for this split is probably an insufficient timestep size in the conducted simulation with the finest mesh. High local CFL number values in the region around the draft tube nose indicate and instable solution, and the predicted detachment region of turbulent structures, which are at the origin of the DTVR, must

Die approbierte gedruckte Originalversion dieser Diplomarbeit ist an der TU Wien Bibliothek verfügbar
The approved original version of this thesis is available in print at TU Wien Bibliothek.
TU Bibliothek Your knowledge hub WIEN

be considered with caution. Without a doubt, the interface where the rotating runner mesh meets the stationary draft tube mesh, forms one of the main sources of uncertainty in the conducted Francis runner CFD simulations.

It is readily seen, that an increase in computational effort, due to a refined timestep size or larger cell counts, leads to greater swirling magnitudes. This is the reason for the longer persistence of a vortex rope in refined simulations. The decay of turbulence starts at higher initial values, hence the breakdown from large to small, and smallest scale turbulence requires a greater amount of time.

5.2 Influence of Temporal Parameters

Aside the residual graph (compare fig. 3.11), that indicates convergence of field variables, the monitoring of global parameters is another tool that enables to estimate the validity of the numerical solution. Since each simulation, conducted in the scope of this thesis, is initiated with a converged solution that was achieved by a predecessor, the residual plots indicate qualitative convergence for all field values. However, the recommended decrease to a convergence tolerance of at least 10^{-6} in case of turbulence field quantities, is not achieved. The RMS (Root-mean square) value for turbulence kinetic energy and frequency (k and ω) varies between 10^{-4} and 10^{-5}. RMS values for the primary field variables have decreased by three orders of magnitude at least, and vary around 10^{-5} for every simulation. Following, the influence of simulation time, and different timestep sizes, on the monitored global parameters, is presented.

5.2.1 Simulation Time T_{sim}

The simualted duration T_{sim} is conveniently correlated to runner revolutions. To get rid of starting oscillations, the first five full runner rotations are not considered in the following evaluation. Due to considerabe long wall clock times, already mentioned in chapter 4.2.2, only the simulations which invoke the coarse timestep size (dt) are calculated for a total of ≈ 70 runner revolutions.

Figure 5.5 shows the behaviour of global variables η_h (top graph), H (middle

Die approbierte gedruckte Originalversion dieser Diplomarbeit ist an der TU Wien Bibliothek verfügbar
The approved original version of this thesis is available in print at TU Wien Bibliothek.

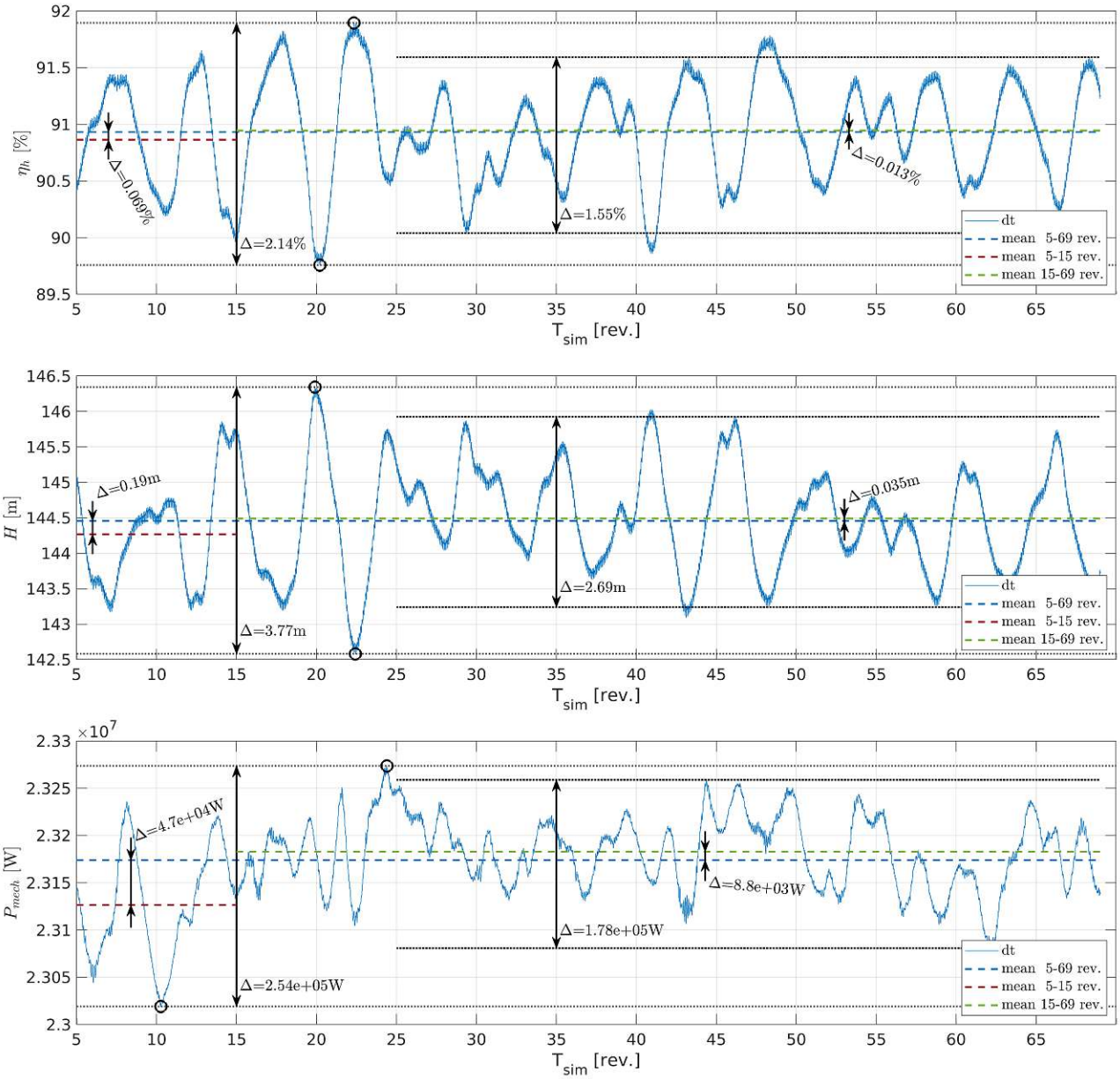

Figure 5.5: Monitored global parameters over T_{sim}

graph) and P_{mech} (bottom graph), that have been monitored during the simulation of the medium mesh size in solid blue. The blue dahsed line displays the mean value of each variable over the whole range of runner rotations (five to 69). In comparison, the red and green dashed lines showcase the mean values for the first ten, and the last 54 runner rotations respectively. It is readily seen, that the mean values of the first ten runner rotations, deviate by a larger magnitude, than the

Die approbierte gedruckte Originalversion dieser Diplomarbeit ist an der TU Wien Bibliothek verfügbar
The approved original version of this thesis is available in print at TU Wien Bibliothek.

mean values, evaluated for the last 54 rotations, with respect to each mean value over the whole runner rotation range (blue dashed line). This circumstance is most pronounced in case of the monitored mechanical power P_{mech}. In addition, it is recognized, that the value band from peak to valley (dotted black lines), reduces almost instantly for each global parameter at a threshold of 25 runner revolutions. If the highest peak and the lowest valley in the follow up rotations are not taken into account, the value band reduces it's range by 27.6% for the hydraulic efficiency, 28.6% for the head and 30% for the mechanical power. The narrowed variation band, persistent over 44 runner rotations, indicates more accurate solution values from 25 runner revolutions onwards. This outcome is in good agreement with the claim made by Krappel et al. [24]. In their research paper it is stated, that meaningful statistical data requires the neglection of the first 20 rotations of their totally simulated 80 runner revolutions.

However, a serious change in mean values is not obtained. Hydraulic efficiency increases by 0.082%, when comparing the mean value of the first ten, to the mean of the follow up 54 runner rotations. An increase is also evident for the mechanical power and the head. The change in head is close to a quarter of a meter and the mean mechanical power is predicted $\approx 5.6 \times 10^4$W higher. Percentage wise expression of these changes is superflous and far from the aformentioned, significant value band changes close to 30%.

This outcome allows for the argumentation, that the mean values of the monitored global parameters do not change significantly along a prolonged duration of the simulation time. They deviate by less than 0.2% if the first ten and follow up 54 runner rotations are compared. When considering the computational effort that leads to this outcome, the necessity for such long simulation times becomes questionable. However, due to the significant drop of the value band's range from 25 runner rotations onwards, the computational result after said threshold must definitely be considered as the more accurate solution.

5.2.2 Timestep Size dt

To quantify the influence of different timestep sizes, same monitored global parameters, as in the previous chapter, are compared against each other. Due to aformentioned computational effort, only 21 runner rotations, with a refined

Die approbierte gedruckte Originalversion dieser Diplomarbeit ist an der TU Wien Bibliothek verfügbar
The approved original version of this thesis is available in print at TU Wien Bibliothek.
TU Bibliothek Your knowledge hub WIEN

timestep size of 0.5dt and 0.1dt, have been simulated.

Figure 5.6 showcases the monitored data from two to 21 full runner rotations (solid lines) as well as each mean value, evaluated in the range from five to 21

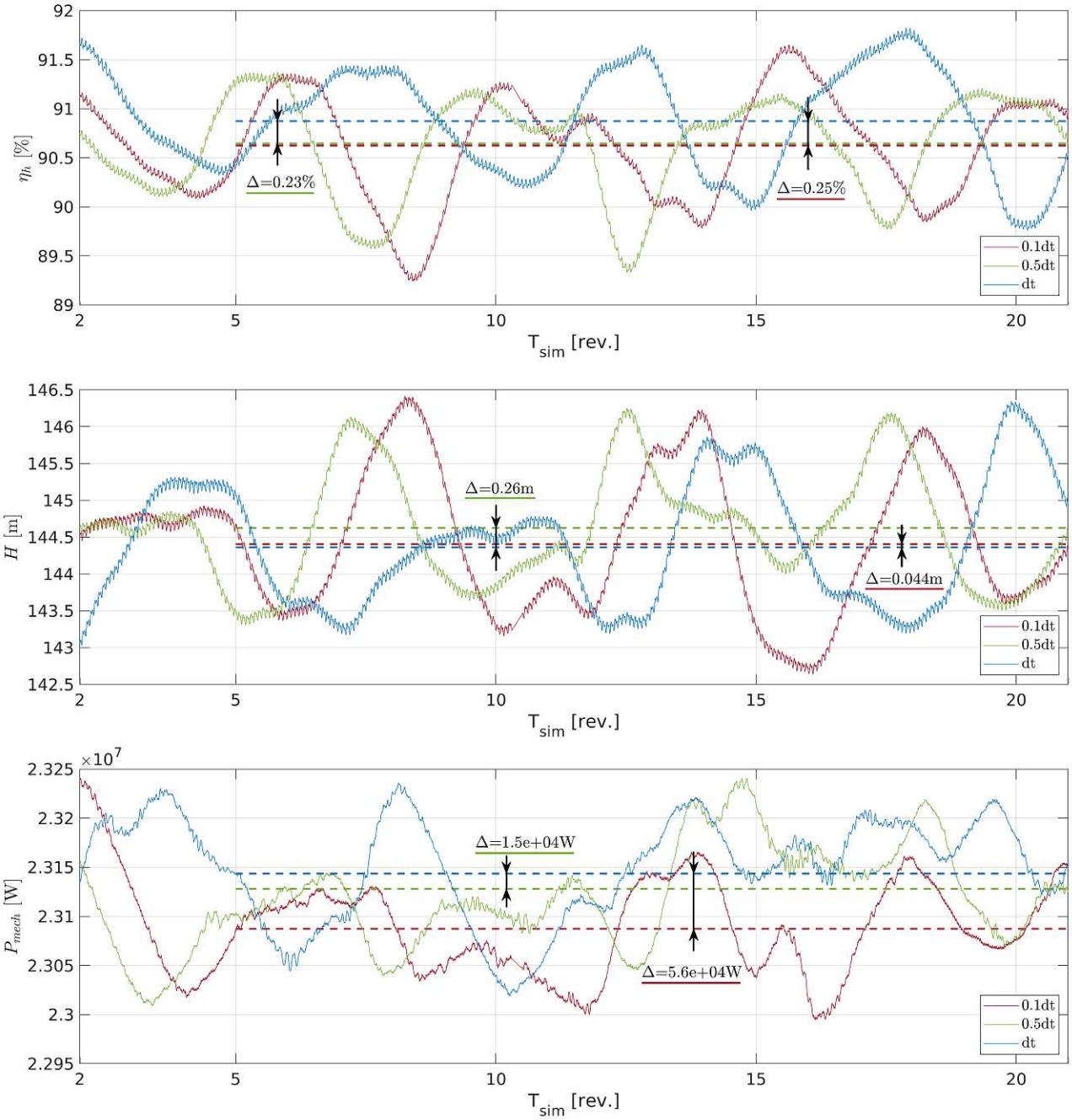

Figure 5.6: Monitored global variables for varying timestep sizes

Die approbierte gedruckte Originalversion dieser Diplomarbeit ist an der TU Wien Bibliothek verfügbar
The approved original version of this thesis is available in print at TU Wien Bibliothek.

runner rotations (dashed lines). Almost identical mean values are evident only in case of the hydraulic efficiency η_h (top graph), for both refined timestep sizes. The green dashed line (0.5dt) is almost in perfect alignment with the red dashed line (0.1dt). Their drop in hydraulic efficiency is $\approx 0.25\%$ with respect to the mean value of the coarse timestep size simulation (dt, blue dashed line).

Decreasing mean values are also obtained for the mechanical power (bottom graph). While the drop in mean power between the dt (blue dashed line) and the 0.5dt (green dashed line) simulation is $\approx 1.5 \times 10^4$W, this rate almost quadruples in case of the 0.1dt (red dashed line) results. The mean value of the mechanical power drops by $\approx 5.6 \times 10^4$W in case of the simulation which invokes the finest timestep size (0.1dt), when referenced to the mean of the coarse timestep size (dt).

Conversely, the monitored head H (middle graph) showcases an increase for the refined timestep sizes. When comparing the mean values of the 0.5dt simulation (green dashed line) to the coarse one (dt, blued dashed line) the head increases by ≈ 0.26m. Interestingly, a much smaller increase (by ≈ 0.05m) becomes evident, when comparing the coarse result to the one, which invokes the finest timestep size (0.1dt, red dashed line). This pattern is in contrast to the change towards lower mean values, which is true in case of the hydraulic efficiency and the mechanical power. A smaller timestep size yields smaller mean values of the power and efficiency, but slightly increases the head.

Both, longer simulation duration and spatial/temporal refinement translates to an increased computational effort. As showcased in the previous chapter, each mean value of the monitored global parameters, experiences a slight increase with a prolonged simulation duration. Hence, increased computational effort, as a result of more simulated runner revolutions, increases all monitored global parameters (see fig. 5.5, all graphs). Apart from the monitored head, the opposite is true when increasing the computational effort, due to a refined timestep size. Smaller timestep sizes lead to a decrease in hydraulic efficiency, as well as mechanical power (top and bottom graph in fig. 5.6), while the mean head value increases.

A reason why the monitored head breaks this pattern is unclear. More simulated runner revolutions with both refined timestep sizes are likely to reveal a corresponding pattern for the head as well. In addition, no significant value band

Die approbierte gedruckte Originalversion dieser Diplomarbeit ist an der TU Wien Bibliothek verfügbar
The approved original version of this thesis is available in print at TU Wien Bibliothek.
TU Bibliothek Your knowledge hub WIEN

drop can be identified for the refined timestep size simulations up to 21 runner rotations. Again, more simulated runner rotations with the two finer timesteps are likely to expose the same behaviour of such a value band drop, along prolonged simulation duration (see chapter 5.2.1). In general, a deviation of less than 0.27%, with respect to the mean value of the simulation which invokes the coarse timestep size dt, is evident for all global parameters. Comparing the monitored signal of the 0.5dt (green), to the 0.1dt (red) simulation, a similar but shifted behaviour, for all global parameters, is recognized. This circumstance again suggests, that the simulations with a refined timestep size represent the more accurate solution.

Figure 5.7 further substantiates the different DTVR behaviour (see fig. 5.1), for the refined timestep sizes. Both graphs display the monitored pressure signal at a location further downstream at the draft tube wall. The upper graph showcases the monitored pressure at the right side of the DT wall and the monitor point, that tracks the bottom signal, is located at the opposite, left side of the draft tube.

Again, a quite similar, but shifted behaviour when comparing the monitored signal for both temporally refined simulations (green, 0.5dt and red, 0.1dt), is evident. In case of the upper graph, which showcases the pressure signal at the right side of the draft tube, the mean values for the refined simulations are almost in perfect alignment. The large pressure fluctuations, evident in each monitored signal, clearly indicate the impact of the vortex rope at the draft tube wall. Although the pressure amplitudes are of comparable size, regardless of the timestep size, the vortex rope's impacts at the wall, are predicted at different instances. While the first and the second impact (at around six and 15 runner rotations respectively), are predicted at similar times for the refined timestep sizes, the prediction of first impact, in case of the dt simulation (blue), happens delayed at around 13 runner rotations. A second impact of the blue signal is not obtained, in the simulated duration of 21 runner rotations. This is another indication for a more accurate solution in favor of the refined timestep sizes. The occurance of the vortex rope is in better agreement between the refined simulations.

Die approbierte gedruckte Originalversion dieser Diplomarbeit ist an der TU Wien Bibliothek verfügbar
The approved original version of this thesis is available in print at TU Wien Bibliothek.

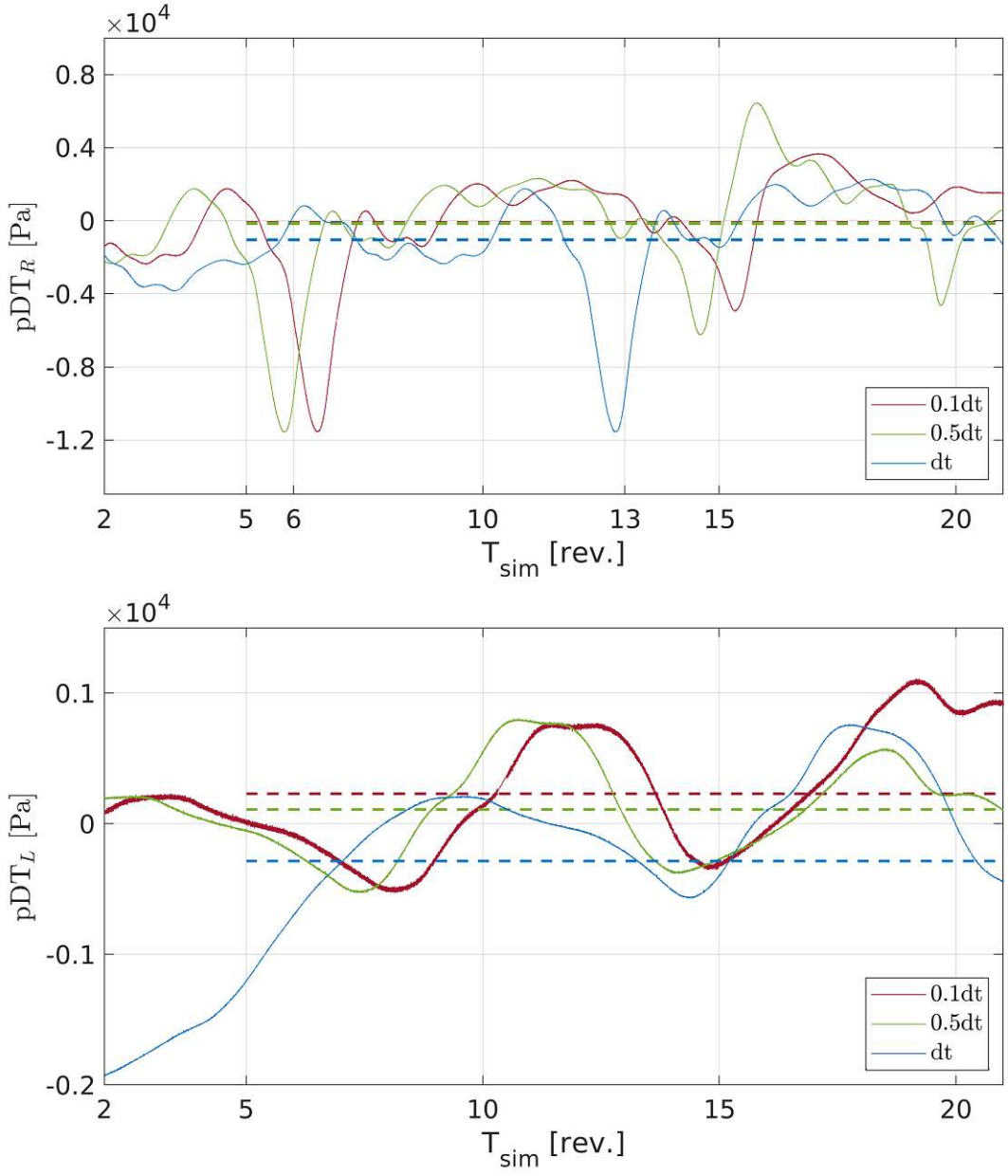

Figure 5.7: Draft tube wall pressure: top - right, bottom - left

Die approbierte gedruckte Originalversion dieser Diplomarbeit ist an der TU Wien Bibliothek verfügbar
The approved original version of this thesis is available in print at TU Wien Bibliothek.

Additional monitor points are located at the wall in the draft tube cone region. The FFT analysis of this signal, that is monitored in the time domain, yields a more conclusive representation in it's frequency domain. Figure 5.8 compares the FFT analysis of each conducted simulation with different timestep sizes. It displays the absolute value of the pressure amplitude over it's frequency, normalized by the runner rotational frequency f_n. In addition, the signal of the conducted measurement is superpositioned in black.

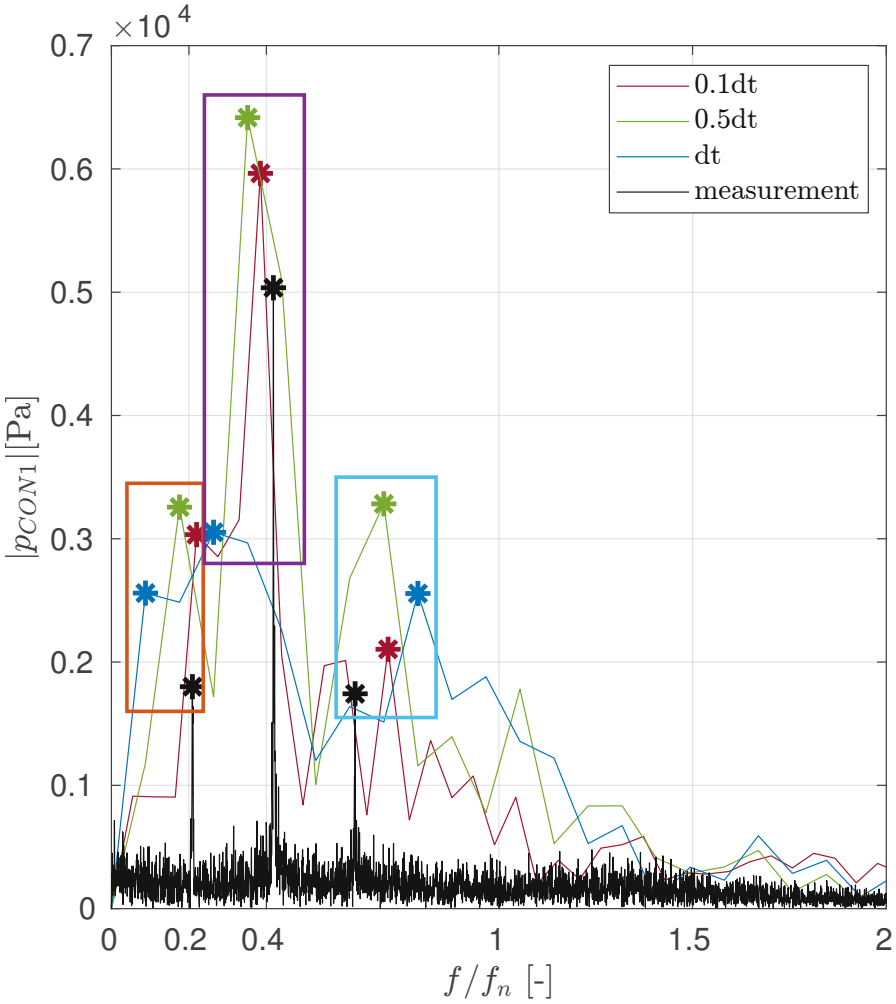

Figure 5.8: FFT signal of draft tube cone pressure for varying timestep sizes

Independent of the timestep size, the three distinctive peaks revealed by the measured signal, are also obtained in each performed simulation. Colored squares (orange - first peak, purple - second peak, and teal - third peak) mark the region of corresponding amplitudes of each peak.

Die approbierte gedruckte Originalversion dieser Diplomarbeit ist an der TU Wien Bibliothek verfügbar
The approved original version of this thesis is available in print at TU Wien Bibliothek.
TU Bibliothek Your knowledge hub WIEN

It is readily seen, that the coarse timestep size dt (blue), is not only off in regards to the occuring frequency, but also underpredicts the main pressure amplitude in the purple square by almost half, when compared to the measured signal (black). The simulated occuring frequencies for the refined simulations (0.5dt - green, 0.1dt - red) on the other hand, are well in alignement with the measured ones. With the exception of the aforementioned underpredicted pressure amplitude, all other amplitudes are overpredicted. Interestingly, the 0.5dt peaks (green) show the largest deviation, when compared to all three occuring measured peaks. Overall, the 0.1dt result showcases the closest resemble to the measurement in regards to both, the occuring frequency and the magnitude of the pressure amplitude. The first red peak of the less distinctive looking shape in the teal square, which shows a slightly lower amplitude than the marked one (red asterisk), almost perfectly matches the measured amplitude (dark asterisk).

Figure 5.8 undeniably supports the necessity for smaller timestep sizes. It showcases the potential to obtain pressure amplitudes as well as occuring frequencies, that resemble the measurement more accurately, in comparison to the results of the coarse timestep size simulation. Although evaluted in the draft tube cone region, it can be fairly assumed, that this potential is also true for the pressure field that acts on the runner surface. The follow up fatigue analysis and the lifetime assessment of the Francis runner is strongly dependent on this pressure field, hence the prediction of the correct frequencies as well as amplitudes, is key to obtain a realistic runner's lifetime prediction.

5.3 Influence of Spacial Parameters

In the course of the conducted GIS in part-load operating condition, a total of 70 runner revolutions, all invoking the same timestep size, but with different total mesh sizes (see table 4.3), have been simulated. A detailed description of the procedure is provided by Celik et al. [62]. It is the recommended method to estimate the discretisation error. The procedure with it's equations, are groundlaying for the MATLAB code (appendix A.1), which has been tested to yield the same results for the sample calculations, that are provided in the research paper.

Die approbierte gedruckte Originalversion dieser Diplomarbeit ist an der TU Wien Bibliothek verfügbar
The approved original version of this thesis is available in print at TU Wien Bibliothek.
TU Bibliothek Your knowledge hub WIEN

The key variables, that are evaluated in the course of the grid convergence method, are the three global parameters, namely head H, mechanical power P_{mech} and the hydraulic efficiency η_h. As already mentioned, and owed to the fact, that only available meshes are considered for the conducted simulations, the desirable refinement factor, and a systematic mesh refinement, as suggested by to the research paper, is not achieved.

Before proceeding to the results of the performed GIS, the signal of the three monitored global parameters, along the simulated runner revolutions is displayed in figure 5.9. It showcases the behaviour of different mesh sizes on the global parameters. A significant value band drop, as already explained in chapter 5.2.1, is evident at the same threshold of 25 runner rotations for all simulated mesh sizes. The amount of available monitoring data for each spatially refined simulation, allows to compare the parameters in the range from 25 to 70 runner rotations. Hence, the change of the mean values, when comparing the signal's mean for the first 20 (five to 25), to the mean value of the following 45 rotations, is not displayed. It is only stated, that in case of every global parameter, the variation of each mean value, evaluated after the threshold of 25 rotations, with respect to the mean of the initial (20) runner revolutions, is within 0.12%.

Comparing the signals of the hydraulic efficiency and the head (top and middle graph in figure 5.9), a similar behaviour, with one noticeable exception at around 55 runner rotations, for all mesh sizes (fine - red, medium - green, and coarse - blue) is evident. In reference to the coarse (blue) mesh simulation, both refined meshes slightly increase the hydraulic efficiency by $\approx 0.004\%$, in case of the medium mesh (green), and by $\approx 0.02\%$, in case of the fine mesh (red). The medium mesh (green) predicts a slighlty higher mean head value (by ≈ 0.004m), while the solution of simulation which invokes the finest mesh size (red), yields a lower mean value (by ≈ 0.02m) for the monitored head, all in reference to the coarse mesh.

Same behaviour is also evident for the mechanical power (bottom graph). The medium mesh (green) increases the mean value of the mechanical power, while the fine mesh (red) decreases it. The difference between the solutions of the medium and coarse mesh simulations, in terms of mean value are $\approx 4.2 \times 10^3$W between the coarse and medium, and $\approx 1.3 \times 10^4$W between the coarse and fine mesh simulation.

Die approbierte gedruckte Originalversion dieser Diplomarbeit ist an der TU Wien Bibliothek verfügbar
The approved original version of this thesis is available in print at TU Wien Bibliothek.
TU Bibliothek Your knowledge hub WIEN

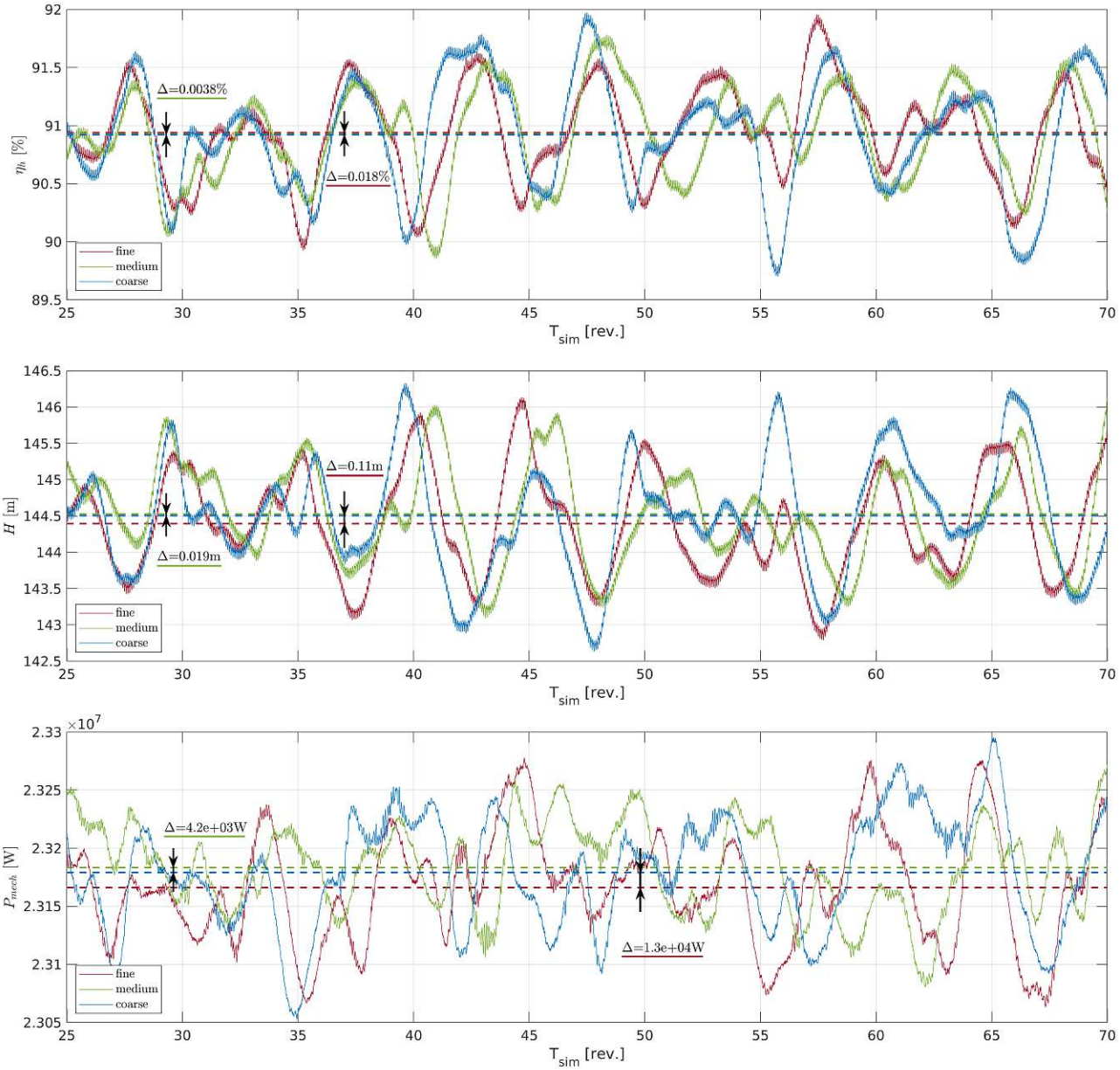

Figure 5.9: Monitored global variables for different mesh sizes

The change of the mean values in the opposite direction, in case of the monitored head and the mechanical power, is unexpected. So far, the mean values of the refined simulations have always shifted in the same direction (compare figures 5.6, and 5.7), with respect to the evaluated coarse mean value (blue). A reason for this inconsistent behaviour along spatial refinement, is probably an insuffienciently

Die approbierte gedruckte Originalversion dieser Diplomarbeit ist an der TU Wien Bibliothek verfügbar
The approved original version of this thesis is available in print at TU Wien Bibliothek.
TU Bibliothek Your knowledge hub WIEN

small timestep size. Simulations invoking simultaneous, spatial and temporal refinement, are likely to reveal a consistent pattern regarding the increase or decrease of the evaluated mean values of the global parameters. Due to the mentioned, considerable long wall clock times, such computations have not been conducted.

Figure 5.10 displays the pressure amplitude over the normalized frequency range, of the pressure signal that is tracked by the second monitor point in the draft tube cone region. This monitor point is located at the draft tube wall, approximately one meter below the first monitor point (p_{CON1}, fig. 5.8). It is again superpositioned by the transformed signal of the measurement (black).

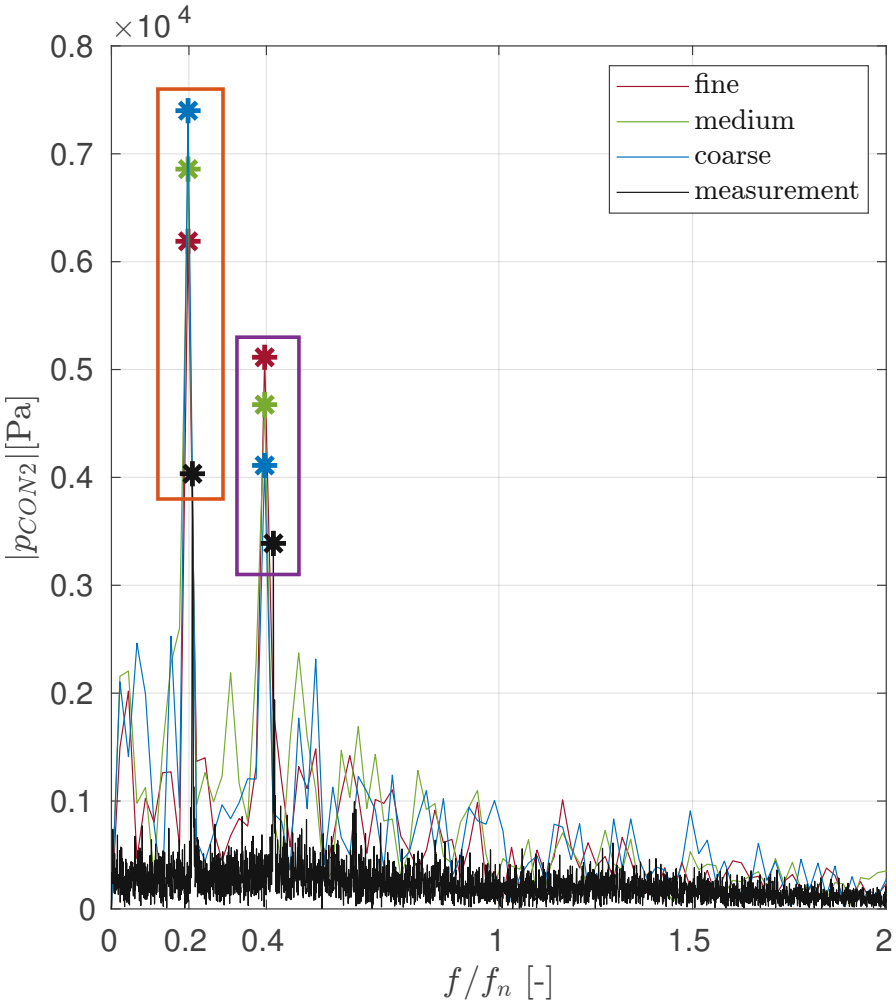

Figure 5.10: FFT signal of draft tube cone pressure for varying mesh sizes

Die approbierte gedruckte Originalversion dieser Diplomarbeit ist an der TU Wien Bibliothek verfügbar
The approved original version of this thesis is available in print at TU Wien Bibliothek.

Again, the occuring frequencies of the two distinct pressure peaks are very well in alignment with the measured ones. However, the coarse mesh (blue) overpredicts the magnitude of this first peak by almost a double of the measured amplitude. Quite the overprediction is also true for the medium as well as the fine mesh size. While the first pressure amplitude consistently decreases along spatial refinement, the second one (purple square) shows an opposite behaviour. With increasing cell counts, the amplitude of the second peak shifts towards higher magnitudes. Simultanious spatial and temporal refinement is likely to reveal a more conclusive pattern as well as a closer resemblance off the measured signal.

5.3.1 Grid Independency Study

The procedure, for the estimation of the discretisation error, follows the exact same steps as provided by Celik et al. [62]. Table 5.1 summarized the results in the same manner according to the research paper. In addition, the representative cell size

	η_h	H	P_{mech}
N_1, N_2, N_3 [1]	20.723, 11.568, 8.746		
h_1, h_2, h_3	0.0038, 0.0048, 0.0055		
r_{21}	1.2641		
r_{32}	1.1341		
ϕ_1	90.9402	144.3947	2.3166e+07
ϕ_2	90.9257	144.5254	2.3183e+07
ϕ_3	90.9219	144.5064	2.3179e+07
p	2.4404	6.1009	4.5594
ϕ_{ext}^{21}	90.9591	144.3536	2.3157e+07
ϕ_{ext}^{32}	90.9363	144.5419	2.3189e+07
e_a^{21}	0.0160%	0.0905%	0.0746%
e_a^{32}	0.0042%	0.0132%	0.0182%
e_{ext}^{21}	0.0207%	0.0285%	0.0390%
e_{ext}^{32}	0.0117%	0.0114%	0.0234%
GCI_{21}	0.0259%	0.0356%	0.0488%
GCI_{32}	0.0146%	0.0143%	0.0293%

[1] in [mio.]

Table 5.1: Calculations of the discretisation error

Die approbierte gedruckte Originalversion dieser Diplomarbeit ist an der TU Wien Bibliothek verfügbar
The approved original version of this thesis is available in print at TU Wien Bibliothek.

h, of each mesh is documented as well. The subscripts $_1$, $_2$, and $_3$ stand for the fine, medium, and coarse mesh, respectively. An estimation of the grid convergence behaviour can be made, based on the discriminating ratio R:

$$R = \frac{\phi_1 - \phi_2}{\phi_2 - \phi_3} \tag{5.2}$$

Although it is argumented by Eça and Hoekstra [64], that the equation (5.2), to determine the convergence behaviour, is only good for constant grid refinement ratios ($h_2/h_1 = h_3/h_2$), the outcome of the equation is in good agreement with the upcoming graphical representation. Based on this equation, a monotonic divergence in case of the monitored hydraulic efficiency, and an oscillatory divergence for both, the head, and the mechanical power has to be reported.

This behaviour is readily seen in figures 5.11 and 5.12. Both display the global parameters, normalized by the the extrapolated parameter, which is calculated from the results of two mesh sizes and the convergence order p. The extrapolated

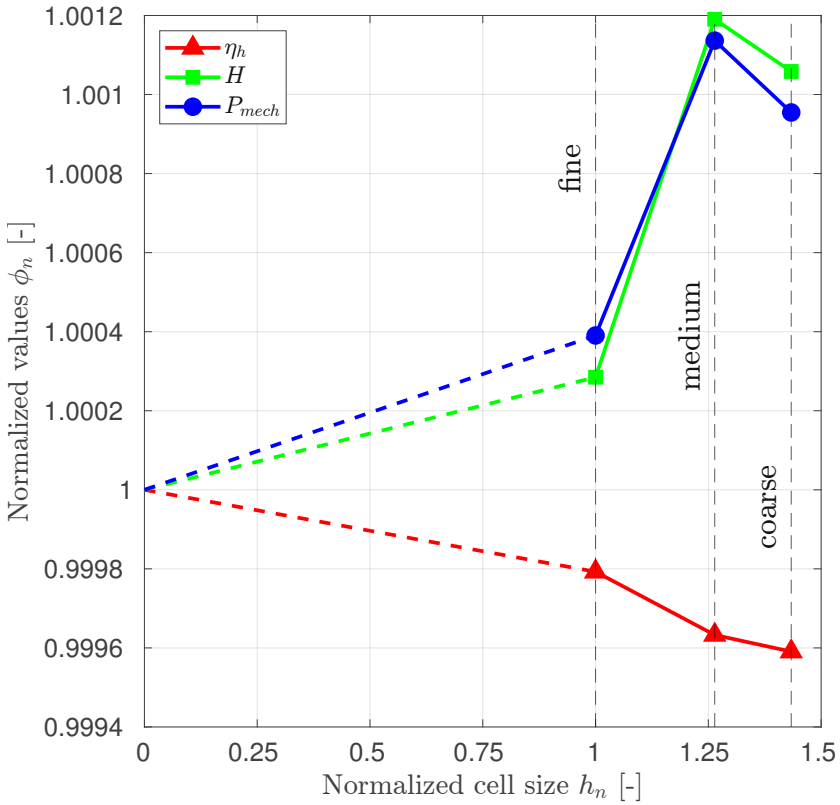

Figure 5.11: Grid convergence, normalized by ϕ_{ext}^{21}

Die approbierte gedruckte Originalversion dieser Diplomarbeit ist an der TU Wien Bibliothek verfügbar
The approved original version of this thesis is available in print at TU Wien Bibliothek.

values represent the mesh independent solution ($h \longrightarrow 0$), based on either the coarse-medium (ϕ_{ext}^{32}), or medium-fine results (ϕ_{ext}^{21}). The horizontal axis represents the normalized cell size h_n, and the vertical black dashed lines help to visualize the convergence rate between the mesh sizes.

Figure 5.11 showcases the convergence behaviour for each global parameter, normalized by ϕ_{ext}^{21}. An oscillatory divergence, in case of the mechanical power (blue) and the head (green), and a monotonic divergence in case of the hydraulic efficiency (red), is obtained. The same behaviour is showcased, when the global parameters are normalized by ϕ_{ext}^{32} (fig. 5.12).

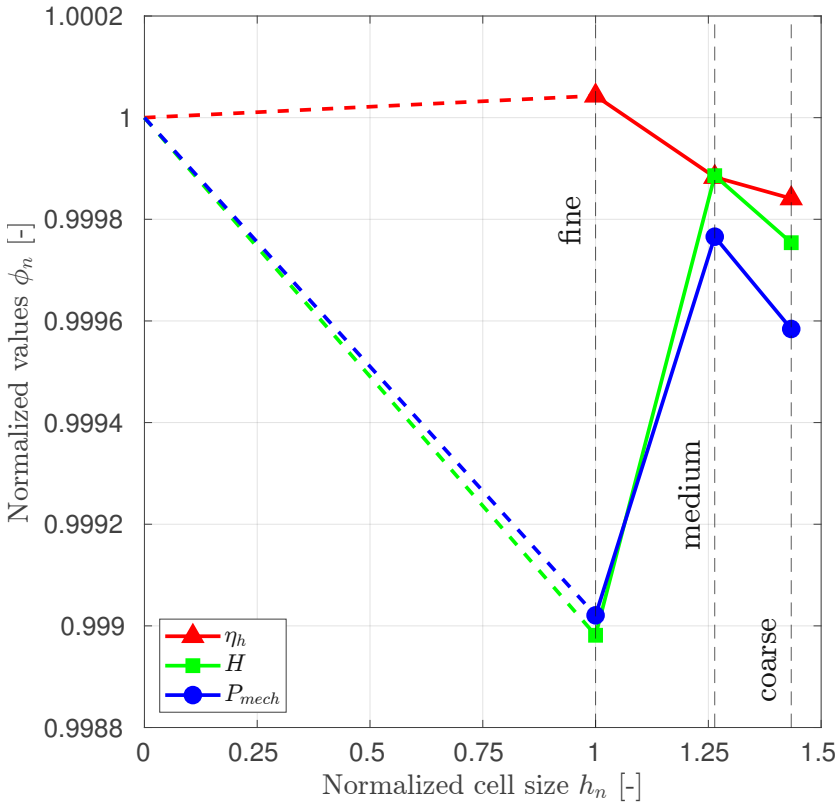

Figure 5.12: Grid convergence, normalized by ϕ_{ext}^{32}

Reasons for the divergence of each global parameter can be related to the inconsistent refinement ratios. They directly have an influence on the apparent order of the grid convergence p (see table 5.1), and values, greater than the formal order of the scheme (2nd-Order), are obtained.

Die approbierte gedruckte Originalversion dieser Diplomarbeit ist an der TU Wien Bibliothek verfügbar
The approved original version of this thesis is available in print at TU Wien Bibliothek.

Another reason, that adds up to the outcoming divergence, is a direct consequence of the differences between the results of two mesh sizes, $\varepsilon_{32} = \phi_3 - \phi_2$ or $\varepsilon_{21} = \phi_2 - \phi_1$. In the research paper of Celik et al. ([62]), it is reported, that the method does not work for ε-values "close to zero", which is likely the case between the coarse and medium mesh results.

In any case, the grid convergence index (GCI) is below one percentage point (see table 5.1), which, according to Roache ([65]) indicates a satisfactory discretisation error. More interestingly, the grid convergence index is almost half the index between the medium and fine mesh (GCI_{21}), when performing the procedure between to coarse and medium mesh (GCI_{32}). This is readily seen in figure 5.12. The solution values of all global parameters are located closely to the normalized solution value 1 in case of the medium mesh results. This is an indication, that the combination of the medium mesh and the coarse timestep dt, is satisfactory, especially when considering the computational effort, refined simulations require.

Although the reported oscillating behaviour of the global parameters, it must be realized, that even the largest deviation (in case of fig. 5.11 the head for the medium mesh, and in case of fig. 5.12 the head for the fine mesh), of the normalized global parameters, is off by 0.0012 and 0.00102 respectively, when compared to mesh independent solution ($h \longrightarrow 0$). The normalized global parameters, oscillate very close around this mesh independent solution ($\phi_n = 1$).

To end chapter five, upcoming figure (fig. 5.13) showcases the deviation of the evaluated mean values of said global parameters, when compared to the conducted measurements. According to the equation, which describes the relative deviation in percentage points for any variable:

$$|\delta| = |\frac{measurement - simulation}{measurement}| * 100\% \tag{5.3}$$

the deviation of each global parameter, is conveniently displayed by means of a bar plot. In figure 5.13 it is readily seen, that regardless of the applied refinement (temporal or spatial), the influence on the evaluated means is close to negligible.

Die approbierte gedruckte Originalversion dieser Diplomarbeit ist an der TU Wien Bibliothek verfügbar
The approved original version of this thesis is available in print at TU Wien Bibliothek.
TU Bibliothek Your knowledge hub WIEN

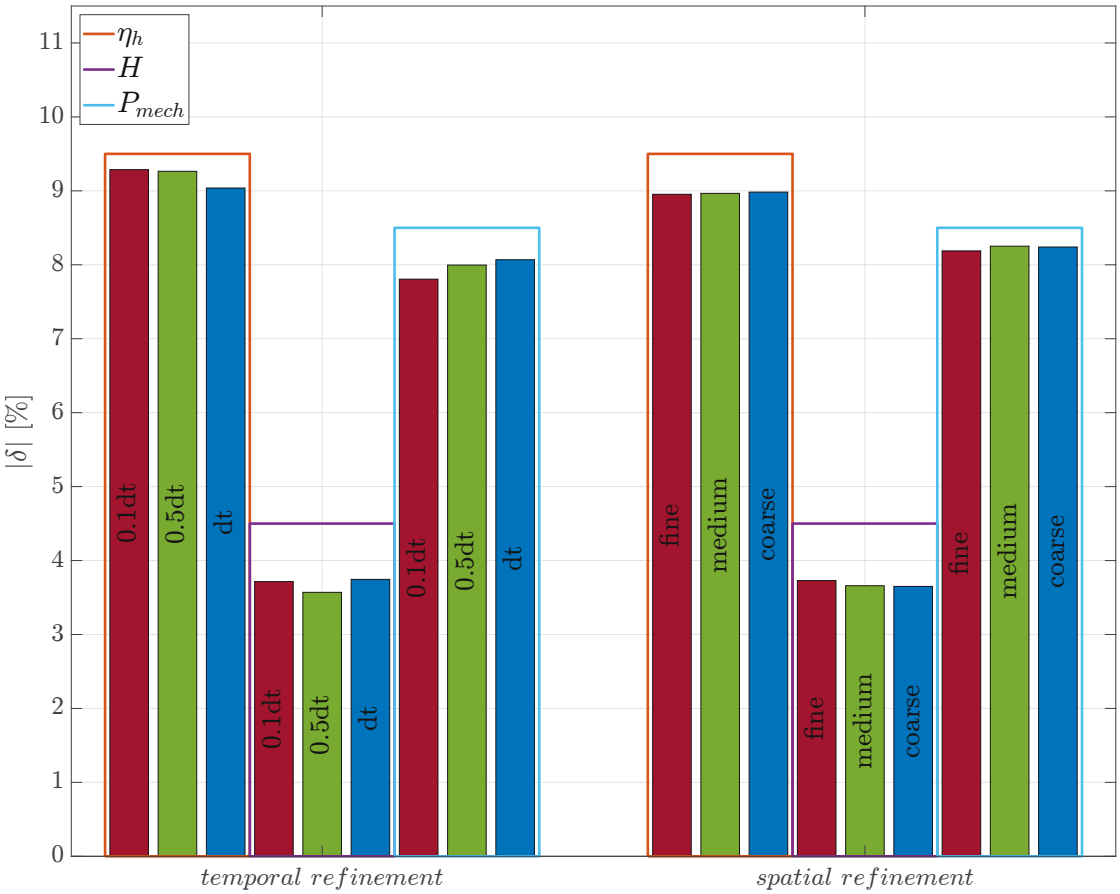

Figure 5.13: Comparison to measurement

As already mentioned, the temporal refinement has a higher potential to shift the mean values of the global parameters, while the spatial refinement hints a noticeable difference between the bars, only in case of the head (purple square) and the mechanical power (teal square).

Nevertheless, the relative deviation for all global parameters, independet of the applied refinement is very well below 10%. In case of the head, the deviation to the measurement is even below 4%. Considering the temporal refinement, the most increased computational effort (the 0.1dt simulation) has a positive effect only on the result of the evaluated mechanical power. Interestingly, the simulation which invokes the coarse timestep size, dt, obtains the smallest relative deviation to the measured hydraulic efficiency (orange square).

Die approbierte gedruckte Originalversion dieser Diplomarbeit ist an der TU Wien Bibliothek verfügbar
The approved original version of this thesis is available in print at TU Wien Bibliothek.

To get a better feeling for the required computational effort, the effective wall clock time off each temporally refined simulation is summarized in table 5.2. Spatial refinement does not change the wall clock time significantly. Regardless of the cell count, seven full runner rotations could be simulated within ∼2.5-3 days (timestep-size dt). Taking the queuing time into consideration, a delay every submitted job has to suffer, on top of occasional shutdowns of the HPC (High performance cluster) during a running computation, it is safe to say that at least 3 days are required to simulate seven full runner rotations.

Timestep	[°]	dt [s]	T_{sim} [rev.]	Wall clock time [d]
dt	1	3.8889e-4	7	≈ 3
0.5dt	0.5	1.9444e-4	3.5	≈ 3
0.1dt	0.1	3.8889e-5	0.7	≈ 3

Table 5.2: Summary of computational wall clock time

Die approbierte gedruckte Originalversion dieser Diplomarbeit ist an der TU Wien Bibliothek verfügbar
The approved original version of this thesis is available in print at TU Wien Bibliothek.

Chapter 6

Conclusion

The object of this thesis was to investigate the influence of spatial (grid refinement) and temporal (simulation duration T_{sim} and varying timestep sizes) parameters on, the conducted CFD simulations of a Francis runner, which operates in part-load region. Three different total mesh sizes (fine - medium - coarse), based on their cell count, and three different timestep sizes (0.1dt - 0.5dt - dt), that correlate to time in seconds, the investigated runner requires to rotate by 0.1°, 0.5°, and 1°, respectively, are chosen to be evaluated.

The correlation between the timestep size, and one (fraction of one) degree of a single runner rotation, allows for the convenient documentation of the monitored parameters, over the amount of simulated runner revolutions. So far, the longest simulation duration, which has been performed by predecessor Schmelz ([5]), marks a total of 30 runner revolutions with a timestep size, corresponding to 5° of a single runner rotation. To further investigate the influence of the simulation duration, the computations for each different mesh size, have been prolonged, until a total of approximately 70 runner revolutions are simulated.

Although all simulations have been performed, harnessing the computational nodes provided by the VSC-4 (fastest supercomputer in Austria), considerable long wall clock times only allowed to prolong the simulations until the threshold of 70 full runner rotations. All prolonged simulations up to this threshold invoke the coarsest timestep size dt, which corresponds to a single degree of a runner revolution. In summary, a total of 70 runner revolutions have been simulated in

Die approbierte gedruckte Originalversion dieser Diplomarbeit ist an der TU Wien Bibliothek verfügbar
The approved original version of this thesis is available in print at TU Wien Bibliothek.
TU Bibliothek Your knowledge hub WIEN

the course of the conducted GIS, for the three different mesh sizes. The drastic increase (see table 5.2) of computational effort in case of the simulations with a refined timestep size, 0.1dt and 0.5dt respectively, allowed for the simulation of approximately 21 total runner rotations only. All temporally refined simulations have been conducted with the medium mesh size.

A quite significant change of the value band (fg. 5.5), in case of the prolonged simulations, could be obtained. The range from peak to valley, for all monitored global parameters, almost instantaneously drops by approximately 30%, at the threshold of 25 runner rotations. The monitored signal of each global parameter sustains in the decreased value band range for the remaining 44 simulated runner revolutions. This is a strong indication, that the solution in the range between 25 and 69 must be considered as the more accurate one.

The evaluated mean values of the global parameters, compared between the first 10 and the follow up 54 runner rotations, do not vary as significantly, such as the value band. For every global parameter, the computational effort necessary to calculate until 69 runner rotations, increases the mean value, with respect to the evaluated mean of the first ten revolutions. Expressed in total values, the hydraulic efficiency rises by 0.082% and the head is predicted 0.225m higher. The most visible increase between the mean value of the first ten, compared to the mean value, evaluated for the follow up 54 rotations, is evident in case of the mechanical power. In total numbers, the mechanical power increases by 55.3kW.

A different pattern is obtained in case of the temporally refined simulations (fig. 5.6). While the mean hydraulic efficiency in case of the refined timestep sizes, decreases by 0.25% (0.1dt), and 0.23% (0.5dt), when compared to the mean value of the coarse results (dt), an increase becomes evident for the mean head value. A decrease is also obtained in case of the mechanical power. So far, computational effort led to a shift of all global paramters in the same direction. The mean value of the monitored head breaks this consistent behaviour. Only a slight increase of 0.044m is evident between the 0.1dt and the coarse timestep size dt, while a larger increase of 0.26m results between the coarse and the 0.5dt simulation.

No such pattern is evident for spatially refined simulations (fig. 5.9). Larger cell counts yield an increase in the hydraulic efficiency by 0.0038%, in case of the

Die approbierte gedruckte Originalversion dieser Diplomarbeit ist an der TU Wien Bibliothek verfügbar
The approved original version of this thesis is available in print at TU Wien Bibliothek.
TU Bibliothek Your knowledge hub WIEN

medium mesh, and by 0.018% for the fine mesh, all in reference to the mesh with the smallest cell count. A change in the opposite direction, with respect to the coarse mean values, is obtained for the mechanical power and the head. While the medium mesh predicts a slightly higher mean value (0.019m/4.2kW), the fine mesh shows a decreasing mean value (0.11m/13kW) in case of the two parameters (H and P_{mech}). This inconsistency, especially the change in the opposite direction of the mean values of the global parameters head an mechanical power, is likely to be related to an insufficiently small timestep size in case of the simualtion with the largest cell count.

Another inconsistent pattern is obtained for the pressure signal in the draft tube cone (fig. 5.8), in case of the temporally refined simulations. While both refined timesteps increase the pressure amplitude, the 0.5dt simulation predicts a higher magnitude than the 0.1dt results. However, the pressure peaks for the refined simulations are of the same order of magnitude and quite significantly double the pressure peak, that is obtained by the simulation, which invokes the coarse timestep size. The occuring frequency on the other hand, consistently moves to later instances, along the refined timestep sizes.

The pressure amplitudes in the draft tube cone (fig. 5.10) show a consistent behaviour along the spatial refinement. More cell counts decrease the first pressure peak, while the second pressure peak increases. The occuring frequencies remain at the same point in time.

In conclusion, the refined simulations in both cases (temporal and spatial refinement), do not obtain a significant change in mean values of the monitored global parameters. In reference to each coarse simulation (coarse timestep size dt or coarse mesh size), the mean values of the refined simulations, deviate by less than 0.27% in case of the temporal, and by less by than 0.07% in case of the spatial refinement. This allows for the argumentation, that a refined timestep size has a greater potential to shift the mean values of the monitored global parameters.

A consistent pattern, in regards to the direction of the shift (increase or decrease), is not obtained. Simulations with simultaneous temporal and spatial refinement are likely to reveal a conclusive behaviour. A quite small percentagewise change in mean values (0.2%) is also evident, when comparing the initial ten, to follow up runner rotations. However, the sudden value band drop, after a threshold of 25

Die approbierte gedruckte Originalversion dieser Diplomarbeit ist an der TU Wien Bibliothek verfügbar
The approved original version of this thesis is available in print at TU Wien Bibliothek.
TU Bibliothek Your knowledge hub WIEN

runner rotations is significant. Comparing the peak to valley value band, between the two regions befor and after 25 runner rotations, obtains a drop of 30%.

When comparing all monitored signals for the temporal refinement, the similar behaviour between the 0.5dt and the 0.1dt results is undeniable. Hence, and with computational effort in mind, the 0.5dt timestep size can be considered the sweet spot, in terms of necessary temporal refinement. A more or less shifted behaviour of each signal, compared to the finest timestep size, is recognized.

However, the computational wall clock time increases considerably in case of the 0.5dt simulation. This circumstance is even more pronounced in case of the 0.1dt simulation. Computational hours can be estimated to increase by a factor of two between the dt and 0.5dt, and by a factor of five between the 0.5dt and 0.1dt simulation. If for example the hydraulic efficiency (fig. 5.6) is taken into consideration, it can be argumented, that ten times the computational effort (in terms of required calculation hours), obtains a decrease in efficiency by a quarter of a percentage point. Such small shifts of the mean values are evident for all monitored parameters (see fig. 5.13) and a priorly determined focus on the outcoming results, must decide wether temporal refinement is necessary or not. Without a doubt, smaller timestep sizes correlate to a more trustworthy visualization of the turbulent structures and furthermore the pressure peaks as well as the occuring frequency are predicted much closer to measurement.

The results of the conducted grid independency study are somewhat unsatisfactory. All monitored global parameters show a divergent behaviour in the range from 25 to 70 runner rotations. A small consolation is obtained, when evaluating the GIS in a different runner rotation range. Since the MATLAB code easily allows to adjust the calculation range in terms of runner rotations, a monotonic convergence for the hydraulic efficiency and an oscillatory convergence for the monitored head, is obtained in the range between 40 to 50 runner rotations. The mechanical power still reports an oscillatory divergence.

A probable reason for the somewhat inconclusive results of the conducted GIS, might be the influence of the inital condition. Only one initial (steady state) solution, with a guide vane angle, that corresponds to the best efficiency operating point, has been simulated. Every follow up simulation is based on this initial

Die approbierte gedruckte Originalversion dieser Diplomarbeit ist an der TU Wien Bibliothek verfügbar
The approved original version of this thesis is available in print at TU Wien Bibliothek.
TU Bibliothek Your knowledge hub WIEN

simulation. The combination of a changing guide vane angle in part-load region, and the varying discharge Q (inlet BC), are likely to yield different initial values, the unsteady simulation in part-load operating region should be based on. Lastly, the influence of insufficiently refined wall regions across the whole computational domain, needs to be quantified as well, to allow further argumentation and to effectively estimate each influence (time step, simulation time, mesh size, intial conditon, wall refinement), on the conducted simulation, seperatly.

Die approbierte gedruckte Originalversion dieser Diplomarbeit ist an der TU Wien Bibliothek verfügbar
The approved original version of this thesis is available in print at TU Wien Bibliothek.

Bibliography

[1] M. Guittet, M. Capezzali, L. Gaudard, F. Romerio, F. Vuille, and F. Avellan, "Study of the drivers and asset management of pumped-storage power plants historical and geographical perspective," *Energy*, vol. 111, pp. 560–579, 2016.

[2] M. Eichhorn, *Fatigue Analysis of Prototype Francis Turbines Using Numerical Simulations and Site Measurements*. PhD thesis, TU Wien - Institut für Energietechnik und Thermodynamik, 2017.

[3] X. Huang, J. Chamberland-Lauzon, C. Oram, A. Klopfer, and N. Ruchonnet, "Fatigue analyses of the prototype francis runners based on site measurements and simulations," *IOP Conference Series: Earth and Environmental Science*, vol. 22, p. 012014, mar 2014.

[4] J. Unterluggauer, *Investigations on Critical Low-Load and Transient Operation of a Prototype Francis Turbine*. PhD thesis, TU Wien - Institut für Energietechnik und Thermodynamik, 2019.

[5] A. A. Schmelz, "Numerische simulation von stabilisierungsluft in einer francisturbine," Master's thesis, TU Wien - Institut für Energietechnik und Thermodynamik, 2019.

[6] J. Giesecke, S. Heimerl, and E. Mosonyi, *Wasserkraftanlagen*. Springer Vieweg Berlin, Heidelberg, 2014.

[7] C. Bauer, *Hydraulische Maschinen und Anlagen I & II: Vorlesungsskriptum*. Institut für Energietechnik und Thermodynamik - Forschungsbereich Strömungsmaschinen, TU Wien, 2015.

[8] W. Bohl and W. Elmendorf, *Strömungsmaschinen 1*. Vogel Buchverlag, 10. Auflage, 2008.

Die approbierte gedruckte Originalversion dieser Diplomarbeit ist an der TU Wien Bibliothek verfügbar
The approved original version of this thesis is available in print at TU Wien Bibliothek.
TU Bibliothek Your knowledge hub WIEN

[9] M. V. Magnoli, *Numerical simulation of pressure oscillations in large Francis turbines at partial and full load operating conditions and their effects on the runner structural behaviour and fatigue life*. PhD thesis, TU München - Institut für Energietechnik MW7, 2014.

[10] M. Wachauer, *Numerische Lebensdauerberechnung einer Francis Turbine im Auslegungspunkt*. PhD thesis, TU Wien, 2016.

[11] M. V. Magnoli and M. Maiwald, "Influence of hydraulic design on stability and on pressure pulsations in francis turbines at overload, part load and deep part load based on numerical simulations and experimental model test results," *IOP Conference Series: Earth and Environmental Science*, vol. 22, p. 032013, mar 2014.

[12] D. Štefan, M. Hudec, V. Uruba, P. Procházka, O. Urban, and P. Rudolf, "Experimental investigation of swirl number influence on spiral vortex structure dynamics," *IOP Conference Series: Earth and Environmental Science*, vol. 774, p. 012085, jun 2021.

[13] C. Nicolet, A. Zobeiri, P. Maruzewski, and F. Avellan, "On the upper part load vortex rope in francis turbine: Experimental investigation," *IOP Conference Series: Earth and Environmental Science*, vol. 12, p. 012053, aug 2010.

[14] P. Davidson, *Turbulence: An Introduction for Scientists and Engineers*. Oxford University Press, 2015.

[15] P. Conrad, W. Weber, and A. Jung, "Deep part load flow analysis in a francis model turbine by means of two-phase unsteady flow simulations," *Journal of Physics: Conference Series*, vol. 813, p. 012027, 04 2017.

[16] B. Nennemann, J. F. Morissette, J. Chamberland-Lauzon, C. Monette, O. Braun, M. Melot, A. Coutu, J. Nicolle, and A. M. Giroux, "Challenges in dynamic pressure and stress predictions at no-load operation in hydraulic turbines," *IOP Conference Series: Earth and Environmental Science*, vol. 22, p. 032055, mar 2014.

[17] H. Keck and M. Sick, "Thirty years of numerical flow simulation in hydraulic turbomachines," *Acta Mechanica*, vol. 201, pp. 211–229, 01 2008.

Die approbierte gedruckte Originalversion dieser Diplomarbeit ist an der TU Wien Bibliothek verfügbar
The approved original version of this thesis is available in print at TU Wien Bibliothek.

[18] M. Sick, W. Michler, T. Weiss, and H. Keck, "Recent developments in the dynamic analysis of water turbines," *Proceedings of the Institution of Mechanical Engineers, Part A: Journal of Power and Energy*, vol. 223, no. 4, pp. 415–427, 2009.

[19] C. Trivedi, M. Cervantes, and O. Dahlhaug, "Experimental and numerical studies of a high-head francis turbine: A review of the francis-99 test case," *Energies*, vol. 9, p. 74, 01 2016.

[20] Trivedi, Chirag and Cervantes, Michel J., "State of the art in numerical simulation of high head francis turbines," *Renew. Energy Environ. Sustain.*, vol. 1, p. 20, 2016.

[21] D. Čelič and H. Ondráčka, "The influence of disc friction losses and labyrinth losses on efficiency of high head francis turbine," *Journal of Physics: Conference Series*, vol. 579, p. 012007, 01 2015.

[22] T. Krappel, A. Ruprecht, S. Riedelbauch, R. Jester-Zuerker, and A. Jung, "Investigation of francis turbine part load instabilities using flow simulations with a hybrid rans-les turbulence model," *IOP Conference Series: Earth and Environmental Science*, vol. 22, p. 032001, mar 2014.

[23] T. Krappel, S. Riedelbauch, R. Jester-Zuerker, A. Jung, B. Flurl, F. Unger, and P. Galpin, "Turbulence resolving flow simulations of a francis turbine in part load using highly parallel cfd simulations," *IOP Conference Series: Earth and Environmental Science*, vol. 49, p. 062014, nov 2016.

[24] T. Krappel, A. Ruprecht, and S. Riedelbauch, "Turbulence resolving flow simulations of a francis turbine with a commercial cfd code," in *High Performance Computing in Science and Engineering '15* (W. E. Nagel, D. H. Kröner, and M. M. Resch, eds.), (Cham), pp. 421–433, Springer International Publishing, 2016.

[25] L. da Vinci, "Studies of water passing obstacles and falling." https://upload.wikimedia.org/wikipedia/commons/9/98/Studies_of_Water_passing_Obstacles_and_falling.jpg, 1508-1509. Accessed: 2023-02-05.

[26] H. Tennekes and J. L. Lumley, *A First Course in Turbulence*. The MIT Press, 03 1972.

Die approbierte gedruckte Originalversion dieser Diplomarbeit ist an der TU Wien Bibliothek verfügbar
The approved original version of this thesis is available in print at TU Wien Bibliothek.

[27] H. Jasak, *Error Analysis and Estimation for the Finite Volume Method With Applications to Fluid Flows*. PhD thesis, 01 1996.

[28] T. Holzmann, *Mathematics, Numerics, Derivations and OpenFOAM®*. 11 2019.

[29] J. H. Ferziger and M. Perić, *Computational Methods for Fluid Dynamics*. Springer Nature Switzerland AG 2020, fourth ed., 2020.

[30] C. Greenshields and H. Weller, *Notes on Computational Fluid Dynamics: General Principles*. Reading, UK: CFD Direct Ltd, 2022.

[31] B. Scheichl, *Turbulent Flows: Lecture Script*. Institut für Strömungsmechanik und Wärmeübertragung - Forschungsbereich Strömungsmechanik, TU Wien, 2016.

[32] R. Bird, W. Stewart, and E. Lightfoot, *Transport Phenomena*. J. Wiley, 2002.

[33] D. Wilcox, *Turbulence Modeling for CFD*. No. Bd. 1 in Turbulence Modeling for CFD, DCW Industries, 2006.

[34] C. H. Kuhlmann, *Numerische Methoden der Strömungsmechanik: Vorlesungsskript*. Institut für Strömungsmechanik und Wärmeübertragung - Forschungsbereich Numerische Strömungsmechanik, TU Wien, 2021.

[35] J. Blazek, "Chapter 7 - turbulence modelling," in *Computational Fluid Dynamics: Principles and Applications (Second Edition)* (J. Blazek, ed.), pp. 227–270, Oxford: Elsevier Science, second edition ed., 2005.

[36] P. Mössinger, R. Jester-Zürker, and A. Jung, "Investigation of different simulation approaches on a high-head francis turbine and comparison with model test data: Francis-99," *Journal of Physics: Conference Series*, vol. 579, p. 012005, jan 2015.

[37] F. R. Menter, "Improved two-equation k-omega turbulence models for aerodynamic flows," tech. rep., 1992.

[38] F. R. Menter, "Two-equation eddy-viscosity turbulence models for engineering applications," *AIAA Journal*, vol. 32, pp. 1598–1605, 1994.

Die approbierte gedruckte Originalversion dieser Diplomarbeit ist an der TU Wien Bibliothek verfügbar
The approved original version of this thesis is available in print at TU Wien Bibliothek.

[39] J. Decaix, V. Hasmatuchi, M. Titzschkau, and C. Münch-Alligné, "Cfd investigation of a high head francis turbine at speed no-load using advanced urans models," *Applied Sciences*, vol. 8, no. 12, 2018.

[40] J. Schütze, Y. Egorov, and R. Lechner, "Best practice: Scale-resolving simulations in ansys cfd." https://www.ansys.com/content/dam/product/fluids/cfd/tb-best-practices-scale-resolving-models.pdf, 2015. Accessed: 2023-02-26.

[41] J. C. Rotta, *Turbulente Strömungen*, vol. 008 of *Göttinger Klassiker der Strömungsmechanik*. Göttingen: Universitätsverlag Göttingen, 2010.

[42] F. Menter and Y. Egorov, "The scale-adaptive simulation method for unsteady turbulent flow predictions. part 1: Theory and model description," *Flow Turbulence and Combustion*, vol. 85, pp. 113–138, 07 2010.

[43] L. Davidson, "Evaluation of the sst-sas model: Channel flow, asymmetric," 2006.

[44] J. Nicolle and S. Cupillard, "Prediction of dynamic blade loading of the francis-99 turbine," *Journal of Physics: Conference Series*, vol. 579, p. 012001, jan 2015.

[45] F. Menter, R. Lechner, and A. Matyushenko, "Best practice: Rans turbulence modeling in ansys cfd." https://www.ansys.com/content/dam/amp/2022/march/quick-request/Best%20Practice%20RANS%20Turbulence%20Modeling%20in%20Ansys%20CFD.pdf, 2022. Accessed: 2023-02-26.

[46] A. Wimshurst, "Fluid mechanics 101: Inflation layers/prism layers in cfd." https://www.youtube.com/watch?v=1gSHN99I7L4&t=286s, 2021. Accessed: 2023-02-28.

[47] L. Prandtl, "Über flüssigkeitsbewegung bei sehr kleiner reibung." https://germanhistory-intersections.org/de/wissen-und-bildung/ghis:document-202, 1904. Accessed: 2023-05-13.

[48] A. Wimshurst, "Fluid mechanics 101: What are wall functions and how do they work?." https://www.youtube.com/watch?v=fJDYtEGMgzs&t=1032s, 2018. Accessed: 2023-02-28.

[49] ANSYS, "Ansys cfx-solver modeling guide," Release 15.0, 2013.

Die approbierte gedruckte Originalversion dieser Diplomarbeit ist an der TU Wien Bibliothek verfügbar
The approved original version of this thesis is available in print at TU Wien Bibliothek.

[50] ANSYS, "Ansys cfx-solver theory guide," Release 14.0, 2011.

[51] S. Lecheler, *Numerische Strömungsberechnung: Schneller Einstieg in ANSYS CFX 18 durch einfache Beispiele*. Springer Fachmedien Wiesbaden, 2018.

[52] A. Alonzo-García, C. Gutiérrez-Torres, and J. Jiménez-Bernal, *Computational Fluid Dynamics in Turbulent Flow Applications*, pp. 1–24. 08 2016.

[53] P. Bartholomew, F. Denner, M. H. S. Abdol Azis, A. Marquis, and B. Wachem, "Unified formulation of the momentum-weighted interpolation for collocated variable arrangements," *Journal of Computational Physics*, vol. 375, 08 2018.

[54] Y. Saad, *Iterative Methods for Sparse Linear Systems*. Society for Industrial and Applied Mathematics, second ed., 2003.

[55] J. Tu, G.-H. Yeoh, and C. Liu, "Chapter 6 - cfd solution analysis: Essentials," in *Computational Fluid Dynamics (Third Edition)* (J. Tu, G.-H. Yeoh, and C. Liu, eds.), pp. 211–253, Butterworth-Heinemann, third edition ed., 2018.

[56] J. Unterluggauer and E. Doujak, "Fatigue analysis of a prototype francis turbine based on strain gauge measurements," *WASSERWIRTSCHAFT*, vol. 109, pp. 66–71, 09 2019.

[57] J. Unterluggauer, E. Doujak, and C. Bauer, "Numerical fatigue analysis of a prototype francis turbine runner in low-load operation," *International Journal of Turbomachinery, Propulsion and Power*, vol. 4, no. 3, 2019.

[58] J. Unterluggauer, A. Maly, and E. Doujak, "Investigation on the impact of air admission in a prototype francis turbine at low-load operation," *Energies*, vol. 12, no. 15, 2019.

[59] J. Unterluggauer, V. Sulzgruber, E. Doujak, and C. Bauer, "Experimental and numerical study of a prototype francis turbine startup," *Renewable Energy*, vol. 157, pp. 1212–1221, 2020.

[60] S. Stadler, "Numerische lebensdauerberechnung einer francis turbine," Master's thesis, TU Wien - Institut für Energietechnik und Thermodynamik, 2020.

[61] K. Mühlbacher, "Auswertung und analyse von messdaten einer francisturbine," Master's thesis, TU Wien - Institut für Energietechnik und Thermodynamik, 2019.

Die approbierte gedruckte Originalversion dieser Diplomarbeit ist an der TU Wien Bibliothek verfügbar
The approved original version of this thesis is available in print at TU Wien Bibliothek.

[62] I. B. Celik, U. Ghia, P. J. Roache, C. J. Freitas, H. Coleman, and P. E. Raad, "Procedure for Estimation and Reporting of Uncertainty Due to Discretization in CFD Applications," *Journal of Fluids Engineering*, vol. 130, 07 2008. 078001.

[63] J. Jeong and F. Hussain, "Hussain, f.: On the identification of a vortex. jfm 285, 69-94," *Journal of Fluid Mechanics*, vol. 285, pp. 69 – 94, 02 1995.

[64] L. Eça and M. Hoekstra, "A procedure for the estimation of the numerical uncertainty of cfd calculations based on grid refinement studies," *Journal of Computational Physics*, vol. 262, pp. 104–130, 2014.

[65] P. J. Roache, "Quantification of uncertainty in computational fluid dynamics," *Annual Review of Fluid Mechanics*, vol. 29, no. 1, pp. 123–160, 1997.

Die approbierte gedruckte Originalversion dieser Diplomarbeit ist an der TU Wien Bibliothek verfügbar
The approved original version of this thesis is available in print at TU Wien Bibliothek.

List of Figures

Die approbierte gedruckte Originalversion dieser Diplomarbeit ist an der TU Wien Bibliothek verfügbar
The approved original version of this thesis is available in print at TU Wien Bibliothek.
TU Bibliothek Your knowledge hub WIEN

Die approbierte gedruckte Originalversion dieser Diplomarbeit ist an der TU Wien Bibliothek verfügbar
The approved original version of this thesis is available in print at TU Wien Bibliothek.

List of Tables

Die approbierte gedruckte Originalversion dieser Diplomarbeit ist an der TU Wien Bibliothek verfügbar
The approved original version of this thesis is available in print at TU Wien Bibliothek.

Appendix A

Matlab Code

A.1 GIS.m

```
%% Grid Independecy Study - VIW_16MW
clc;clear
addpath('plotdata','myfunctions')
preamble

% calculations for plotting
coarse = readmatrix('coarse.csv');
medium = readmatrix('medium.csv');
fine   = readmatrix('fine.csv');
Ustart = 40; Uend = 50;% maxU = 70
% 40 - 50
[phi,names] = GIS_plot(coarse,medium,fine,Ustart,Uend,screen);
iend = length(phi(:,1));

% datainput for GIS
SC = [3693240 1698788 1620846];
SV = [4080104 1231466 400574];
RN = [7284160 4641728 3143296];
DT = [3069164 1401375 986271];

% calculations for GIS
N = SC + SV + RN + DT;
h = (1./N).^(1/3);
r21 = h(2)/h(1); r32 = h(3)/h(2);
C = cell(15,iend);
```

Die approbierte gedruckte Originalversion dieser Diplomarbeit ist an der TU Wien Bibliothek verfügbar
The approved original version of this thesis is available in print at TU Wien Bibliothek.

```
26
27 for i = 1:iend
28     Phi    = phi(i,:);
29     eps21  = Phi(2)-Phi(1);
30     eps32  = Phi(3)-Phi(2);
31     s      = 1*sign(eps32/eps21);
32     R      = (Phi(1)-Phi(2))/(Phi(2)-Phi(3)); % Eca_Hoekstra
33     % convergence
34     if 0 < R && R < 1
35         disp(['Phi_',num2str(i),' --> monotonic convergence'])
36     elseif R > 1
37         disp(['Phi_',num2str(i),' --> monotonic divergence'])
38     elseif R < 0 && abs(R) < 1
39         disp(['Phi_',num2str(i),' --> oscillatory convergence'])
40     elseif R < 0 && abs(R) > 1
41         disp(['Phi_',num2str(i),' --> oscillatory divergence'])
42     end
43     % fixed-point iteration
44     pinit = (1/log(r21))*abs(log(abs(eps32/eps21)));
45     piter = @(p) order_of_method(p,r21,r32,s,eps32,eps21);
46     p      = fixed_point_iteration(piter,pinit);
47     % extrapolated values
48     Phiext21 = ((r21^p)*Phi(1) - Phi(2))/(r21^p - 1);
49     Phiext32 = ((r32^p)*Phi(2) - Phi(3))/(r32^p - 1);
50     % approximate relative error
51     ea21 = abs((Phi(1)-Phi(2))/Phi(1));
52     ea32 = abs((Phi(2)-Phi(3))/Phi(2));
53     % extrapolated relative error
54     eext21 = abs((Phiext21-Phi(1))/Phiext21);
55     eext32 = abs((Phiext32-Phi(2))/Phiext32);
56     % grid convergence index
57     GCI21 = ((1.25*ea21)/(r21^p - 1));
58     GCI32 = ((1.25*ea32)/(r32^p - 1));
59     % cellfilling
60     C{1,i} = N;
61     C{2,i} = r21;C{3,i} = r32;
62     C{4,i} = Phi(1);C{5,i} = Phi(2);C{6,i} = Phi(3);
63     C{7,i} = p;
64     C{8,i} = Phiext21;C{9,i} = Phiext32;
65     C{10,i} = ea21*100;C{11,i} = ea32*100;
66     C{12,i} = eext21*100;C{13,i} = eext32*100;
67     C{14,i} = GCI21*100;C{15,i} = GCI32*100;
68 end
```

Die approbierte gedruckte Originalversion dieser Diplomarbeit ist an der TU Wien Bibliothek verfügbar
The approved original version of this thesis is available in print at TU Wien Bibliothek.

```
69
70  fileID = fopen('GIS.txt');
71  c = textscan(fileID,'%s');
72  C = [c{1,1} C];disp(C);
73
74  hn   = NaN(1,4);hn(1) = 0;
75  Phin_21 = NaN(length(phi(:,1)),4);Phin_21(:,1) = 1;
76  Phin_32 = NaN(length(phi(:,1)),4);Phin_32(:,1) = 1;
77
78  for j = 1:length(Phin_21(:,1))
79      for i = 2:length(hn)
80          hn(i) = h(i-1)/h(1);
81          Phin_21(j,i) = phi(j,i-1)/C{8,j+1};
82          Phin_32(j,i) = phi(j,i-1)/C{9,j+1};
83      end
84  end
85
86  tit = ["$GIS_{21}:medium-fine$" "$GIS_{32}:coarse-medium$"];
87  for k = 1:2
88      f = figure(k+1);
89      if k == 1
90          f.Position = [screen(3)/2+21 screen(4)/2-15 (screen(3)/2)
                *0.5 screen(4)/2-85];
91          plot(hn,Phin_21(1,:),'r-^','MarkerFaceColor','r');hold on
92          plot(hn,Phin_21(2,:),'g-s','MarkerFaceColor','g')
93          plot(hn,Phin_21(3,:),'b-o','MarkerFaceColor','b')
94      else
95          f.Position = [screen(3)/2+21              50 (screen(3)/2)
                *0.5 screen(4)/2-150];
96          plot(hn,Phin_32(1,:),'r-^','MarkerFaceColor','r');hold on
97          plot(hn,Phin_32(2,:),'g-s','MarkerFaceColor','g')
98          plot(hn,Phin_32(3,:),'b-o','MarkerFaceColor','b')
99      end
100     xticks(linspace(0,1.5,7))
101     xlabel('Normalized cell size $h_n$ [-]')
102     ylabel('Normalized values $\Phi_n$ [-]')
103     legend(names,'Location','northwest')
104     title(tit(k))
105     grid on
106 end
```

Die approbierte gedruckte Originalversion dieser Diplomarbeit ist an der TU Wien Bibliothek verfügbar
The approved original version of this thesis is available in print at TU Wien Bibliothek.

A.2 dt_compare.m

```
% preamble & datainput
clc;clear;
addpath('plotdata','myfunctions')
preamble
A = readmatrix('16MW_M_output_dt.csv');
B = readmatrix('16MW_M_output_0.5dt.csv');
C = readmatrix('16MW_M_output_0.1dt.csv');

% calculations
n = 428.6;          % [U/min]
n = n/60;           % [U/s]
dtA = 3.8889e-04;   % [s]
dtB = 0.5*dtA;      % [s]
dtC = 0.1*dtA;      % [s]
A = [A(:,1) dtA*A(:,1) n*dtA*A(:,1) A(:,2:end)];% dt
B = [B(:,1) dtB*B(:,1) n*dtB*B(:,1) B(:,2:end)];% 0.5dt
C = [C(:,1) dtC*C(:,1) n*dtC*C(:,1) C(:,2:end)];% 0.1dt

% indices
U = 1;Uend = 70;
iA = find(A(:,3)>=U);iA = iA(1); iAend = find(A(:,3)<=Uend);iAend
    = iAend(end);
iB = find(B(:,3)>=U);iB = iB(1); iBend = find(B(:,3)<=Uend);iBend
    = iBend(end);
iC = find(C(:,3)>=U);iC = iC(1); iCend = find(C(:,3)<=Uend);iCend
    = iCend(end);

% for plotting
xA = A(iA:iAend,3);xAdummy = ones(length(xA),1);
xB = B(iB:iBend,3);xBdummy = ones(length(xB),1);
xC = C(iC:iCend,3);xCdummy = ones(length(xC),1);

interest = [4 5 6 7 8 9 10 11 12];% ETA HEAD pDTs_R pDTs_L pDyn1
    pDyn2 pD2 pR1 pS2
units = {'[\%]' '[m]' '(Pressure) [Pa]' '(Pressure) [Pa]' '(
    Absolute Pressure) [Pa]',...
        '(Absolute Pressure) [Pa]' '(pSTATCORR) [$\frac{kg}{ms
            ^{2}}$]',...
        '(pSTATCORR) [$\frac{kg}{ms^{2}}$]' '(pSTATCORR) [$\frac{
            kg}{ms^{2}}$]'};
```

Die approbierte gedruckte Originalversion dieser Diplomarbeit ist an der TU Wien Bibliothek verfügbar
The approved original version of this thesis is available in print at TU Wien Bibliothek.

```
names = {'Efficiency' 'Head' 'pDTs$_{R}$' 'pDTs$_{L}$' 'pDyn1' '
    pDyn2' 'pD2' 'pR1' 'pS2'};

% plotting
for i = 1:length(interest)
    j = interest(i);
    meanA = xAdummy*mean(A(iA:iAend,j));
    meanB = xBdummy*mean(B(iB:iBend,j));
    meanC = xCdummy*mean(C(iC:iCend,j));

    f = figure;
    f.Position = [50 screen(4)/2-50 screen(3)/2-50 (screen(4)
        /2-100)*0.6];
    plot(xA,A(iA:iAend,j),'Color',[0 0.4470 0.7410]);hold on
    plot(xA,meanA         ,'Color',[0 0.4470 0.7410],      '
        LineStyle','--')
    plot(xB,B(iB:iBend,j),'Color',[0.9290 0.6940 0.1250])
    plot(xB,meanB,         'Color',[0.9290 0.6940 0.1250],'
        LineStyle','--')
    plot(xC,C(iC:iCend,j),'Color',[0.6350 0.0780 0.1840])
    plot(xC,meanC,         'Color',[0.6350 0.0780 0.1840],'
        LineStyle','--')
    axis padded
        xticks([U 5:5:Uend])
    grid on
    xlabel('$T_{sim}$ [Runner Rev.]')
    ylabel(horzcat(names{i},' ',units{i}))
    legend('dt','mean','0.5dt','mean','0.1dt','mean','Location','
        southeast')
    title('dt-Comparison in Part Load Condition','FontSize',14)
    exportgraphics(gcf,['16MW_M_plot_', num2str(i),'.pdf'],'
        Resolution',300)
end
```

A.3 Subroutines

preamble.m

```
% preamble
set(0,'defaultTextInterpreter','latex')
```


Die approbierte gedruckte Originalversion dieser Diplomarbeit ist an der TU Wien Bibliothek verfügbar
The approved original version of this thesis is available in print at TU Wien Bibliothek.

```
set(0,'defaultLegendInterpreter','latex')
set(0,'defaultAxesFontSize',12)
set(0,'defaultTextFontSize',12)
% set(0,'defaultFigureWindowStyle','docked')
clear
close all
clc
clear vars
rng('default')
rng(0)
warning('off')
set(0,'units','pixels')
assignin('caller','screen',get(0,'ScreenSize'))
```

GIS_plot.m

```
function [phi,names] = GIS_plot(coarse,medium,fine,Ustart,Uend,
    screen)
n      = 428.57;      % [U/min]
n      = n/60;        % [U/s]
dt     = 3.8889e-04; % [s]
Q      = 18.02;       % [m3/s]
rho    = 998;         % [kg/m3]
g      = 9.81;        % [m/s2]
const = (g*rho*Q)/100;

A = fine; B = medium; C = coarse;
A = [A(:,1) dt*A(:,1) n*dt*A(:,1) A(:,2:end)];A = [A(:,:) A(:,4).*
    A(:,5)*const];
B = [B(:,1) dt*B(:,1) n*dt*B(:,1) B(:,2:end)];B = [B(:,:) B(:,4).*
    B(:,5)*const];
C = [C(:,1) dt*C(:,1) n*dt*C(:,1) C(:,2:end)];C = [C(:,:) C(:,4).*
    C(:,5)*const];

% indices
iA = find(A(:,3)>=Ustart);iA = iA(1); iAend = find(A(:,3)<=Uend);
    iAend = iAend(end);
iB = find(B(:,3)>=Ustart);iB = iB(1); iBend = find(B(:,3)<=Uend);
    iBend = iBend(end);
iC = find(C(:,3)>=Ustart);iC = iC(1); iCend = find(C(:,3)<=Uend);
    iCend = iCend(end);
```

Die approbierte gedruckte Originalversion dieser Diplomarbeit ist an der TU Wien Bibliothek verfügbar
The approved original version of this thesis is available in print at TU Wien Bibliothek.

```
19
20 % for plotting
21 xA = A(iA:iAend,3);xB = B(iB:iBend,3);xC = C(iC:iCend,3);
22
23 interest = [4 5 13];
24 names = {'$\eta$' '$H$' '$P_{out}$'};
25 units = {'[\%]' '[m]' '[W]'};
26
27 f = figure(1);
28 f.Position = [20 50 screen(3)/2 screen(4)-150];
29 t = tiledlayout(length(interest),1);t.TileSpacing = 'compact';t.
       Padding = 'compact';
30 phi = NaN(length(interest),3);
31
32 for i = 1:length(interest)
33     j = interest(i);
34     nexttile(i)
35     plot(xA,A(iA:iAend,j),'Color',[0 0.4470 0.7410],      '
          DisplayName','fine');hold on
36     plot(xB,B(iB:iBend,j),'Color',[0.9290 0.6940 0.1250],'
          DisplayName','medium')
37     plot(xC,C(iC:iCend,j),'Color',[0.6350 0.0780 0.1840],'
          DisplayName','coarse');hold off
38          xticks(Ustart:5:Uend)
39     grid on
40     xlabel('$T_{sim}$ [Runner Rev.]')
41     ylabel(horzcat(names{i},' ',units{i}))
42     legend
43     phi(i,:) = [mean(A(iA:iAend,j)) mean(B(iB:iBend,j)) mean(C(iC:
          iCend,j))];
44 end
45 return
46 end
```

order_of_method.m

```
1 function p = order_of_method(p,r21,r32,s,eps32,eps21)
2     q = log((r21^p - s)/(r32^p - s));
3     p = (1/log(r21))*abs(log(abs(eps32/eps21)) + q);
4 end
```

Die approbierte gedruckte Originalversion dieser Diplomarbeit ist an der TU Wien Bibliothek verfügbar
The approved original version of this thesis is available in print at TU Wien Bibliothek.